

# Capillary-Fed Zero-Gap Water Electrolyser

Colin van der Made



DELFT UNIVERSITY OF TECHNOLOGY

---

# Capillary-Fed Zero-Gap Water Electrolyser

---

Master Thesis

*Author:*

Colin van der Made, 5186900

To obtain the masters degree of Chemical Engineering

At TU Delft.

To be defended publicly on February 13, 2024 at 12:15 PM.

Thesis Committee:

F. M. Mulder

T. Burdyny

D. A. Vermaas

Keywords: zero-gap, capillary-fed, water electrolysis, alkaline medium, high performance, temperature difference, salt formation, gas chromatography, gas crossover.

Date: February 6, 2024



## Abstract

A transition towards renewable energy sources is necessary to globally achieve net-zero carbon emissions. To achieve reliable renewable energy production, storage of sustainable energy is key. The utilisation of hydrogen, whether for long-term or short-term storage, could provide a vital solution in achieving reliability for sustainable energy demand. However, producing green hydrogen (water electrolysis) is not cost-competitive with fossil fuels and other hydrogen production methods. An original alkaline electrolyser design has been created that can help with lowering the CAPEX and OPEX when optimized. In common alkaline electrolysers, electrodes are completely immersed in liquid. However, the electrode surfaces of the novel design apply wetted surfaces through the use of capillary forces to suck up electrolytes. Compared to immersed electrode surfaces, the wetted surface shows a reduction in (bubble) resistance leading to lower voltage losses. Additionally, the overpotential can be further reduced with, for example, the use of a PES membrane instead of a common Zirfon membrane, better contact with the anode by welding it to the current collector, and adding PTFE to the anode for better gas removal. Prior to testing the assembled cell design, the electrodes were tested individually to understand the mechanics of each electrode. Here, we report that the electrodes perform well individually in alkaline media. However, our findings reveal that the assembled cell performs poorly, mostly because of significant overpotentials brought on by increasing resistance, along with other drawbacks including salt formation and exceeding the legal gas crossover limit. Some of these issues regarding performance are still poorly understood and therefore need further investigation.

# Part I

## Table of Contents

---

|   |           |
|---|-----------|
| <b>Abbreviations</b>                          | <b>7</b>  |
| <b>1 Introduction</b>                         | <b>8</b>  |
| 1.1 Alkaline electrolysis cells . . . . .     | 8         |
| 1.2 Electrolyte transport behaviour . . . . . | 9         |
| 1.3 Gas crossover . . . . .                   | 10        |
| 1.4 Project Aim . . . . .                     | 11        |
| <b>2 Experimental</b>                         | <b>12</b> |
| 2.1 Materials for cell assembly . . . . .     | 12        |
| 2.2 Chemicals . . . . .                       | 14        |
| 2.3 Anode preparation . . . . .               | 14        |
| 2.4 Cathode preparation . . . . .             | 14        |
| 2.5 Analytical methods . . . . .              | 15        |
| <b>3 Results and discussions</b>              | <b>18</b> |
| 3.1 SEM . . . . .                             | 18        |
| 3.2 EDX . . . . .                             | 20        |
| 3.3 Cathode cyclic performance . . . . .      | 21        |
| 3.4 Anode cyclic performance . . . . .        | 22        |
| 3.5 Alkaline cell performance . . . . .       | 24        |
| 3.6 Zero-gap cell performance . . . . .       | 24        |
| 3.7 Gas crossover . . . . .                   | 31        |
| <b>4 Conclusion</b>                           | <b>32</b> |
| <b>5 Outlook</b>                              | <b>33</b> |
| <b>6 Acknowledgement</b>                      | <b>34</b> |
| <b>Appendix</b>                               | <b>38</b> |

---

## List of Figures

|    |   |    |
|----|---|----|
| 1  | (a) Schematic of a conventional alkaline electrolysis cell with both electrodes fully immersed in liquid electrolyte. (b) Schematic of a zero-gap alkaline electrolysis cell with both electrodes fully immersed in liquid electrolyte. (c) Schematic of an asymmetrical PEM cell with one electrode immersed in liquid electrolyte. (d) Schematic of a zero-gap capillary-fed alkaline cell, where no electrodes are immersed in liquid electrolyte. Electrolyte is continuously supplied due to a capillary effect, together with the addition of an electrolyte reservoir. . . . .   | 9  |
| 2  | (a) Schematic of the flow of the electrolyte (ions and water molecules). The flow is upwards due to the capillary forces. (b) Schematic of ionic accumulation, causing salt formation on the cathode and possibly increasing resistance overall. . . . .  | 10 |
| 3  | (a) Schematic of crossover in a typical alkaline electrolyser. The thickness of the membrane is approximately 2–3 mm (or 500 $\mu\text{m}$ for a Zirfon membrane). The produced gas on one side has to diffuse through three phases before poisoning the other side by lowering its purity. (b) schematic of crossover in the zero-gap capillary-fed alkaline electrolyser. The thickness of the membrane is approximately 140 $\mu\text{m}$ . The produced gas on one side now diffuses much faster compared to the alkaline electrolyser schematic, as it does not necessarily move through three phases since the produced gas is in immediate contact with the membrane. . . . .  | 11 |
| 4  | (a) Side view of the cell design. 1) Bipolar plate position bolt 2) Tie bolts 3) Cell frame 4) Perforated bipolar plate (made from stainless steel) 5) Cathode 6) PES separator 7) Gasket 8) Welded anode to a perforated bipolar plate. (b) Rear view of the cell design. 9) Reference electrode insertion 10) Gas outlet 11) Connection to reservoir 12) Gas chamber 13) Liquid reservoir chamber. (c) Rear view of assembled cell. . . . .   | 12 |
| 5  | Image of the 3D printer used for printing the cell design. . . . .  | 13 |
| 6  | Schematic of the cricut design of the gasket. . . . .   | 13 |
| 7  | Electrotaped anode before electroplating. This is done to ensure metal-metal contact for welding is possible with the bipolar plate and the anode. The area for electroplating is 1x1 cm. . . . .   | 14 |
| 8  | Schematic of the spray pattern done for the HER electrode. The purple arrow represents a spacing of 6 mm. The yellow arrow represents a spacing of 2 mm. . . . .  | 15 |
| 9  | Schematic of the GC setup where the anode outlet is attached to the GC and nitrogen is used as a carrier gas. The cathode outlet is attached to a volume of water for backpressure. . . . .   | 16 |
| 10 | Schematic of the setup to calculate the faradaic efficiency. The gasses push down the liquid level inside the beaker. The gasses are produced until the known volume is filled with gas, where the time this takes is measured. . . . .   | 17 |
| 11 | (a) Side view of the cathode showing thickness of the sprayed coating (150 $\mu\text{m}$ ). (b) Image of the sprayed surface. Sample has a loading of 0.48 mg/cm <sup>2</sup> Pt. . . . .   | 18 |
| 12 | (a) Thickness of the coating (1.2 $\mu\text{m}$ ). (b) Image of the electrocoated surface. Sample is prepared via pulse applied potential for 300 pulses, using 50/50 Ni(NO <sub>3</sub> ) <sub>2</sub> ·6 H <sub>2</sub> O (0.15 M), FeSO <sub>4</sub> (0.15 M). . . . .   | 19 |
| 13 | (a) Thickness of the coating (1.2 $\mu\text{m}$ ). (b) Image of the electrocoated surface. Sample is prepared via pulse applied potential for 300 pulses, using 80/20 Ni(NO <sub>3</sub> ) <sub>2</sub> ·6 H <sub>2</sub> O (0.24 M), FeSO <sub>4</sub> (0.06 M). . . . .   | 19 |
| 14 | (a) Bare Sigracet 22BB, cycling between -1.2 V - -0.5 V (vs Hg/HgO), scanrate = 10 mV/s, cycles 1, 5, 9, 13 and 17 are shown. (b) Spray coated Sigracet 22BB with 0.3 mg/cm <sup>2</sup> loading, cycling between -1.2 V - -0.5 V (vs Hg/HgO), scanrate = 10 mV/s, cycles 1, 5, 9, 13, 17, 21, 25, 29, 33 and 37 are shown. (c) Platinum wire, cycling between -1.2 V - -0.8 V (vs Hg/HgO), scanrate = 10 mV/s, cycles 1 up to 20 are shown. . . . .  | 22 |
| 15 | (a) 70/30 Ni/Fe ratio (dried for one day after plating), cycling between 0.25 V - 0.55 V (vs Hg/HgO), scanrate = 10 mV/s, cycles 1, 5, 9, 13, 17, 21, 25, 29, 33 and 37 are shown. (b) 70/30 Ni/Fe ratio (submerged in KOH for 1 hour before cycling), cycling between 0.25 V - 0.55 V (vs Hg/HgO), scanrate = 10 mV/s, cycles 1, 5, 9, 13, 17, 21, 25, 29, 33 and 37 are shown. (c) 50/50 Ni/Fe ratio (dried for one day after plating), cycling between 0.25 V - 0.55 V (vs Hg/HgO), scanrate = 10 mV/s, cycles 1, 5, 9, 13, 17, 21, 25, 29, 33 and 37 are shown. (d) 80/20 Ni/Fe ratio (dried for 24 hours after plating), cycling between 0.25 V - 0.55 V (vs Hg/HgO), scanrate = 10 mV/s, cycles 1, 5, 9, 13, 17, 21, 25, 29, 33 and 37 are shown. (e) 80/20 Ni/Fe ratio with 10 g/L PTFE (dried for 24 hours after plating), cycling between 0.25 V - 0.55 V (vs Hg/HgO), scanrate = 10 mV/s, cycles 1, 5, 9, 13, 17, 21, 25, 29, 33 and 37 are shown. (f) 20th cycle of all previously mentioned experiments (70/30, 70/30-KOH, 50/50, 80/20, 80/20-PTFE). . . . . | 23 |
| 16 | Pourbaix diagram of Nickel (Ni), reproduced from Singh et al. [45]. . . . .   | 23 |

|     |   |    |
|-----|---|----|
| 17  | (a) Full range cycling between 0.0 V - 1.6 V. RE is attached with the CE. Scan rate = 10 mV/s. Illustrating the first and second cycle. WE = anode, CE = cathode. (b) Cycling between 1.0 V - 1.6 V. RE is attached with the CE. Scan rate = 10 mV/s. Illustrating the first and second cycle. WE = anode, CE = cathode. . . . .  | 24 |
| 18  | (a) Cell performance for constant current (200 mA/cm <sup>2</sup> ) depicts poor stability; the current supply can only be upheld going up to 9 V, where up to 40 minutes the fluctuations are kept at a minimum. (b) Cell performance for constant current (200 mA/cm <sup>2</sup> ) depicts poor stability; the current supply can only be upheld going up to 7.5 V, where up to 40 minutes the fluctuations are kept at a minimum. (c) Cell performance for constant current (100 mA/cm <sup>2</sup> ) depicts poor stability; the current supply can only be upheld going up to 6.5 V, where up to 120 minutes the fluctuations are kept at a minimum. . . . .                      | 25 |
| 19  | Experimental data showing a change in potential with different temperatures and different currents (plotted on a logarithmic scale). . . . .  | 25 |
| 20  | Graph of water splitting regime at different temperatures, reproduced from Mori et al. [47]. . . .  | 26 |
| 21  | (a) Cell performance for 15 h at 30 °C at 50 mA/cm <sup>2</sup> . (b) Cell performance for 15 h at 40 °C at 50 mA/cm <sup>2</sup> and 15 h at 75 mA/cm <sup>2</sup> . (c) Cell performance for 15 h in total, at 60 °C at 50 mA/cm <sup>2</sup> , 75 mA/cm <sup>2</sup> and 100 mA/cm <sup>2</sup> (5 hours each). (d) Cell performance for 15 h in total, at 80 °C at 50 mA/cm <sup>2</sup> , 75 mA/cm <sup>2</sup> and 100 mA/cm <sup>2</sup> (5 hours each). . . . .   | 27 |
| 22  | Experimental data showing the cathode and anode performance with the Hg/HgO referenced at the anode. Showing the first and second cycles, scanrate = 2 mV/s. The instability of the stainless steel current collector is expressed in oxidation and reduction reactions aside from the regular nickel reactions. . . . .  | 28 |
| 23  | Pourbaix diagram for iron at ionic concentrations of 1.0 mM. Extracted from [51]. . . . .   | 29 |
| 24  | (a) FE of 5 different current densities. Only the O <sub>2</sub> side is measured, and no backpressure was applied on the H <sub>2</sub> side. The carrier gas flow was set to 8 mL/min. (b) FE measurement at a constant current of 100 mA/cm <sup>2</sup> . The gas was carried by 7 mL/min of N <sub>2</sub> . (c) FE measurement at a constant current of 200 mA/cm <sup>2</sup> , carried with 10 mL/min of N <sub>2</sub> . . . . .   | 30 |
| 25  | (a) Salt formation occurring after a 5-hour (constant current of 100 mA/cm <sup>2</sup> ) measurement at room temperature at the backside of the cathode. (b) Salt formation occurring after a 15-hour (constant current of 50 mA/cm <sup>2</sup> ) measurement at room temperature at the backside of the cathode. (c) Salt formation occurring after a 15-hour (constant current of 50 mA/cm <sup>2</sup> - 100 mA/cm <sup>2</sup> ) measurement at 80 °C at the backside of the cathode. . . . .   | 30 |
| 26  | (a) H <sub>2</sub> gas crossover in O <sub>2</sub> at a constant current of 200 mA/cm <sup>2</sup> . A trend has been added to this graph since the exact backpressure is difficult to get the same as the applied pressure from the nitrogen gas. (b) Varying current densities with constant carrier gas flow (8 mL/min). A trendline is added to discuss the similarities to that found in literature [6]. . . . .   | 31 |
| B.1 | 80/20 coating Ni(NO) <sub>3</sub> ·6H <sub>2</sub> O (0.24 M) and Fe(SO <sub>4</sub> )·7H <sub>2</sub> O (0.06 M) together with PTFE (10 g/L) on a stainless steel mesh, cycling between 0.25 V-0.55 V (vs Hg/HgO), scanrate = 10 mV/s, cycles 1, 5, 9, 13, 17, 21, 25, 29, 33 and 37 are shown. . . . .  | 41 |
| C.1 | Graph of the XRD measurement showing the peaks for nickel, overshadowing any presence of other substances. . . . .  | 42 |
| D.1 | (a) Image showing the surface structure of the Ni-coating (no Fe). The method used for applying this coating is constant current as discussed in Appendix B. (b) Image showing the thickness of the coating; the same sample is used as in the previous subfigure. Coating has a thickness of approximately 10–15 microns. (c) overhead view illustrating that the coating is covering the whole surface due to handling or bending the material. (d) Sideview image of a sample using the pulse applied potential method, showing thickness of approximately 1 micron. . . . .   | 43 |
| D.2 | (a) Image showing the backside of a piece of coating. (b) 3000x zoomed-in image of the surface of the coating, showing boundaries and some detail about the surface roughness. (c) 10000x zoomed-in image of the surface of the coating showing boundaries and the surface roughness in greater detail. (d) 30000x zoomed-in image of the surface of the coating, showing great detail about the surface roughness and structure. (e) Image taken of a place where the substrate is bended so the coating can be peeled off. (f) A more zoomed-in image of the same area as previous subfigure, showing the thickness of the coating is relatively equal and close to 1 micron. . . . . | 44 |
| D.3 | (a) Three-phase image of the PTFE, one after the other, more zoomed-in. (b) A different chosen area where blob-like structures are seen. . . . .  | 45 |

|     |  |    |
|-----|--|----|
| E.1 | (a) Coupled with (d): Completely dry membrane, not used for cell testing. (b) Coupled with (e): Membrane wetted with dionised water, not used for cell testing. (c) Coupled with (f): Membrane sample put in KOH and dried in vacuum, not used for cell testing. Salt crystals formed on the surface of the membrane. . . . .  | 46 |
| E.2 | (a) Coupled with (b): The side of the membrane touching the anode during testing, using a current of 100 mA. (c) Coupled with (d): The side of the membrane touching the cathode during testing, using a current of 100 mA. . . . .  | 47 |
| E.3 | (a) Coupled with (b): The side of the membrane touching the anode during testing, using a current of 300 mA. (c) Coupled with (d): The side of the membrane touching the cathode during testing, using a current of 300 mA. . . . .  | 48 |
| E.4 | (a) Coupled with (b): The side of the membrane touching the anode during testing, using a current of 300 mA, cleaned with deionised water. (c) Coupled with (d): The side of the membrane touching the cathode during testing, using a current of 300 mA, cleaned with dionised water. . . . .   | 49 |
| F.1 | (a) Coupled with (b): Ni(OH) <sub>2</sub> coating on the nickel mesh. The coating shows a green color. (c) Coupled with (d): NiFe(OH) <sub>2</sub> coating on the nickel mesh. The coating shows a golden color. . . . .   | 50 |
| F.2 | (a) Image of the coated material before welding. The left side is the electrode after removing the electrocoated tape. The rightside is the electrode before removing the tape and the extended part that connects with the parstat. (b) same electrodes, together with a ruler to show that the electrocoated part is 1 cm. (c) Indicates that the other side of the electrode is also 1 cm. . . . .  | 51 |
| G.1 | (a)-(b) Images of the areas where the EDX measurements are done. The surface is scraped to ensure the coating is not in contact with the substrate. Sample is prepared via pulse applied potential for 300 pulses, using 50/50 Ni(NO <sub>3</sub> ) <sub>2</sub> ·6 H <sub>2</sub> O (0.15 M), FeSO <sub>4</sub> ·7 H <sub>2</sub> O (0.15 M). (c) An example of the peaks of the different elements measured on one of the areas measured. . . . .  | 52 |
| G.2 | (a)-(c) Images of the areas where the EDX measurements are done. The surface is scraped to ensure the coating is not in contact with the substrate. The sample is prepared via pulse applied potential for 300 pulses using 80/20 Ni(NO <sub>3</sub> ) <sub>2</sub> ·6 H <sub>2</sub> O (0.24 M) and FeSO <sub>4</sub> ·7 H <sub>2</sub> O (0.06 M). . . . .   | 52 |
| G.3 | (a)-(c) Images of the areas where the EDX measurements are done. The surface is scraped to ensure the coating is not in contact with the substrate. The sample is prepared via pulse applied potential for 300 pulses using 80/20 Ni(NO <sub>3</sub> ) <sub>2</sub> ·6 H <sub>2</sub> O (0.24 M), FeSO <sub>4</sub> ·7 H <sub>2</sub> O (0.06 M) and PTFE (10g/L). . . . .   | 53 |
| G.4 | (a)-(c) Images of the areas where the EDX measurements are done. The sample used was used for the cell setup for a certain amount of time, and after cleaning, it was used for SEM imaging. The sample is prepared via pulse applied potential for 300 pulses using 80/20 Ni(NO <sub>3</sub> ) <sub>2</sub> ·6 H <sub>2</sub> O (0.24 M) and FeSO <sub>4</sub> ·7 H <sub>2</sub> O (0.06 M). . . . .   | 53 |
| H.1 | (a) FE of 5 different current densities. Only the O <sub>2</sub> side is measured, and no backpressure was applied on the H <sub>2</sub> side. The carrier gas flow was set to 8 mL/min. (b) Graph of the FE values acquired from the GC. The graph is split into three segments, where the first segment considers an overpressure on the oxygen side, the second considers an overpressure on the hydrogen side, and the last segment considers equal pressure. The measurement was performed at a constant current density of 200 mA/cm <sup>2</sup> . . . . .  | 55 |
| I.1 | (a) Backside of the anode after measuring at 80 °C for 15 hours. (b) Cathode gas chamber after measuring at 80 °C for 15 hours. (c) Cathode side of the membrane after measuring at 80 °C for 15 hours. . . . .  | 56 |
| J.1 | Gas crossover measurement all injections. The color spectra indicate the injection number at that specific current density. . . . .  | 57 |
| J.2 | (a) H <sub>2</sub> gas crossover in O <sub>2</sub> at a constant current of 200 mA/cm <sup>2</sup> . Four separate measurements are done to see what the gas crossover does. (b) OH <sub>2</sub> gas crossover in H <sub>2</sub> at a constant current of 200 mA/cm <sup>2</sup> . Four separate measurements are done to see what the gas crossover does. Note: (1) The GC setups used for this experiment uses calibration gasses to get PPM values from the area of the peak, for oxygen however, there is only one calibration gas while typically a minimum of two is required for accurate results. (2) The use of hydrogen gas in the GC setup used for O <sub>2</sub> crossover uses a different calibration gas than the GC setup used for H <sub>2</sub> crossover. The difference between the two setups is the standard value it will output whenever it detects almost no gas, this has been accounted for in these graphs. . . . . | 58 |

## List of Tables

|   |   |    |
|---|---|----|
| 1 | EDX table of the 50/50 $\text{Ni}(\text{NO}_3)_2 \cdot 6\text{H}_2\text{O}$ (0.15 M) and $\text{FeSO}_4 \cdot 7\text{H}_2\text{O}$ (0.15 M) sample. A total of 6 measurements are done to establish the average. . . . .  | 20 |
| 2 | EDX table of the 80/20 $\text{Ni}(\text{NO}_3)_2 \cdot 6\text{H}_2\text{O}$ (0.24 M) and $\text{FeSO}_4 \cdot 7\text{H}_2\text{O}$ (0.06 M) sample. A total of 7 measurements are done to establish the average. . . . .  | 20 |
| 3 | EDX table of the 80/20 $\text{Ni}(\text{NO}_3)_2 \cdot 6\text{H}_2\text{O}$ (0.24 M) and $\text{FeSO}_4 \cdot 7\text{H}_2\text{O}$ (0.06 M) sample together with the addition of PTFE. A total of 9 measurements are done to establish the average. . . . .             | 21 |
| 4 | EDX table of the 80/20 $\text{Ni}(\text{NO}_3)_2 \cdot 6\text{H}_2\text{O}$ (0.24 M) and $\text{FeSO}_4 \cdot 7\text{H}_2\text{O}$ (0.06 M) after using the electrode in the zero-gap cell design. A total of 7 measurements are done to establish the average. . . . . | 21 |

## Abbreviations and Acronyms

|              |   |
|--------------|---|
| <b>AEM</b>   | Anion Exchange Membrane                       |
| <b>BED-C</b> | Backscattered Electron Detector               |
| <b>CAPEX</b> | Capital expenditure                           |
| <b>CE</b>    | Counter electrode                             |
| <b>EDX</b>   | Energy-dispersive X-ray                       |
| <b>FE</b>    | Faradaic Efficiency                           |
| <b>GC</b>    | Gas Chromatography                            |
| <b>HHV</b>   | Higher heating value                          |
| <b>IRENA</b> | International Renewable Energy Agency         |
| <b>ISO</b>   | International Organization of Standardization |
| <b>LCOH</b>  | Levelised costs of hydrogen                   |
| <b>LEL</b>   | Lower Explosion Limit                         |
| <b>OPEX</b>  | Operational expenditure                       |
| <b>PEM</b>   | Proton exchange membrane                      |
| <b>PES</b>   | Polyether sulfone                             |
| <b>RE</b>    | Reference electrode                           |
| <b>SED</b>   | Secondary Electron Detector                   |
| <b>SEM</b>   | Scanning electron microscope                  |
| <b>UEL</b>   | Upper Explosion Limit                         |
| <b>WE</b>    | Working electrode                             |
| <b>XRD</b>   | X-ray powder diffraction                      |

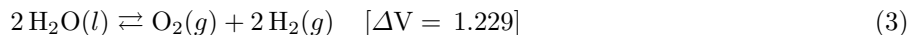
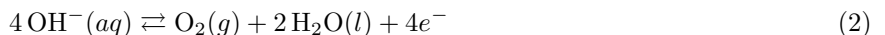
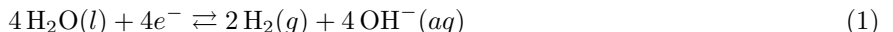
# 1 Introduction

Before 2050, civilization must attain net-zero carbon emissions globally [1]. Specifically, hard-to-abate sectors will have to go through the transition of decarbonisation, in which renewable hydrogen will play a vital role [2–6]. Renewable hydrogen is best produced by energy sources such as solar and wind energy whenever energy production is in surplus relative to demand, but other renewable power sources such as biomass, geothermal energy, or hydropower can be utilised as base-load [7–9]. A major challenge to utilising solar and wind energy as the main renewable energy sources is the production fluctuations. Since excess energy can be chemically stored in hydrogen, the fluctuations of renewable electricity can be covered and stabilised when demand is higher than production. Larger quantities of hydrogen can be stored in, for example, storage tanks [10], salt caverns [11], or smaller quantities of metal hydrides [12] and extracted when demand is higher than production. For hydrogen production via water electrolysis, two main techniques are readily used for large-scale applications [13]:

- Alkaline water electrolysis
- Proton exchange membrane electrolysis (or polymer electrolyte membrane) (PEM)

Both electrochemical techniques require energy to split water molecules into hydrogen gas, formed at the cathode, and oxygen gas, formed at the anode. Presently, the levelised cost of green hydrogen (LCOH) is not competitive with fossil fuels due to high capital expenditure (CAPEX) and high operational expenditure (OPEX) [14]. State-of-the-art commercial water electrolyzers typically require 53 kWh/kg of produced hydrogen, while only 39.4 kWh/kg of the energy is able to be extracted, according to the higher heating value (HHV) of H<sub>2</sub> [15]. To put this into perspective, 1 kg of coal, the most commonly used fossil fuel for electricity generation, typically produces 6.7–8.1 kWh/kg, excluding the very low thermal efficiency of about 37% for electrical generators (coming down to requiring ~20 times more kg of coal than H<sub>2</sub> for the same amount of energy) [16–19]. The International Renewable Energy Agency (IRENA) has set a target to decrease cell energy consumption to <42 kWh/kg by 2050 [14]. By increasing the efficiency of the reactions, heat exchange, and other factors, the energy consumption can be further reduced to reach the goal set by IRENA before 2050. Previous studies found improved methods getting closer to the desired target by utilising Anion Exchange Membrane (AEM), which is the cheaper option compared to Proton Exchange Membrane (PEM), since it uses non-noble metals [20–22]. In this research, the focus is on alkaline water electrolysis, as a recent study has come out that claims to reach close to 100% faradaic efficiency with low gas crossover and 100% cell energy efficiency at 85 °C and 0.3 A cm<sup>-2</sup> (based on the HHV), surpassing the target set by IRENA [6].

Building upon the aforementioned results, it is essential to analyse their findings by delving into the theory of hydrogen production in an alkaline medium. The half reactions and total reaction in alkaline medium are formulated in (Eq. 1-3)[13, 23]. For more in-depth half reactions, please refer to Appendix A.



Water electrolysis requires a minimum potential difference of 1.229 V at standard conditions, although, to maintain a constant temperature at this potential difference, external heat is required. Whenever no external heat is supplied, the thermo-neutral potential difference of water splitting at room temperature is 1.482 V [24].

## 1.1 Alkaline electrolysis cells

The main goal of this project is to successfully produce green hydrogen that is cost-competitive with fossil fuels. However, efficiency of the electrolyzers tend to be a large problem. Conventional alkaline electrolyzers have both electrodes immersed in a liquid electrolyte (Figure 1a). A variation on this setup is the zero-gap alkaline electrolysis cell (Figure 1b). Both electrodes are still immersed in a liquid electrolyte but exhibit lower electrolyte resistance due to the reduced distance between the electrodes. In contrast, an asymmetrical PEM electrolysis cell is a type of cell where only one electrode is immersed in a liquid electrolyte (Figure 1c). This brings an additional reduction in overpotential due to the mitigation of bubble formation on one side of the cell. Additionally, another cell design has been created by integrating the features from 1b and 1c (refer to Figure 1d): instead of immersed electrodes, only the surface of the electrodes is now wetted with liquid electrolyte. The reduced distance reduces electrolyte resistance and since the surface is only wetted, this mitigates bubble resistance. A spontaneous effect, known as the capillary effect, continuously supplies the electrodes with electrolyte with the help of a separator. The separator is partly immersed in an external

reservoir of liquid electrolyte, thereby able to maintain the capillary effect, consequently, keeping the electrode surfaces wet.

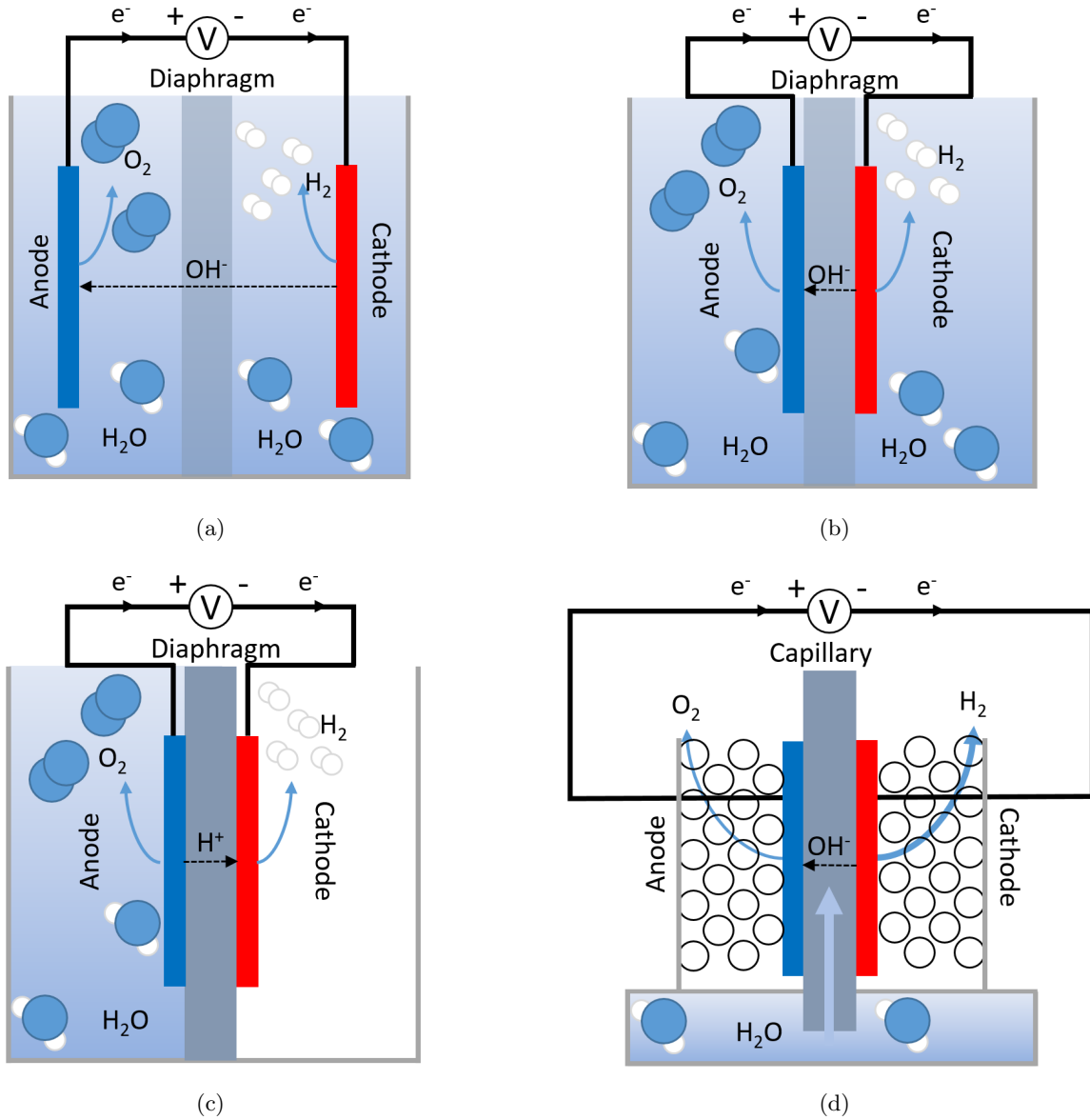


Figure 1: (a) Schematic of a conventional alkaline electrolysis cell with both electrodes fully immersed in liquid electrolyte. (b) Schematic of a zero-gap alkaline electrolysis cell with both electrodes fully immersed in liquid electrolyte. (c) Schematic of an asymmetrical PEM cell with one electrode immersed in liquid electrolyte. (d) Schematic of a zero-gap capillary-fed alkaline cell, where no electrodes are immersed in liquid electrolyte. Electrolyte is continuously supplied due to a capillary effect, together with the addition of an electrolyte reservoir.

## 1.2 Electrolyte transport behaviour

A capillary-fed electrolyser is a novel concept, thus the physics of the capillary effect is essential to understand. A porous medium (a PES separator in the case of this study) comprises numerous pores (in literature referred to as voids) and a skeleton of the material (referred to as the matrix) [25]. Capillary action represents the ability of a liquid to flow in narrow spaces without the assistance of external forces, working against forces like gravity [26]. The capillary rise can be seen as the adhesive forces (generally referred to as capillary forces) between the walls of the capillary tube and the liquid, causing the liquid to move upwards. The surface tension (a cohesive force) consistently pulls molecules from the surface inward [27]. The adhesive and cohesive forces counteract each other, and the liquid stops rising until the net force is balanced. The rate and capability at which the liquid level rises depend on the pore size, the viscosity of the liquid, and the surface tension of the

liquid [6, 28]. A schematic of the flow of the electrolyte within the cell is portrayed in Figure 2a. Additionally, the flow of the electrolyte contains water and ions.  $\text{H}_2\text{O}$  is consumed and  $\text{OH}^-$  is produced at the cathode. Since  $\text{OH}^-$  is consumed at the anode, the ionic flow of the  $\text{OH}^-$  directs towards the anode. The ionic flow is caused by a chemical gradient (concentration difference) and an electrical gradient (migration of the electrical current flowing). Since  $\text{H}_2\text{O}$  is consumed, electrolyte is constantly replenished due to upward capillary forces. Other than the concentration gradient, there is no force or phenomenon playing a role in the mitigation of ion buildup by the downward flow of ions. This could potentially result in an increase in resistance (conversely, a decrease in conductivity) whenever the concentration becomes too large [29].

Moreover, the cathode exhibits a porous morphology, allowing the produced  $\text{OH}^-$  (and to account for neutral charge,  $\text{K}^+$  flow) to permeate through the backside of the electrode, leading to salt precipitation or 'salting out' when in contact with  $\text{CO}_2$  forming bicarbonates [30]. Additionally, when ion concentration surpasses the solubility limit of salt in water, salt formation (KOH) is imminent. Figure 2b shows a simplified schematic to represent what this ion accumulation would look like.

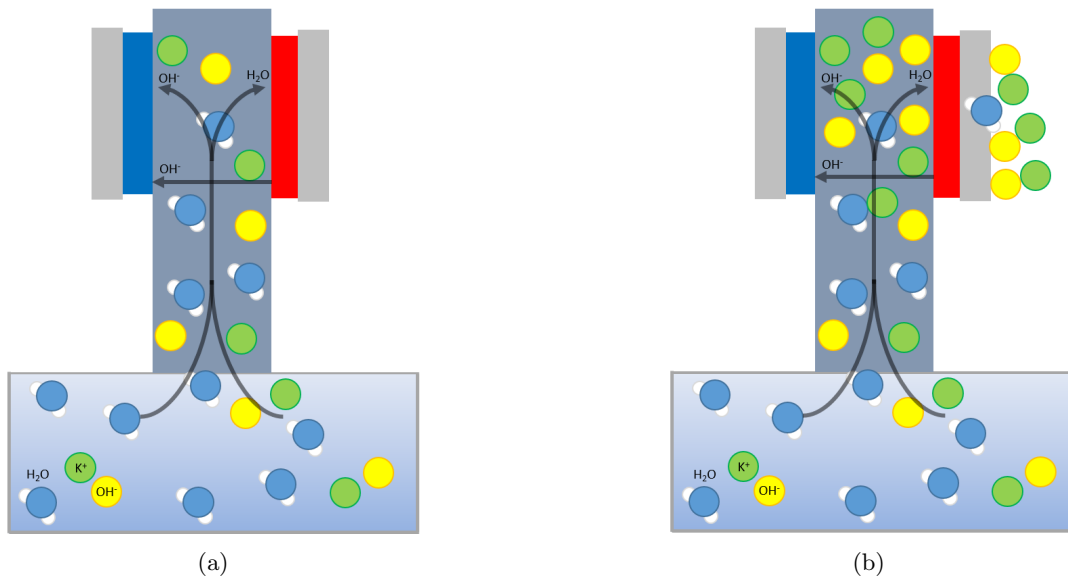


Figure 2: (a) Schematic of the flow of the electrolyte (ions and water molecules). The flow is upwards due to the capillary forces. (b) Schematic of ionic accumulation, causing salt formation on the cathode and possibly increasing resistance overall.

### 1.3 Gas crossover

Two main barriers typically prevent gas crossover in alkaline water electrolyzers. The first barrier is gas dissolution in the liquid electrolyte. The second barrier is the diffusion of the gas molecules through the separator. Both barriers in the capillary-fed zero-gap cell are reduced, leading to an increased risk of gas crossover, which in turn, lead to increased safety issues. The lower explosion limits (LEL) and upper explosion limits (UEL) of  $\text{H}_2/\text{O}_2$  mixtures are 3.8 mol% and 95.4 mol%  $\text{H}_2$  at atmospheric pressure and 80 °C respectively [31, 32]. In order to mitigate ignition and explosion risks, the maximum allowed mol% of hydrogen in oxygen is determined to be below 2 mol% by the ISO (International Organization of Standardization) [33].

In this novel design, the first barrier is removed from the system due to the absence of liquid media, which previously hindered the transport by requiring gas dissolution. Instead of hydrogen/oxygen content in the range of  $10^{-3}$  mol/L in a liquid medium, gas contains a considerably higher concentration of  $\text{H}_2/\text{O}_2$ , as 1 L of gas volume contains approximately 0.04 moles of gas (assuming an ideal gas at standard conditions) in a gas medium. Additional risks are posed by the high diffusion rate of the molecules in the gas phase, as they have a diffusion rate which is 5 orders of magnitude larger in the gas phase in comparison to the aqueous phase ( $10^{-4}\text{m}^2/\text{s}$  vs  $10^{-9}\text{m}^2/\text{s}$ , respectively) [34, 35].

Furthermore, the second barrier is also reduced by the thickness of the separator. In the capillary-fed zero-gap cell, the separator is 140 microns thick. Typical zero-gap cells use membranes with similar thickness ( $\sim 100 \mu\text{m}$ ), while porous separators of regularly used alkaline electrolyzers are stated to be 2-3 mm thick [36]. A more

commonly utilised separator in an alkaline electrolyser is, however, a Zirfon membrane. These membranes are usually in the range of  $500\ \mu\text{m}$  thick [37]. It is believed that, because of the reduction or elimination of these barriers, the purity of the gas will not be maintained above the critical point established by ISO in order to reduce any risk of explosion. Please refer to Figures 3a and 3b for a schematic of the gas crossover for both types of electrolysers.

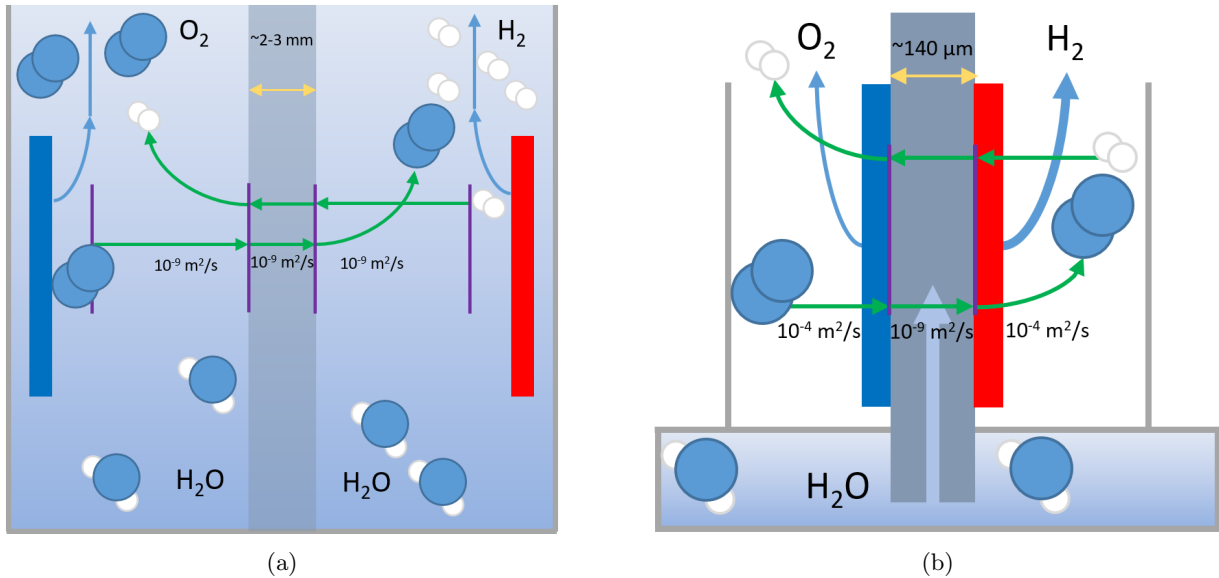


Figure 3: (a) Schematic of crossover in a typical alkaline electrolyser. The thickness of the membrane is approximately 2–3 mm (or  $500\ \mu\text{m}$  for a Zirfon membrane). The produced gas on one side has to diffuse through three phases before poisoning the other side by lowering its purity. (b) schematic of crossover in the zero-gap capillary-fed alkaline electrolyser. The thickness of the membrane is approximately  $140\ \mu\text{m}$ . The produced gas on one side now diffuses much faster compared to the alkaline electrolyser schematic, as it does not necessarily move through three phases since the produced gas is in immediate contact with the membrane.

## 1.4 Project Aim

In order to move away from conventional alkaline water electrolysis, a capillary-fed cell design has been created. As mentioned previously, recent research stated that high efficiencies and low gas crossover were acquired at high current densities [6]. The goal of this study is trying to reproduce the capillary-fed electrolyser setup components and catalysts and testing whether the same high performances can be acquired. To reach this goal, first the operation of the individual electrodes is experimentally determined. Secondly, the components are assembled and tested under controlled conditions. The final step is for relevant parameters to be investigated to finalise the concluding evidence of the validity of the acquired results attained by Hodges et al. [6]. Relevant factors to be taken into account in this research are:

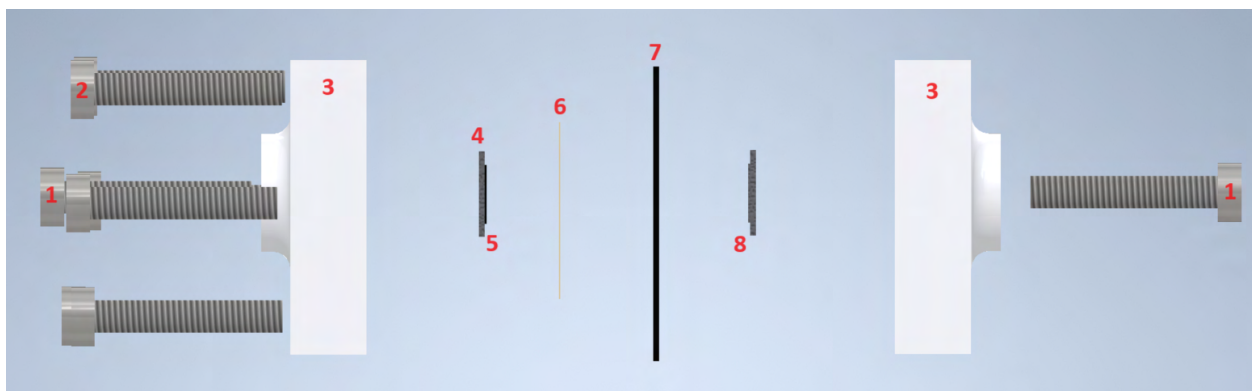
- Electrolyte and KOH transport behaviour
- Stability and performance of the cell under different temperatures
- Gas quality and the influence of pressurised compartments.
- Faradaic efficiency measurements

## 2 Experimental

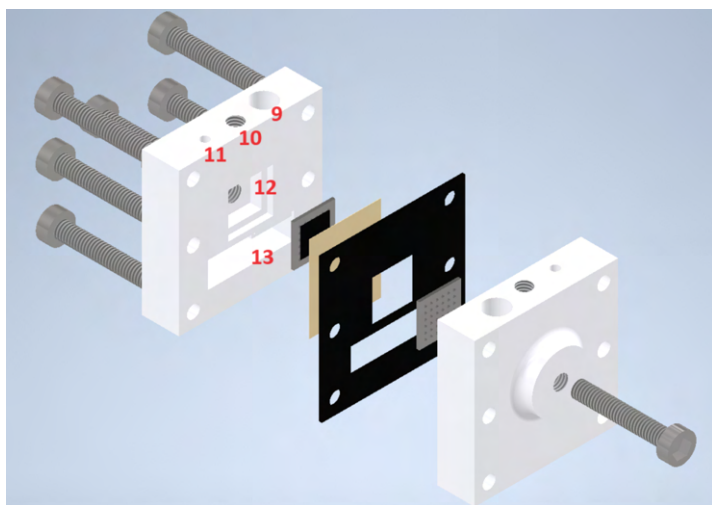
### 2.1 Materials for cell assembly

Clear resin is used for 3D printing of the cell frame. This material is only stable up to 60 °C with 6 M KOH. Peek is used for the cell frame for higher temperatures. The tie bolts and positioning bolts used are made of stainless steel. Furthermore, the perforated bipolar plate is made from stainless steel and measures 1.45 cm x 1.45 cm x 0.1 cm with alternating 1 mm holes to allow gas to escape. The gasket is 1 mm thick PTFE. The membrane is a polyether sulfone separator (PES) with 8  $\mu\text{m}$  pores.

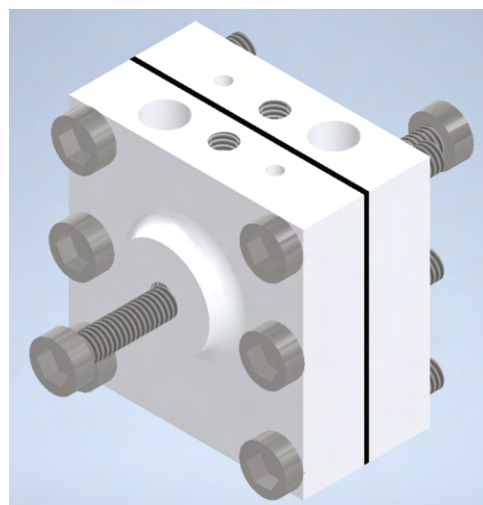
In figures 4a - 4c different views of the 3D sketch are illustrated.



(a)



(b)



(c)

Figure 4: (a) Side view of the cell design. 1) Bipolar plate position bolt 2) Tie bolts 3) Cell frame 4) Perforated bipolar plate (made from stainless steel) 5) Cathode 6) PES separator 7) Gasket 8) Welded anode to a perforated bipolar plate. (b) Rear view of the cell design. 9) Reference electrode insertion 10) Gas outlet 11) Connection to reservoir 12) Gas chamber 13) Liquid reservoir chamber. (c) Rear view of assembled cell.

#### 2.1.1 3D printing

The program Autodesk Inventor Professional 2024 is used to design the cell. With the use of the program PreForm and the 3D printer (formlabs V3) seen in figure 5, the cell is printed using Clear Resin as a filament.

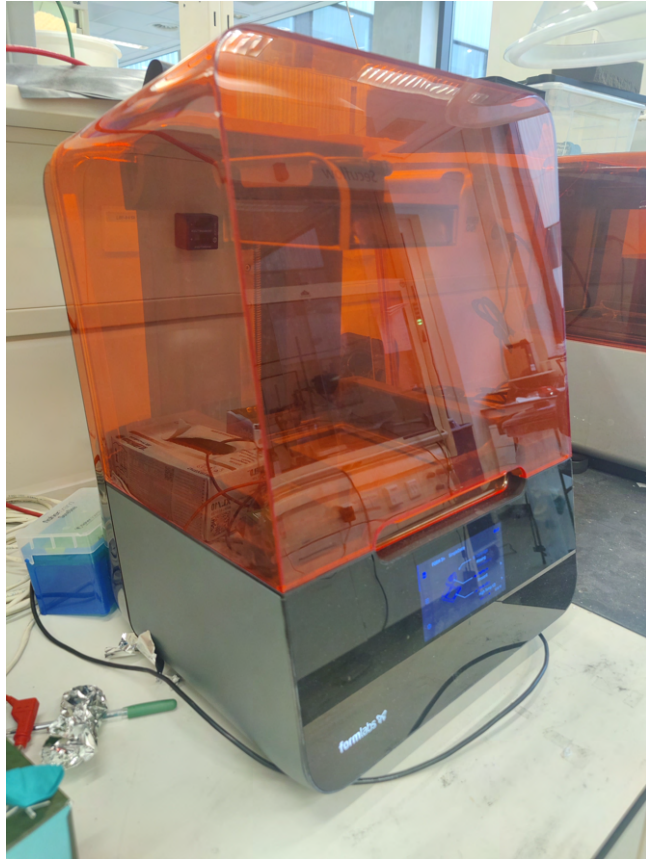


Figure 5: Image of the 3D printer used for printing the cell design.

### 2.1.2 Gasket

The gasket is made out of 1 mm thick PTFE. The design is shown below in figure 6 and cut using the Cricut Maker 3.

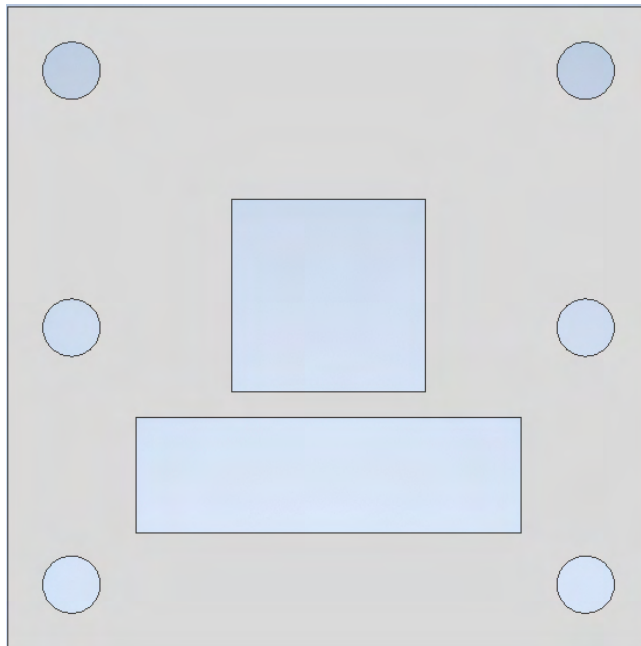


Figure 6: Schematic of the cricut design of the gasket.

## 2.2 Chemicals

$\text{Ni}(\text{NO}_3)_2 \cdot 6\text{H}_2\text{O}$  (Alfa Aesar, 98%),  $\text{FeSO}_4 \cdot 7\text{H}_2\text{O}$  (Sigma-Aldrich,  $\geq 99.0\%$ ), Isopropyl alcohol (VWR Chemicals,  $\geq 98\%$ ), Nafion perfluorinated resin solution (Sigma-Aldrich, 5 wt.% in aliphatic alcohols, contains 15-20% water), 10% Pt on Vulcan XC-72 (FUELCELL Store), Sigracet<sup>TM</sup> 22BB carbon paper (FUELCELL Store), Porous polyether sulfone (PES) filters, 8.0 microns average pore diameter (Sterlitech), Nickel mesh (Dexmet, 40 LPI,  $\emptyset$  120  $\mu\text{m}$ , 500  $\mu\text{m}$  aperture)

## 2.3 Anode preparation

A 1 x 1 cm Ni mesh (40 LPI,  $\emptyset$  120  $\mu\text{m}$ , 500  $\mu\text{m}$  aperture) was cleaned by ultrasonication in isopropyl alcohol for 10 min. The mesh was then pickled in 5 M HCl for 10 min, rinsed with deionised water and dried. Referring to figure 7, the anode is taped with electro-tape on both sides. A rough calculation was done that estimates the active surface area of this mesh, which is approximately 2.7 times smaller than the one reported in Hodges et al. [6]. Electroplating was performed using a 3-electrode cell, comprising the previously prepared Ni mesh working electrode (WE), an oversized Ni foam counter electrode (CE) and Ag/AgCl (3 M NaCl) reference electrode (RE). The electrodes were placed in various (electroplating) solutions, discussed in Appendix B. In the case of the anode preparation method used for further testing, the following method was used:

- 80/20 mixture with  $\text{Ni}(\text{NO}_3)_2 \cdot 6\text{H}_2\text{O}$  (0.24 M) and  $\text{FeSO}_4 \cdot 7\text{H}_2\text{O}$  (0.06 M) (+ the addition of 10 g/L PTFE for one measurement).
- Pulse applied potential of -1 V and 0 V, alternating every 1 second, for 600 seconds in total.
- Drying the plated WE in air overnight before welding to bipolar plate.



Figure 7: Electrotaped anode before electroplating. This is done to ensure metal-metal contact for welding is possible with the bipolar plate and the anode. The area for electroplating is 1x1 cm.

## 2.4 Cathode preparation

The hydrogen-evolving electrode was prepared by cutting and weighing a square area of 5  $\text{cm}^2$  ( $\approx 2.2 \text{ cm} \times 2.2 \text{ cm}$ ) of carbon fibre paper (Sigracet 22BB). Afterwards, a mask is put over the substrate. The substrate is air-brushed with a paint consisting of the following composition:

- 50 mg 10% Pt on Vulcan XC-72, 0.4 mL 5 wt% Nafion solution, 3.33 mL deionised water, 6.67 mL iso-propanol. Roughly 50% of the ink is efficiently sprayed onto the substrate.

The spray pattern is visualised in figure 8. The airbrush is a Hanpose 42HS34P100 and makes use of Universal Gcode Platform to transfer code into actions of the spraycoater. The Hanpose goes from the Home coordinates to the left top corner of the substrate and follows the blue serpentine pattern, where each 180-degree shift has a spacing width of 6 mm (indicated with a purple arrow). Subsequently, the Hanpose makes a shift of 2 mm (indicated with a yellow arrow) to follow the orange serpentine pattern. Lastly, it shifts another 2 mm to follow the green serpentine before going back to the starting point to either perform these steps again or go back to the Home coordinates.

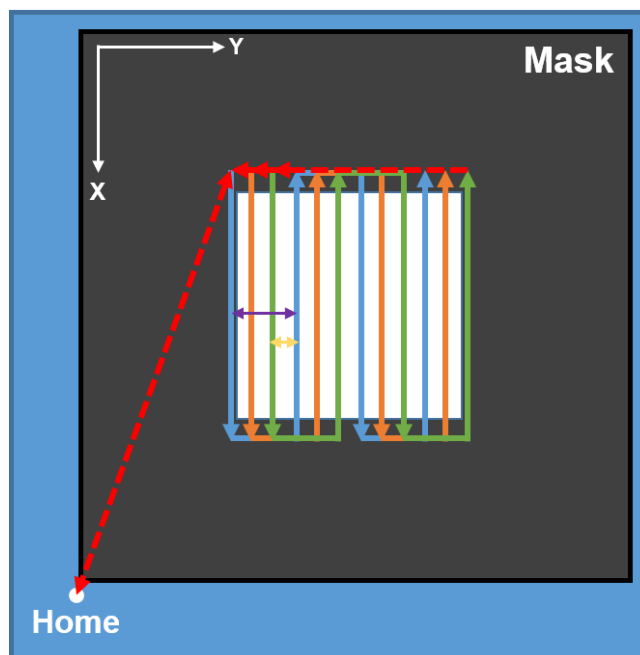


Figure 8: Schematic of the spray pattern done for the HER electrode. The purple arrow represents a spacing of 6 mm. The yellow arrow represents a spacing of 2 mm.

After spraying a loading of  $\sim 0.5 \text{ mg} \cdot \text{cm}^{-2}$ , the electrode is cut into four pieces of  $1 \text{ cm}^2$  area, with some small pieces left for analytical measurements.

## 2.5 Analytical methods

(Electro-)plated and (spray-)coated electrodes were analysed using different analytical techniques. The surface roughness, thickness, and binding of the catalyst were analysed with the use of a Scanning Electron Microscope (SEM). Furthermore, the composition of the surface of the electrodes was analysed by performing Energy-dispersive X-ray (EDX) measurements. Additionally, by performing X-ray powder diffraction (XRD) as a phase identification, the plated material can be compared with reference databases, explained in further detail in the Appendix.

### 2.5.1 Scanning Electron Microscope

A JMS-IT700 Field effect microscope is used to analyse surface structures and layer thicknesses of the prepared electrodes. A small part of the electrodes are cut off and put on carbon tape. The sample is then placed into the JMS-IT700 with a height difference of at least 10.5 mm, where different magnifications are used for different surface images. Typically, the acceleration voltage is between 2.0 kV - 15.0 kV. In this analysis technique, two detectors are used for the JMS-IT700: the Secondary Electron Detector (SED), and the Backscattered Electron Detector (BED-C). The SED is a detector that collects low energy ( $\leq 50 \text{ eV}$ ) to produce a topographic image. The Probe current can also be adjusted, where used values range 30 nA - 50 nA.

### 2.5.2 Energy-dispersive X-ray

Aside from SEM analysis, the JMS-IT700 Field effect microscope can also perform for EDX measurements. An EDX measures the energy and intensity distribution of detected X-ray signals and quantifies this result. The detector used for this measurement is the BED-C and the acceleration voltage is set to 15 kV. Areas used for the measurements are mostly coating layers that are peeled from the material for minimal substrate background noise interfering with the results.

### 2.5.3 Cyclic voltammetry

When testing stability, the cell is tested in an environment of 6 M KOH (14.78 pH). In literature, typically potentials are referenced to RHE, but in this study are translated to Hg/HgO ( $0 \text{ V vs Hg/HgO} = 0.0983 + 0.8748 = 0.9731 \text{ V vs RHE}$  at pH 14.78), expressed in (Eq. 4) [38].

$$E_{RHE}^0 = E_{Hg/HgO}^0 + \left(2.303 \cdot \frac{RT}{F}\right) \cdot pH \quad (4)$$

For OER, cycling between 0.25 V - 0.6 V vs Hg/HgO is done for multiple cycles. For HER, cycling between -1.5 V - -0.8 V vs Hg/HgO is done for multiple cycles.

### 2.5.4 Higher temperature stability

Both electrodes are tested with reference electrodes, and an individual cell potential measurement is done simultaneously. Different currents are applied for a certain time period to check the stability within the cell during gas production. Room temperature, 30 °C, 40 °C, 60 °C and 80 °C are the temperatures used for this type of measurement. To reach these desired temperatures, an oven is preheated an hour before performing the experiment.

### 2.5.5 Gas chromatography

The gasses produced on the anode and cathode sides are measured by piping the output to the GC. In this study the anode outlet is being measured using nitrogen as a carrier gas. The cathode outlet is submerged at a specific water depth to create back pressure. A schematic of this setup can be seen in Figure 9. The GC operates with thermal conductivity detection, a flame ionisation detector and argon, together with nitrogen as the gas carrier. The identification of hydrogen and oxygen is based on their retention times and integrated to determine the relative quantities of gas present. An alternative method employed discussed in Appendix J, involves two gas chromatography (GC) devices which measure oxygen crossover and hydrogen crossover at equal pressures.

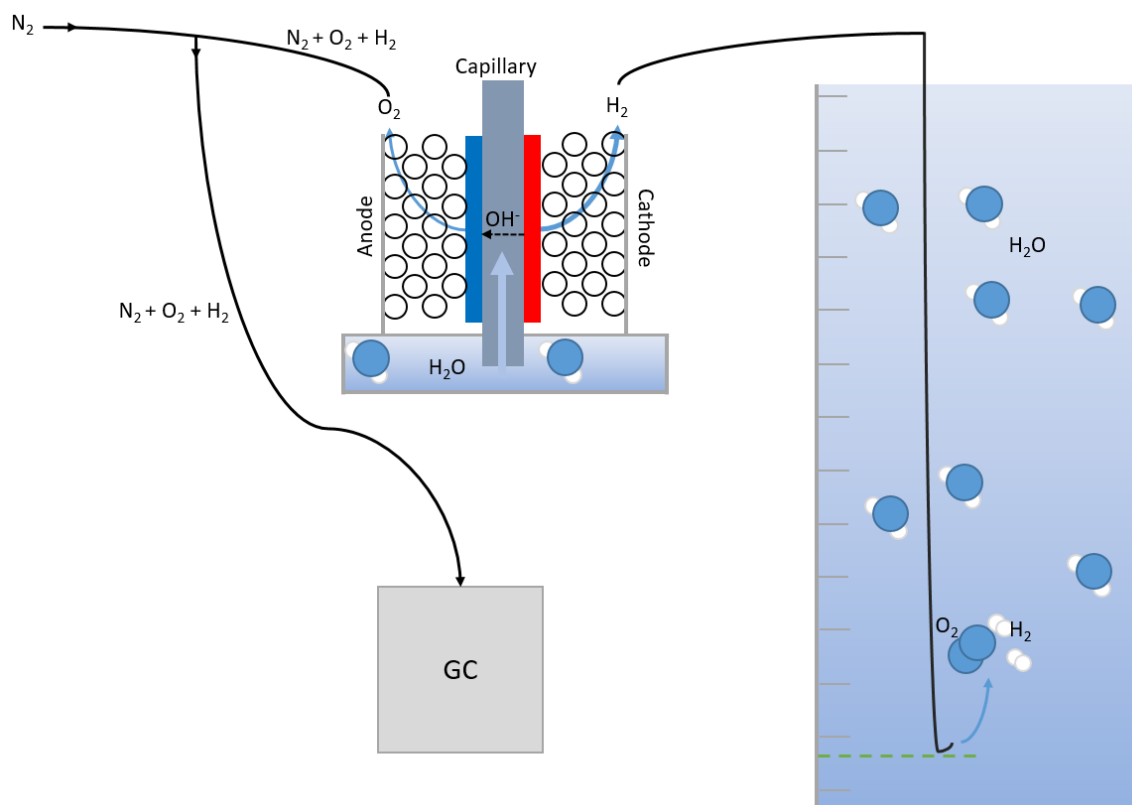


Figure 9: Schematic of the GC setup where the anode outlet is attached to the GC and nitrogen is used as a carrier gas. The cathode outlet is attached to a volume of water for backpressure.

### 2.5.6 Faradaic efficiency

Faradaic efficiency (FE) is calculated via two routes:

- Measure the time it takes to fill a known volume with produced gas (by first completely immersing it in liquid and letting the gas push the water level within this volume down). Divide this with the theoretical volume, calculated via the amount of charge put in. A schematic of this setup can be seen in Figure 10.
- Convert PPM values acquired from the GC data into FE. A detailed description of these calculations can be seen in Appendix H.

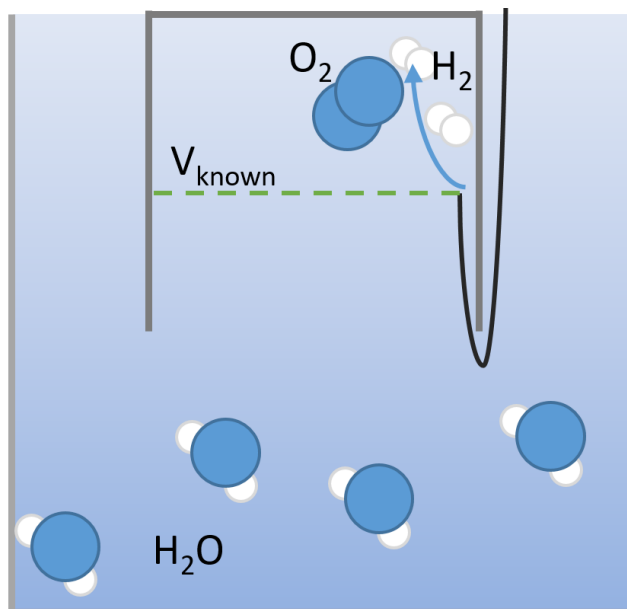


Figure 10: Schematic of the setup to calculate the faradaic efficiency. The gasses push down the liquid level inside the beaker. The gasses are produced until the known volume is filled with gas, where the time this takes is measured.

### 3 Results and discussions

In this section, SEM (Scanning Electron Microscope), EDX (Energy Dispersive X-ray), CV (Cyclic Voltammetry), FE (Faradaic Efficiency) and GC (Gas Chromatography) are used as analytical methods for acquiring experimental data. The electrodes individually underwent SEM, EDX and CV measurements, while the assembled electrodes underwent CV, FE and GC measurements. This data is processed and discussed in this section.

#### 3.1 SEM

A Scanning Electron Microscope (SEM) produces images by beaming electrons onto the surface of the sample in high vacuum. The atoms on the surface themselves emit an electron that is then detected on one of the detectors, typically a secondary electron detector (SED). This information is then transformed into a visible image.

##### 3.1.1 Sigracet 22BB

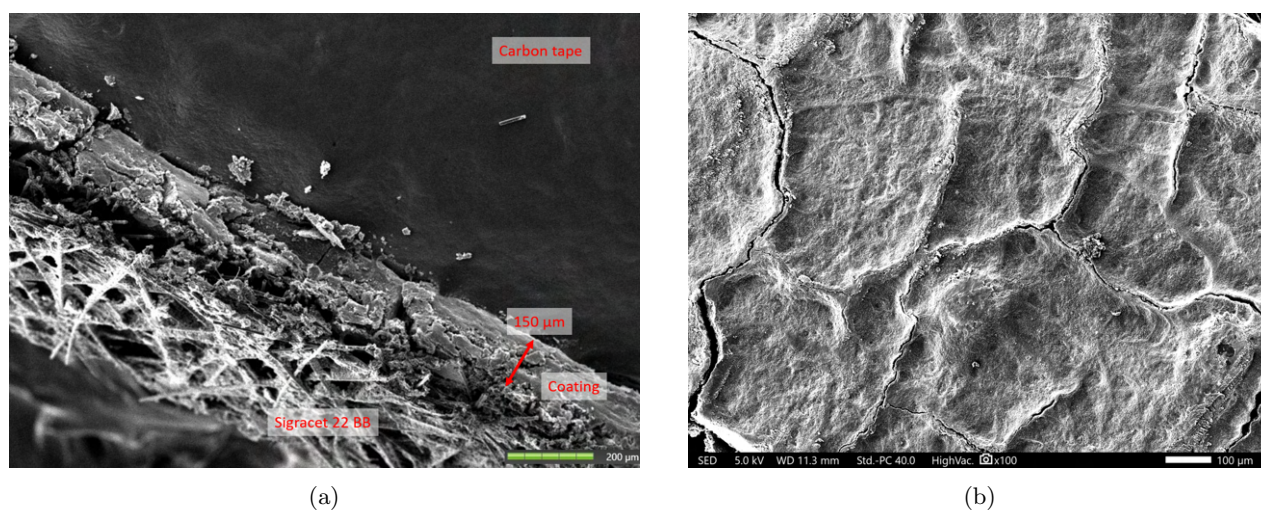


Figure 11: (a) Side view of the cathode showing thickness of the sprayed coating ( $150\ \mu\text{m}$ ). (b) Image of the sprayed surface. Sample has a loading of  $0.48\ \text{mg}/\text{cm}^2$  Pt.

The cathode (Sigracet 22BB substrate) underwent the spray-coating method discussed in the Experimental. The ink used for this preparation consisted of 50 mg 10% Pt on Vulcan XC-72, 0.4 mL 5 wt% Nafion solution, 3.33 mL deionised water and 6.67 mL of iso-propanol. Figure 11a shows that the applied Pt/C coating has a thickness of roughly  $150\ \mu\text{m}$ . The geometric surface area sprayed is  $5\ \text{cm}^2$ , resulting in a coating with a total volume of  $75\ \text{mm}^3$ . When calculating the average density of the particles sprayed on the substrate ( $0.4\ \text{mg}/\text{mm}^3$ ), the total weight of spray-coated ink is 30 mg. A total of 32 mg is sprayed onto the substrate (difference in before spraying and after spraying), ensuring that the mathematical value and analytical value is similar. 25% of the total weight is from Nafion (8 mg), leaving the the rest of the weight to the 10% Pt on carbon black (24 mg). Which comes down to a loading of  $0.48\ \text{mg}/\text{cm}^2$  Pt. The start amount of Pt added was 5 mg, while effectively, the sprayed amount consists of 2.4 mg Pt. Ultimately, the spray-efficiency factor taken into account in the Experimental (50%) for this experiment, was upheld. Figure 11b shows a part of the surface of the coated carbon fibre paper. A rough surface is observed, meaning an increased catalytic surface area.

### 3.1.2 Nickel mesh

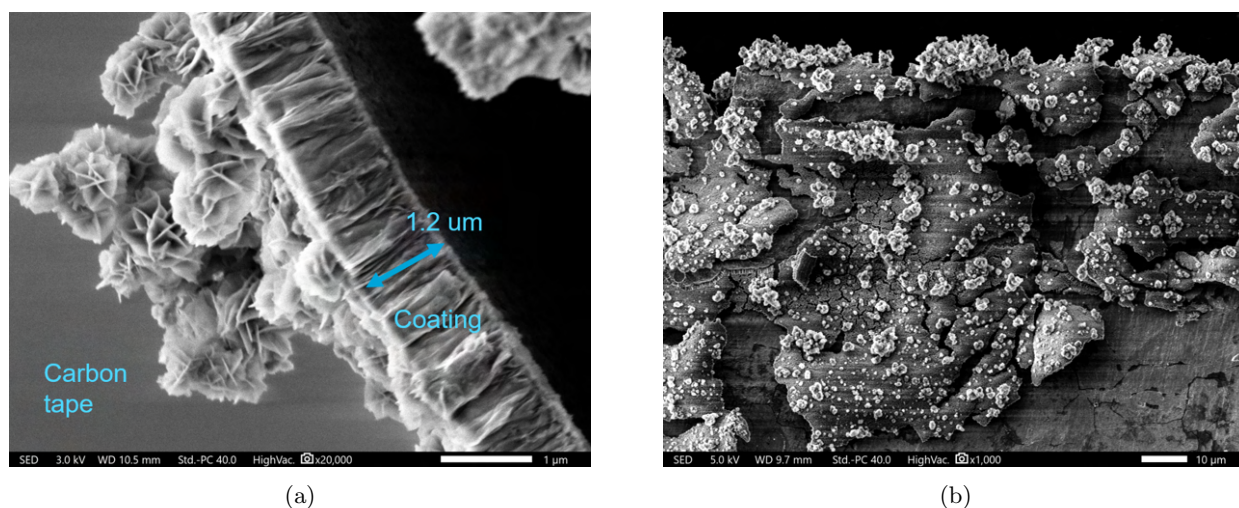


Figure 12: (a) Thickness of the coating ( $1.2 \mu\text{m}$ ). (b) Image of the electrocoated surface. Sample is prepared via pulse applied potential for 300 pulses, using 50/50  $\text{Ni}(\text{NO}_3)_2 \cdot 6\text{H}_2\text{O}$  (0.15 M),  $\text{FeSO}_4$  (0.15 M).

The anode (Nickel mesh) underwent the pulse applied potential method discussed in the Experimental. The composition used for electrocoating in the sample showcased in Figures 12a-12b, consists of  $\text{Ni}(\text{NO}_3)_2 \cdot 6\text{H}_2\text{O}$  (0.15 M) and  $\text{FeSO}_4$  (0.15 M) respectively. Figure 12a shows a peeled-off coating from the substrate. A very homogeneous layer has been deposited, with flakes that increase the surface area. Figure 12b illustrates that the catalytic layer is not present across the whole electrode surface. It is thought that this is mostly due to handling the mesh. The nickel mesh is very bendable, which means that the catalytic layer peels off easily when bending the substrate.

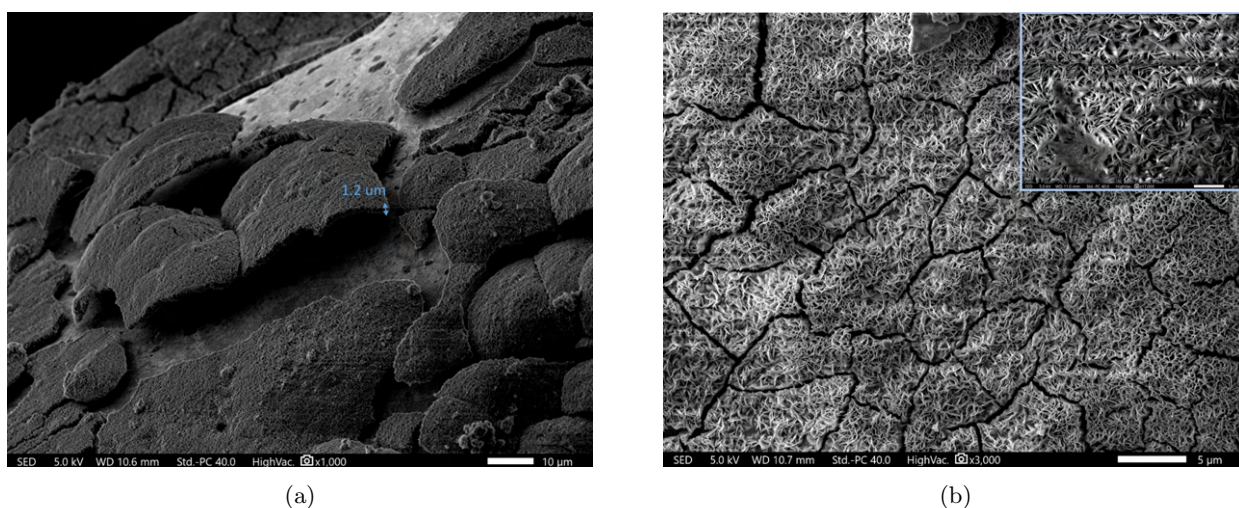


Figure 13: (a) Thickness of the coating ( $1.2 \mu\text{m}$ ). (b) Image of the electrocoated surface. Sample is prepared via pulse applied potential for 300 pulses, using 80/20  $\text{Ni}(\text{NO}_3)_2 \cdot 6\text{H}_2\text{O}$  (0.24 M),  $\text{FeSO}_4$  (0.06 M).

In comparison to Figure 12a and 12b, Figure 13a confirms that the used technique produces the same coating thickness, regardless of using different compositions. The presence of flakes on the surface of the coating is confirmed by Figure 13b, thus showing evidence for a large increase in surface area. For further imaging of the anode samples, please refer to Appendix D.

### 3.2 EDX

An additional feature of the JMS-IT700 is the possibility to perform an Energy-dispersive X-ray (EDX) analysis. EDX is an analytical technique used for the chemical characterisation of a sample, which relies on the basis that each element has a unique set of peaks on the electromagnetic emission spectrum. The incident beam can excite an electron of an atom in the inner shell to a higher energy state, leaving an electron hole behind. An electron from an outer, higher energy shell, then fills this hole, together with the release of energy, in the form of x-ray emission, which is measured by a detector.

An EDX measurement is useful to analyse what the elemental composition of the material is, by either mapping a small, selected area (e.g. coated area or completely non-coated area), or by scanning a whole area, where both coating and bare substrate is present. Table 1 presents the elemental composition of the coated nickel mesh obtained by calculating the average over 6 selected areas of the sample, prepared via pulse applied potential, for 300 pulses, using the precursors  $\text{Ni}(\text{NO}_3)_2 \cdot 6\text{H}_2\text{O}$  (0.15 M) and  $\text{FeSO}_4$  (0.15 M). The peak intensity and example of the areas used for EDX measurements to establish the average can be found in Appendix G.

| Element      | Atom%       | Weight%     |
|--------------|-------------|-------------|
| Ni           | 9.54        | 20.61       |
| Fe           | 16.70       | 34.43       |
| O            | 62.27       | 37.27       |
| C            | 7.99        | 3.53        |
| S            | 3.51        | 4.15        |
| <b>Total</b> | <b>100%</b> | <b>100%</b> |

Table 1: EDX table of the 50/50  $\text{Ni}(\text{NO}_3)_2 \cdot 6\text{H}_2\text{O}$  (0.15 M) and  $\text{FeSO}_4 \cdot 7\text{H}_2\text{O}$  (0.15 M) sample. A total of 6 measurements are done to establish the average.

By removing the values for O, C and S, taken from Table 1, the ratio of Ni/Fe, based on the Atom% is 35/65. This value is substantially different from the initial precursor ratio (50/50). It is known from literature that a ratio of 80/20 Ni/Fe improves the electronic conductivity relative to no Fe present, resulting in improved OER performance [39].

| Element      | Atom%       | Weight%     |
|--------------|-------------|-------------|
| Ni           | 16.06       | 34.9        |
| Fe           | 9.74        | 20.34       |
| O            | 64.72       | 38.53       |
| C            | 7.86        | 3.61        |
| S            | 2.03        | 2.42        |
| <b>Total</b> | <b>100%</b> | <b>100%</b> |

Table 2: EDX table of the 80/20  $\text{Ni}(\text{NO}_3)_2 \cdot 6\text{H}_2\text{O}$  (0.24 M) and  $\text{FeSO}_4 \cdot 7\text{H}_2\text{O}$  (0.06 M) sample. A total of 7 measurements are done to establish the average.

Initially, a precursor ratio of 50/50 Ni/Fe was selected, resulting in a coating consisting of a ratio deviating from the ideal proportions. Subsequently, in the preparation of the coating, a precursor ratio of 80/20 Ni/Fe was employed, revealing a composition of 62/38 Ni/Fe in the coating, as seen in Table 2. Although still falling short of the better-performing ratio, this ratio comes closer compared to the 50/50 precursor ratio. Examples of the areas used for the EDX calculations can be found in Appendix G.

| Element      | Atom%       | Weight%     |
|--------------|-------------|-------------|
| Ni           | 15.83       | 35.35       |
| Fe           | 4.57        | 9.73        |
| O            | 50.06       | 32.15       |
| C            | 12.74       | 6.32        |
| S            | 1.76        | 2.20        |
| F            | 11.93       | 8.60        |
| K            | 3.39        | 5.65        |
| <b>Total</b> | <b>100%</b> | <b>100%</b> |

Table 3: EDX table of the 80/20  $\text{Ni}(\text{NO}_3)_2 \cdot 6\text{H}_2\text{O}$  (0.24 M) and  $\text{FeSO}_4 \cdot 7\text{H}_2\text{O}$  (0.06 M) sample together with the addition of PTFE. A total of 9 measurements are done to establish the average.

Excluding the values of O, C, S, F and K, the Ni/Fe ratio taken from Table 3 is 78/22, coming close to the optimal 80/20 ratio. Examples of the areas used for the EDX calculation can be seen in Appendix G together with the EDX values after using the electrodes in the zero-gap cell formation.

Interestingly, the anode coating is not stable when implementing the electrode in the zero-gap cell design. Table 4 shows the wt% of iron, concluding almost complete depletion of the coating. The wt% of oxygen is also relatively low, but this is mainly because the areas measured were on nickel substrate instead of islands of coating that are not in contact with the substrate. The presence of  $\text{Ni}(\text{OH})_2$  could therefore still be there, but in very small amounts (and without iron). SEM images of the surface can be seen in Appendix G.

| Element      | Atom%       | Weight%     |
|--------------|-------------|-------------|
| Ni           | 48.80       | 77.04       |
| Fe           | 0.71        | 1.05        |
| O            | 15.31       | 7.33        |
| C            | 33.02       | 11.97       |
| Al           | 0.04        | 0.03        |
| K            | 2.11        | 2.58        |
| <b>Total</b> | <b>100%</b> | <b>100%</b> |

Table 4: EDX table of the 80/20  $\text{Ni}(\text{NO}_3)_2 \cdot 6\text{H}_2\text{O}$  (0.24 M) and  $\text{FeSO}_4 \cdot 7\text{H}_2\text{O}$  (0.06 M) after using the electrode in the zero-gap cell design. A total of 7 measurements are done to establish the average.

### 3.3 Cathode cyclic performance

The HER electrode is tested for stability and the onset of hydrogen formation, as is the OER electrode for the onset of oxygen formation. Figure 14a illustrates the bare Sigracet 22BB performance of HER, where the onset of the  $\text{H}_2$  formation is at  $\sim -0.9$  V vs Hg/HgO. Compared to Figure 14b, the HER current consumption of the bare carbon fibre paper is very little. The spray-coated carbon fibre paper (Sigracet 22BB), containing in this measurement  $\sim 0.3$   $\text{mg}/\text{cm}^2$  Pt loading, has the same onset ( $\sim -0.9$  V vs Hg/HgO), but a much higher current consumption due to the catalytic activation. Here, the maximum potential for cycling is at  $-0.5$  V vs Hg/HgO, which is close to the oxidation of Pt to PtO ( $0.3$  V vs RHE), seen in Pourbaix diagrams from literature [40]. The oxidation peak seen in this graph, is due to hydrogen oxidation. When scanning in the positive direction, the hydrogen that is still present inside the porous structure is oxidized, as seen in literature [41]. It is clear that the platinum-coated carbon fibre paper is relatively stable in terms of current consumption compared to the platinum wire. Considering Figure 14c, which is a platinum wire cycled between  $-1.2$  V and  $-0.8$  V vs Hg/HgO, the current consumption decreases after every cycle. It was observed that this decrease is due to bubbles sticking to the surface of the wire, reducing the active surface area.

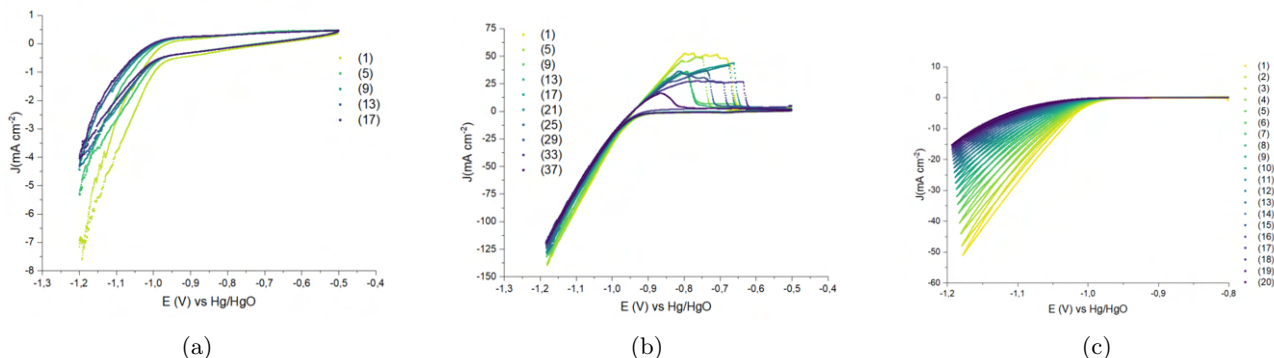


Figure 14: (a) Bare Sigracet 22BB, cycling between -1.2 V - -0.5 V (vs Hg/HgO), scanrate = 10 mV/s, cycles 1, 5, 9, 13 and 17 are shown. (b) Spray coated Sigracet 22BB with 0.3 mg/cm<sup>2</sup> loading, cycling between -1.2 V - -0.5 V (vs Hg/HgO), scanrate = 10 mV/s, cycles 1, 5, 9, 13, 17, 21, 25, 29, 33 and 37 are shown. (c) Platinum wire, cycling between -1.2 V - -0.8 V (vs Hg/HgO), scanrate = 10 mV/s, cycles 1 up to 20 are shown.

### 3.4 Anode cyclic performance

Throughout the project, different approaches to anode plating were performed. In general, Ni(OH)<sub>2</sub> is oxidised to NiOOH which is known in literature to be a good catalyst for the oxygen evolution reaction [39]. The general redox reaction is given by:

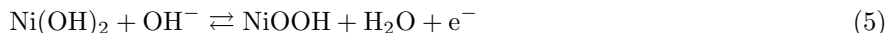


Figure 15a illustrates the CV measurement of a sample where the composition for plating was 70/30 Ni(NO<sub>3</sub>)<sub>2</sub>·6H<sub>2</sub>O (0.21 M) and FeSO<sub>4</sub>·7H<sub>2</sub>O (0.09 M), where the sample was dried for a day before testing the performance of the electrode. Prior to the OER, two peaks were present. The less intense peak is from the β-phase, while the more intense peak is from the α-phase of Ni(OH)<sub>2</sub>. What can be seen from this graph is that the OER performance is decreasing throughout cycling. The onset of OER is approximately at 525 mV. Figure 15b has the same conditions as the previous experiment, except that after plating, it is immediately put into KOH for one hour before testing the performance of the electrode. The onset of OER is approximately at 513 mV. In this graph, two peaks correspond to the alpha and beta phases of Ni(OH)<sub>2</sub>, while an additional peak before the β peak, is more frequently observed in literature but remains largely unexplored in terms of its relation to any specific reaction [42, 43]. This extra peak is believed to be influenced by the substrate, particularly nickel, as it is exclusively observed in the presence of nickel substrates in literature and not on other substrates. The slight shift is primarily attributed to variations in coverage of the catalyst coating (containing iron and nickel). Parts of the surface, without catalyst, allow bare nickel to undergo transformation into nickel hydroxide due to high pH, as depicted in the Pourbaix diagram in Figure 16. Literature suggests that the introduction of iron leads to a shift in the oxidation (and reduction) peak from Ni(OH)<sub>2</sub> to NiOOH to a more positive potential [44]. However, as the uncoated section lacks iron, this shift is absent, causing the peak to initiate at a less positive potential.

The CV measurement with the composition of 50/50 Ni(NO<sub>3</sub>)<sub>2</sub>·6H<sub>2</sub>O/FeSO<sub>4</sub>·7H<sub>2</sub>O (0.15 M both) can be seen in Figure 15c. Interestingly, the Ni(OH)<sub>2</sub> oxidation and reduction peaks are very minimal compared to OER. Furthermore, the OER did not seem to reduce much throughout cycling. The OER onset is at approximately 508 mV. Similarly, the 80/20 Ni(NO<sub>3</sub>)<sub>2</sub>·6H<sub>2</sub>O/FeSO<sub>4</sub>·7H<sub>2</sub>O (0.24 M/0.06 M) sample is shown in Figure 15d. The OER peak is not as intense as other samples (with an onset of 522 mV), but relatively in the same range. Again, three oxidation and reduction reactions happen in this system, where only peak two and three can be recognized for the β-phase and α-phase of Ni(OH)<sub>2</sub> with Fe and the first peak to be Ni(OH)<sub>2</sub> without iron. The last CV experiment, with the composition of 80/20 Ni(NO<sub>3</sub>)<sub>2</sub>·6H<sub>2</sub>O/FeSO<sub>4</sub>·7H<sub>2</sub>O and the addition of 10 g/L PTFE, is seen in Figure 15e. The OER does relatively well in this experiment, which could be influenced by better gas removal due to the aerophilic properties of the PTFE. Here, the OER onset is at approximately 518 mV. The final Figure 15f summarizes all previously mentioned experiments, showing the 20th cycle of all samples. All electrodes are approximately in the same range of the OER onset potential, while showing clear shifts for the onset potentials of the reduction and oxidation reactions of the Ni(OH)<sub>2</sub> material. This shift is typically caused by the addition of iron, as seen in literature [44].

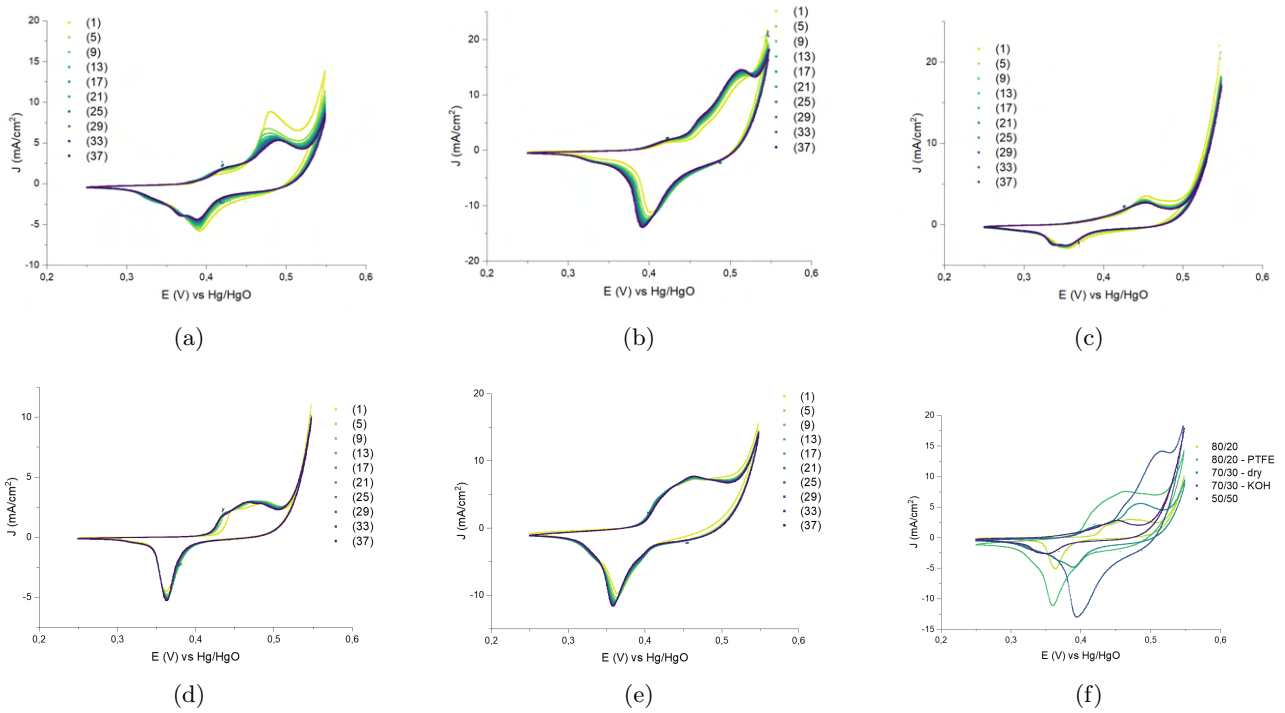


Figure 15: (a) 70/30 Ni/Fe ratio (dried for one day after plating), cycling between 0.25 V - 0.55 V (vs Hg/HgO), scanrate = 10 mV/s, cycles 1, 5, 9, 13, 17, 21, 25, 29, 33 and 37 are shown. (b) 70/30 Ni/Fe ratio (submerged in KOH for 1 hour before cycling), cycling between 0.25 V - 0.55 V (vs Hg/HgO), scanrate = 10 mV/s, cycles 1, 5, 9, 13, 17, 21, 25, 29, 33 and 37 are shown. (c) 50/50 Ni/Fe ratio (dried for one day after plating), cycling between 0.25 V - 0.55 V (vs Hg/HgO), scanrate = 10 mV/s, cycles 1, 5, 9, 13, 17, 21, 25, 29, 33 and 37 are shown. (d) 80/20 Ni/Fe ratio (dried for 24 hours after plating), cycling between 0.25 V - 0.55 V (vs Hg/HgO), scanrate = 10 mV/s, cycles 1, 5, 9, 13, 17, 21, 25, 29, 33 and 37 are shown. (e) 80/20 Ni/Fe ratio with 10 g/L PTFE (dried for 24 hours after plating), cycling between 0.25 V - 0.55 V (vs Hg/HgO), scanrate = 10 mV/s, cycles 1, 5, 9, 13, 17, 21, 25, 29, 33 and 37 are shown. (f) 20th cycle of all previously mentioned experiments (70/30, 70/30-KOH, 50/50, 80/20, 80/20-PTFE).

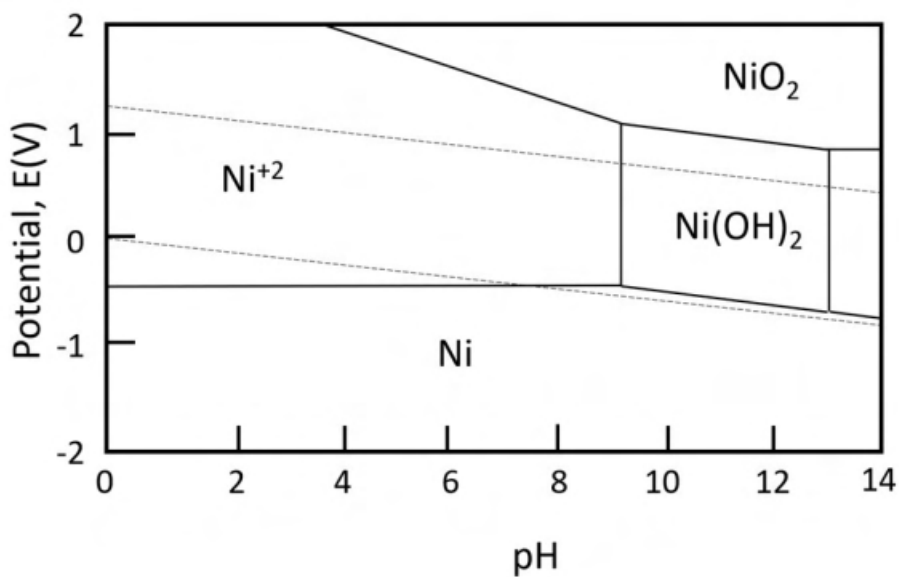


Figure 16: Pourbaix diagram of Nickel (Ni), reproduced from Singh et al. [45].

### 3.5 Alkaline cell performance

The electrodes have been thoroughly tested individually on their performance and stability. However, the electrodes had not been assembled into a cell up to this stage. Before proceeding with the zero-gap cell, it is important to see whether there are any fluctuations, deviations, or reactions happening in a normal alkaline cell. The absence of side reactions through the whole cycle range of 0–1.6 V (no reference) is confirmed by Figure 17a. Figure 17b illustrates a more detailed view of the range where the anode oxidizes and reduces, right before OER. The cell potential starts to generate OER at an onset potential of approximately 1.48 V.

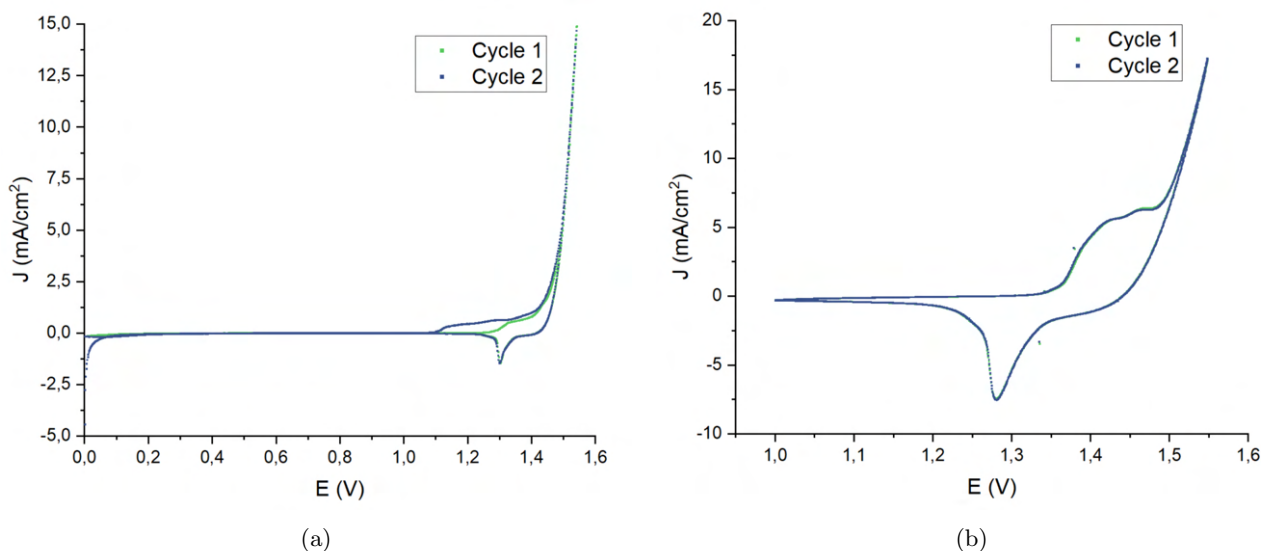


Figure 17: (a) Full range cycling between 0.0 V - 1.6 V. RE is attached with the CE. Scan rate = 10 mV/s. Illustrating the first and second cycle. WE = anode, CE = cathode. (b) Cycling between 1.0 V - 1.6 V. RE is attached with the CE. Scan rate = 10 mV/s. Illustrating the first and second cycle. WE = anode, CE = cathode.

### 3.6 Zero-gap cell performance

#### 3.6.1 Cell performance at room temperature

The stability and performance of the cell setup have been assessed through multiple experimental sessions. Figures 18a-18c indicate poor stability of the cell under constant current conditions at room temperature. While conducting GC measurements, the gasses are produced by applying a constant current (for stable gas production), where the applied potential is measured. Based on Ohm's law, a constant current paired with an increasing potential indicates an increase in resistance. Theoretically, there are several factors that contribute to the overpotential induced by (ohmic) resistance, the main factors potentially being caused by bipolar plates, electrolyte, contact resistance, and membranes [46]. The bipolar plates could not cause a sudden shift in potential, as the plates remain stationary and do not exhibit abrupt changes in conductivity (with the exception of a minor amount of corrosion). In terms of contact resistance, the same argument can be applied in terms of movement; however, the accumulation of bubbles could increase contact resistance between electrodes and the membrane, and the release of said bubble would decrease the resistance once again. Upon analysing the graphs, it becomes apparent that fluctuations increase over time, suggesting that a continuous buildup and release of bubbles may not be the sole reason for variations in resistances. The membrane and electrolyte are closely interconnected, with the membrane serving as an electrolyte supplier. Two hypotheses related to this are either ionic accumulation or a deficient supply of electrolyte. The ion buildup, as described in the introduction, leads to decreased conductivity. The deficient supply of electrolyte results in a significant increase in resistance owing to inadequate replenishment of the generated current. It is unclear at this stage which of these hypotheses hold true.

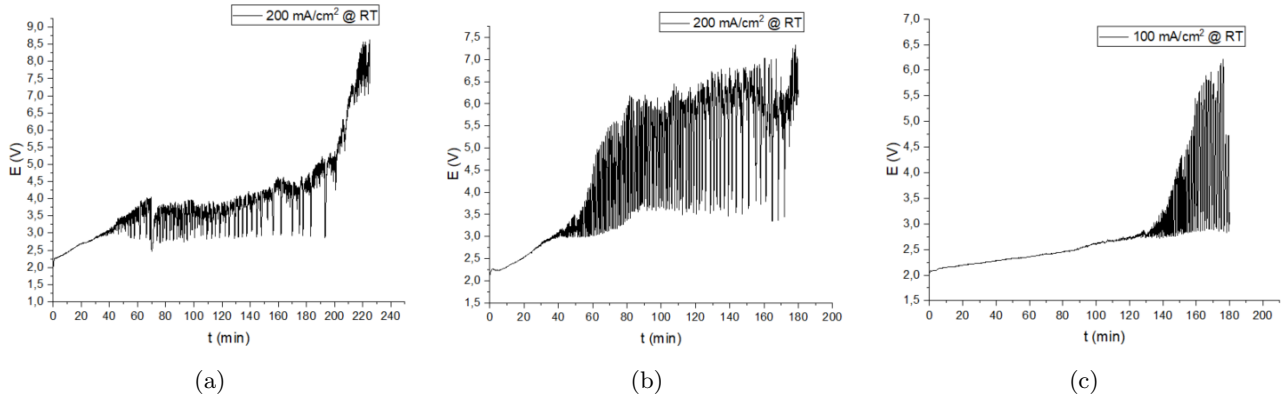


Figure 18: (a) Cell performance for constant current ( $200 \text{ mA/cm}^2$ ) depicts poor stability; the current supply can only be upheld going up to 9 V, where up to 40 minutes the fluctuations are kept at a minimum. (b) Cell performance for constant current ( $200 \text{ mA/cm}^2$ ) depicts poor stability; the current supply can only be upheld going up to 7.5 V, where up to 40 minutes the fluctuations are kept at a minimum. (c) Cell performance for constant current ( $100 \text{ mA/cm}^2$ ) depicts poor stability; the current supply can only be upheld going up to 6.5 V, where up to 120 minutes the fluctuations are kept at a minimum.

### 3.6.2 Cell performance at higher temperatures

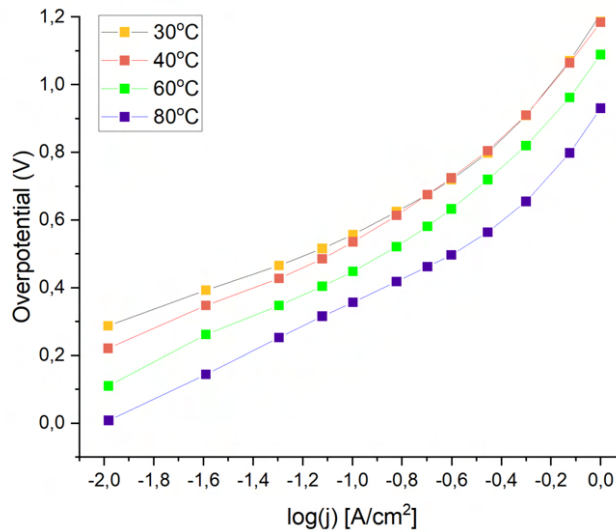


Figure 19: Experimental data showing a change in potential with different temperatures and different currents (plotted on a logarithmic scale).

The graph depicted in Figure 19 illustrates the overpotential (difference between the generated potential and thermoneutral potential) required to achieve a specific current. These calculations account for the shift in thermoneutral voltage resulting from temperature variations, as depicted in Figure 20 [47]. In general, it is evident that elevated temperatures lead to water splitting at lower overpotentials, primarily attributed to a decrease in (ohmic) resistance from the electrolyte. Moreover, an increase in current densities corresponds to an increase in overpotential. This increase is attributed to the sluggish transport of reactants from the electrolyte to the electrode surface and also to transport from the surface away from the electrode, blocking the active surface area [48].

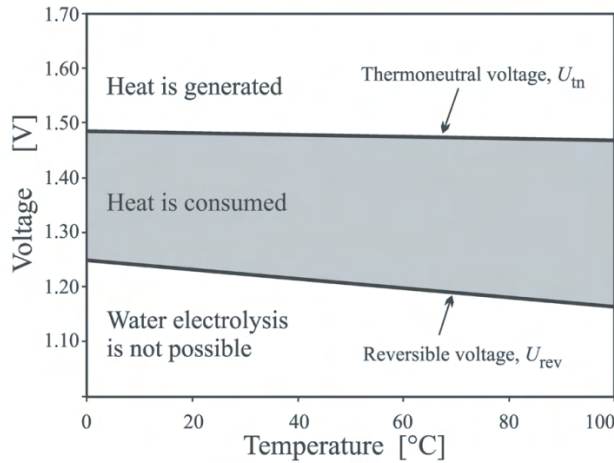


Figure 20: Graph of water splitting regime at different temperatures, reproduced from Mori et al. [47].

At elevated temperatures, water splitting requires lower overpotential, as deduced from both the obtained results and relevant scientific literature [47, 49]. Furthermore, the generation of higher current densities results in increased overpotential. The room-temperature experiments reveal that the cell exhibits instability when subjected to current densities exceeding  $100 \text{ mA/cm}^2$ . Four elevated temperature experiments ( $30 \text{ }^\circ\text{C}$ ,  $40 \text{ }^\circ\text{C}$ ,  $60 \text{ }^\circ\text{C}$  and  $80 \text{ }^\circ\text{C}$ ) each spanning 15 hours are presented in Figures 21a - 21d. These graphs collectively indicate that potential fluctuations are less pronounced at higher temperatures and lower current densities. These fluctuations are based on bubble formation and removal, as discussed before. Despite the fluctuations in potential, a consistent rise in potential over time is observed in all measurements. The experiment at  $80 \text{ }^\circ\text{C}$ , shows a stabilising drop in potential before a steady increase (as seen in all different current densities at this temperature).

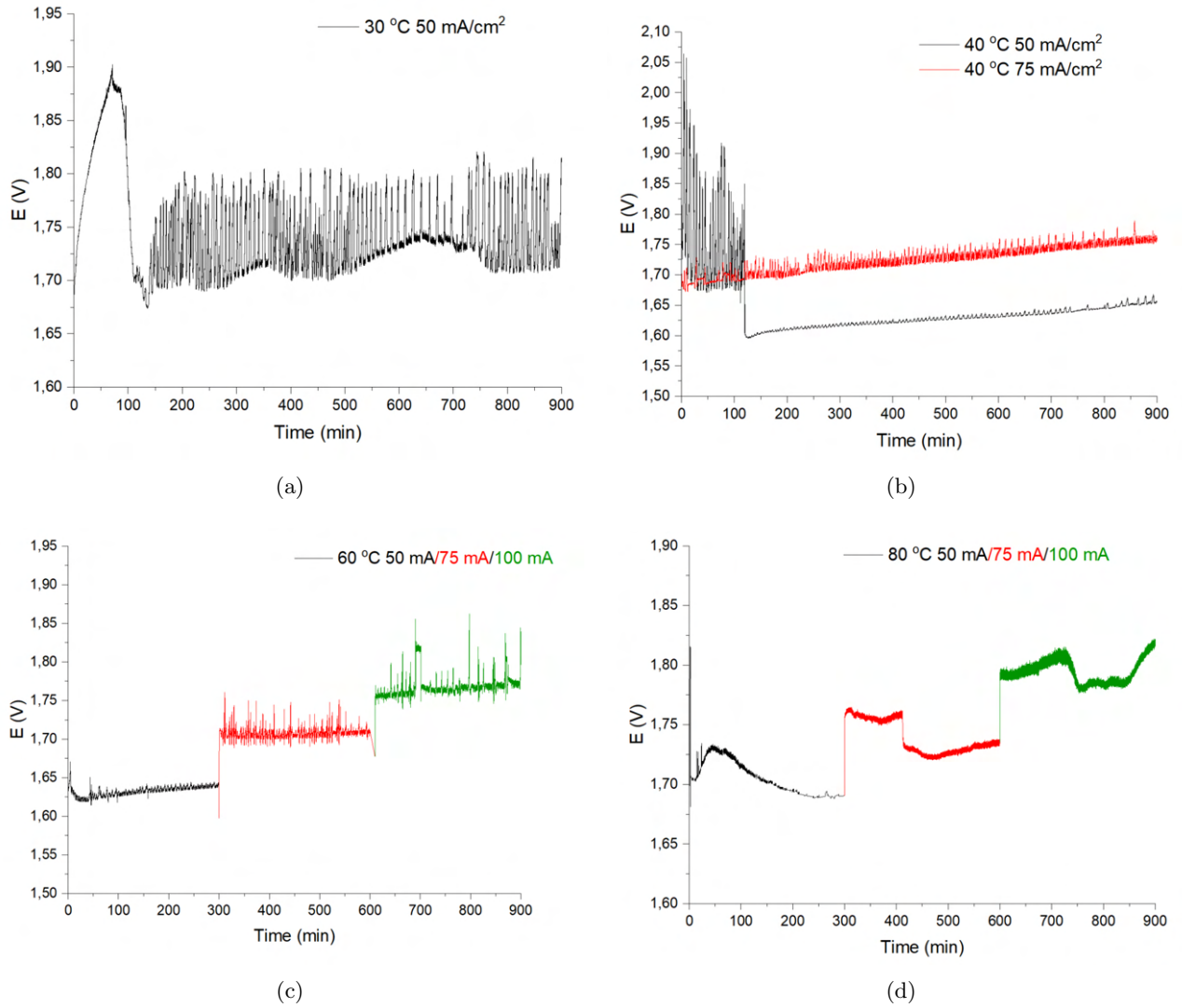


Figure 21: (a) Cell performance for 15 h at 30 °C at 50 mA/cm<sup>2</sup>. (b) Cell performance for 15 h at 40 °C at 50 mA/cm<sup>2</sup> and 15 h at 75 mA/cm<sup>2</sup>. (c) Cell performance for 15 h in total, at 60 °C at 50 mA/cm<sup>2</sup>, 75 mA/cm<sup>2</sup> and 100 mA/cm<sup>2</sup> (5 hours each). (d) Cell performance for 15 h in total, at 80 °C at 50 mA/cm<sup>2</sup>, 75 mA/cm<sup>2</sup> and 100 mA/cm<sup>2</sup> (5 hours each).

### 3.6.3 Faradaic Efficiency

The first method to acquire the faradaic efficiency (FE) discussed in the Experimental section is performed using: (Eq. 6-8)

$$n_0 = \frac{Q}{F} \quad (6)$$

$$V_0 = \frac{n_0 \cdot R \cdot T}{P} \quad (7)$$

$$FE = \frac{V}{V_0} \quad (8)$$

These equations assume the ideal gas law, which is assumed to closely represent experimental conditions in this system. The following parameters are used for this experiment:

- The known volume to be filled was 20 mL ( $V$ ).
- The applied current density was 300 mA/cm<sup>2</sup>.

- The gas was produced in an oven at a temperature of 80 °C.
- The gas was captured in a beaker filled with water at room temperature.

The time it took to fill a volume of 20 mL with gas was approximately 390 seconds. Considering the applied current density, the total amount of charge put in is 117 C. Following Eq. 6, the theoretical gas production relates to 0.0012 moles of gas. Based off Eq. 7, the theoretical volume this amount of moles should acquire is  $\sim 29$  mL ( $V_0$ ). Comparing both the theoretical and experimental volume, the FE in this experiment is  $\sim 69\%$ . However, this experiment does have a relatively large error margin, as the time it takes for the gas to reach this volume could deviate by more than 10 seconds. Alongside the fact that the error could be increased further by the relative uncertainty in temperature and pressure, which was not taken into account in this experiment. The FE is not a 100% for one main reason: The current collectors and position bolts are made of stainless steel, a material that is unstable in alkaline environments when potential is applied. The Pourbaix diagram extracted from literature shows multiple oxidation reactions occur on the surface of stainless steel (mainly at the cathode side, since a negative potential is applied to the current collector) [50]. Consequently, the (in)stability of the current collector becomes apparent during the cycling of the cell, as depicted in Figure 22.

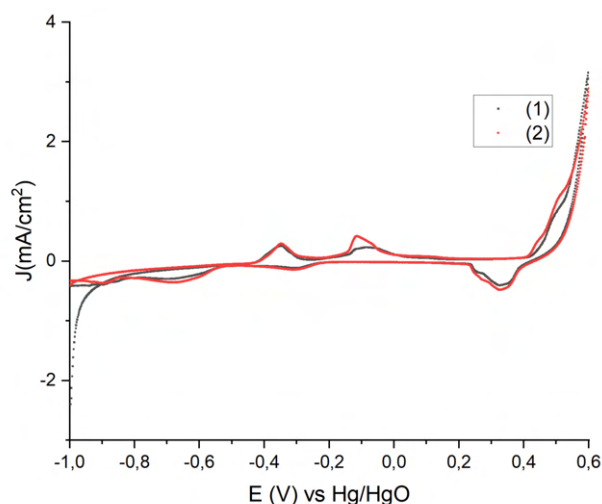


Figure 22: Experimental data showing the cathode and anode performance with the Hg/HgO referenced at the anode. Showing the first and second cycles, scanrate = 2 mV/s. The instability of the stainless steel current collector is expressed in oxidation and reduction reactions aside from the regular nickel reactions.

Regarding the observed oxidation and reduction peaks in the above-mentioned graph, except from the easily distinguishable nickel peaks, it is believed that these are primarily attributed to the presence of iron, leading to the formation of iron oxides. Some of these iron oxides undergo reversible transformations back into iron, while others engage in irreversible reactions resulting in a loss of conductivity. Figure 23 illustrates that the reactions possible at such elevated pH and potential include the oxidation to  $\text{Fe}_2\text{O}_3$  and  $\text{Fe}_3\text{O}_4$ .

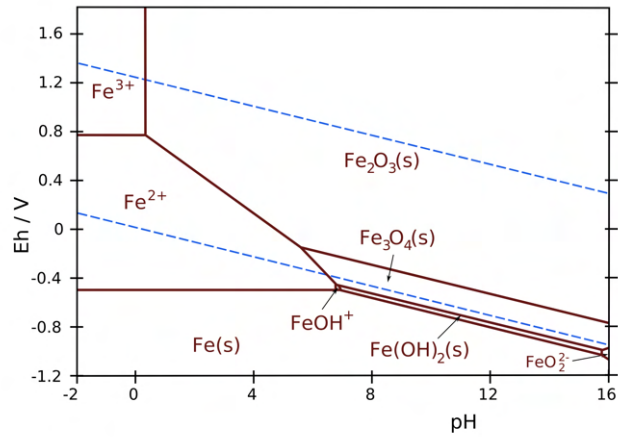


Figure 23: Pourbaix diagram for iron at ionic concentrations of 1.0 mM. Extracted from [51].

A less prominent reason for the lack of near-100% FE is that the cell is not completely airtight. In theory, the current cell design cannot simply be air-leak-free as the positioning bolts are rotating, making it extremely difficult to have hermetic sealing. Applying Teflon tape around the positioning bolts was undertaken to ensure more hermetic sealing (yet, a 100% hermetically sealed cell was not attained). An experiment was performed to investigate gas bubbles forming outside of the cell by putting the setup in a bath of water. Argon gas was pumped through one of the gas outlets. While the remaining (other) gas outlet was attached to an external beaker filled with water. The depth of the water in this beaker was greater, resulting in higher back pressure compared to the surrounding water around the cell. This made the flow of the gas slightly more favorable to any air leakages within the cell. The experimental observation revealed that, in relation to the volume of gas being pumped through the other outlet, smaller bubbles were forming in lower quantities where the positioning bolt entered the cell. Comparatively, the amount of leaking gas is negligible and would not affect the FE significantly.

A second method described in the Experimental is by converting values acquired in the GC into FE. The approach to doing so can be found in Appendix H. Every injection in the GC measures the presence of hydrogen or oxygen, integrates the area of the peak, and translates this into a PPM (parts per million) value. In Figure 24a the change in FE during measurement at different current densities can be seen. There is a large fluctuation at the beginning of different current densities due to the time it takes for the system to reach equilibrium. Several experiments regarding gas purity also included measuring the FE. Figures 24b and 24c show the FE values with backpressure applied, where the current density is either 100 mA/cm<sup>2</sup> or 200 mA/cm<sup>2</sup>. The FE for 100 mA/cm<sup>2</sup> is higher (approximately around 78%) than that of 200 mA/cm<sup>2</sup> (approximately 70%). This generally makes sense, as higher current densities mean faster kinetics are needed, resulting in a less efficient system. More FE measurements, calculations, and the mass flow meter (MFM) measurement can be found in Appendix H.

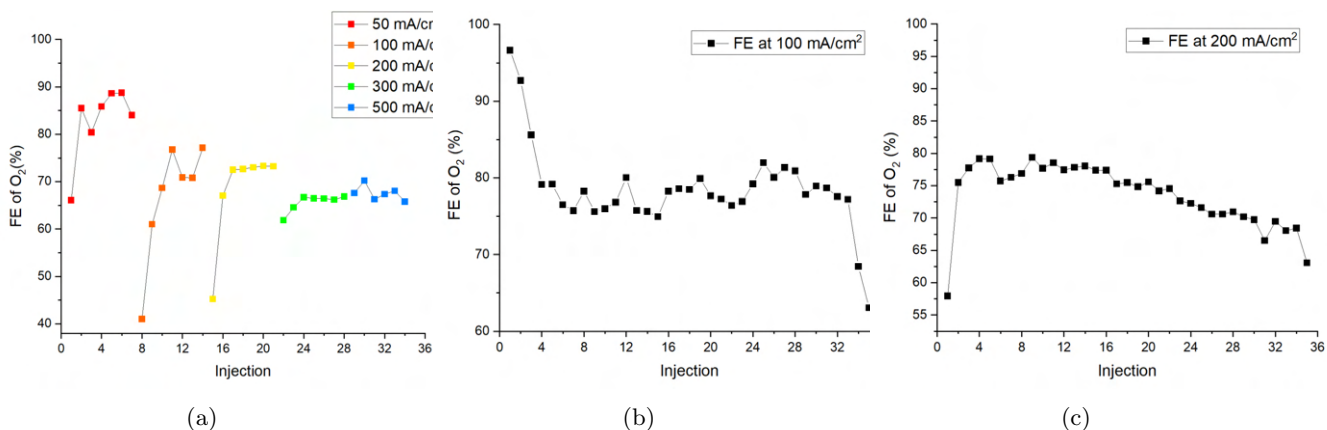


Figure 24: (a) FE of 5 different current densities. Only the O<sub>2</sub> side is measured, and no backpressure was applied on the H<sub>2</sub> side. The carrier gas flow was set to 8 mL/min. (b) FE measurement at a constant current of 100 mA/cm<sup>2</sup>. The gas was carried by 7 mL/min of N<sub>2</sub>. (c) FE measurement at a constant current of 200 mA/cm<sup>2</sup>, carried with 10 mL/min of N<sub>2</sub>.

### 3.6.4 Ion accumulation

As discussed in the Introduction, a potential phenomenon occurring during measurements is the accumulation of the OH<sup>-</sup> and K<sup>+</sup> ions, potentially leading to increased resistance or salt formation by exceeding solubility limits or a reaction with the present CO<sub>2</sub> gas in the gas chamber. Results obtained up to this stage show no conclusive evidence indicating the cause of increased resistance. Aside from the poor cell performance, the continual increase in applied potential over time appears to be attributable to a decrease in conductivity; however, the latter phenomenon is evident at all measured temperatures for using the cell for extended durations. Figures 25a - 25c reveal the presence of salt formation, aligning with literature suggesting that the catalytic surface may become obstructed, reducing the active surface area and the removal of gas [52, 53]. Based on scientific intuition, the ion accumulation is thought to be mitigated by lowering the ion concentration. The membrane is soaked in 6 M KOH, but the electrolyte reservoir can be at lower concentrations to further mitigate this ion accumulation. In practice, this method has not yet been applied, but electrolyte buildup should be mitigated in theory. More indications and images towards salt formation can be seen in Appendix I.

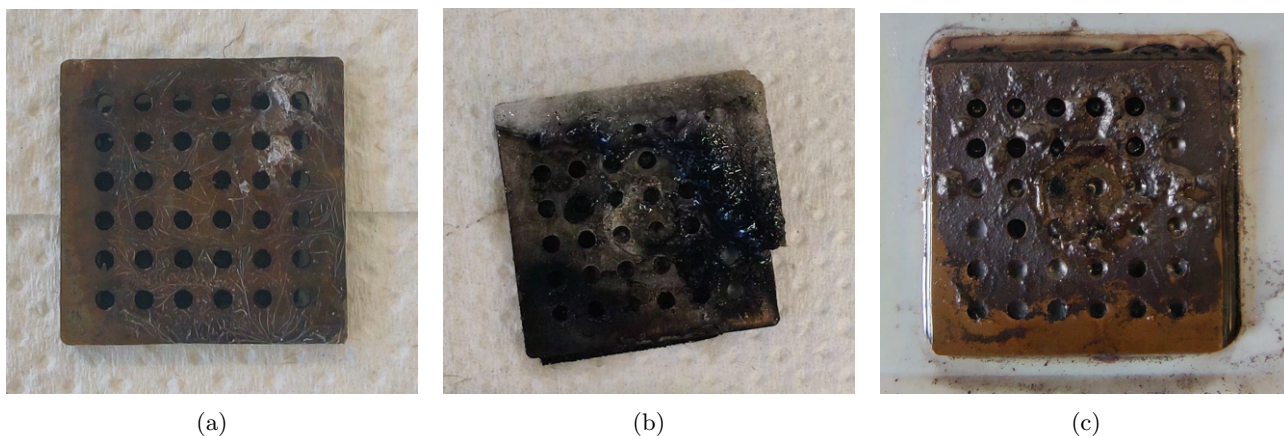


Figure 25: (a) Salt formation occurring after a 5-hour (constant current of 100 mA/cm<sup>2</sup>) measurement at room temperature at the backside of the cathode. (b) Salt formation occurring after a 15-hour (constant current of 50 mA/cm<sup>2</sup>) measurement at room temperature at the backside of the cathode. (c) Salt formation occurring after a 15-hour (constant current of 50 mA/cm<sup>2</sup> - 100 mA/cm<sup>2</sup>) measurement at 80 °C at the backside of the cathode.

### 3.7 Gas crossover

One compartment of the cell undergoes pressurisation by introducing nitrogen as a carrier gas into one of the gas outlets. This establishes a pressure gradient between the two compartments, wherein the measured compartment experiences higher pressure than the crossover side. In practical applications, the pressure in both compartments should ideally be equal to atmospheric pressure. Therefore, backpressure is implemented to achieve this equilibrium, as explained in the Experimental section. In this experiment, the focus is on measuring the O<sub>2</sub> side (H<sub>2</sub> crossover), since O<sub>2</sub> crossover is generally 4 times lower than H<sub>2</sub> due to the production rate (2 H<sub>2</sub>, 1 O<sub>2</sub>), excluding the difference in diffusion rate. The inference is that changing backpressure influences crossover values, as seen in Figure 26a. Figure 26b illustrates the gas crossover phenomenon under conditions of no backpressure and varying current densities. The nitrogen gas flow remains constant throughout the entire experiment (set at 8 mL/min). Notably, without any backpressure, the H<sub>2</sub> gas crossover is below the legal limit for up to 200 mA/cm<sup>2</sup>. For currents above 200 mA/cm<sup>2</sup>, the gas crossover increases significantly towards high values. The gas production increases while the induced pressure of the gas carrier remains constant. In order to refrain from measuring high gas crossovers, the carrier gas flow has to be increased, moving further away from standard applications (where pressure on both sides is equal). The pressure barrier created by flowing one gas chamber compartment with nitrogen is surpassed by increased gas production, which comes closer to standard applications (equal pressures). In Appendix J all injections of the different current densities can be found, where at 500 mA/cm<sup>2</sup>, equilibrium is reached at approximately 17% H<sub>2</sub> in O<sub>2</sub>. A trend line in this graph is added to discuss the resemblance of the data shown in the paper by Hodges et al. [6]. A similar trend is observed, where, depending on the amount of applied pressure, the absolute crossover values differ. To summarise this result, the induced pressure difference (due to the nitrogen carrier gas, which is kept constant) between both sides decreases with higher gas production, therefore gas crossover increases. In Appendix J, a supplementary measurement involving the application of carrier gas on both sides of the cell is presented, yielding consistent results with those obtained previously.

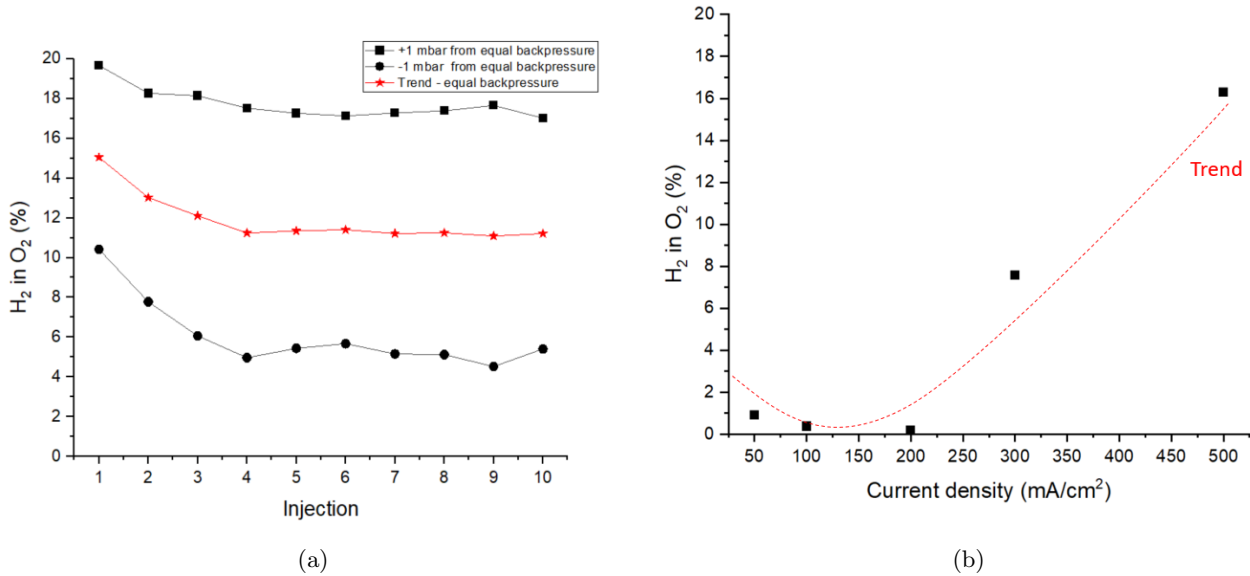


Figure 26: (a) H<sub>2</sub> gas crossover in O<sub>2</sub> at a constant current of 200 mA/cm<sup>2</sup>. A trend has been added to this graph since the exact backpressure is difficult to get the same as the applied pressure from the nitrogen gas. (b) Varying current densities with constant carrier gas flow (8 mL/min). A trendline is added to discuss the similarities to that found in literature [6].

## 4 Conclusion

We have successfully fabricated anodes coated with  $\text{Ni}_{0.8}\text{Fe}_{0.2}(\text{OH})_2$  and cathodes coated with Pt/C. Each electrode underwent individual testing via cyclic voltammetry (CV), revealing robust performance and high stability. Analysis of the individual experimental data facilitated an understanding of the underlying reactions occurring at each electrode. The anode, coated with  $\text{Ni}_{0.8}\text{Fe}_{0.2}(\text{OH})_2$ , oxidises to  $\text{Ni}_{0.8}\text{Fe}_{0.2}\text{OOH}$ , which is known to be an efficient OER catalyst. The observed oxidation peaks originate from several processes, including both the beta phase and the more present alpha phase of  $\text{Ni}_{0.8}\text{Fe}_{0.2}(\text{OH})_2$ , which contribute to the formation of their  $\alpha$ - and  $\beta$ -  $\text{Ni}_{0.8}\text{Fe}_{0.2}\text{OOH}$  phases. Additionally, at the parts that are not coated, the nickel substrate surface converts to  $\text{Ni}(\text{OH})_2$  in alkaline conditions. This oxidises to  $\text{NiOOH}$ , which happens slightly earlier than the aforementioned oxidation reactions. Corresponding reduction reactions are observed when scanning in the negative direction. The cathode, spray-coated with a Pt/C ink, demonstrates excellent catalytic behaviour towards HER at potentials near 0 V vs SHE. Hydrogen oxidation is evident, given the porous nature of the electrode; hence, gas bubbles can still be present when scanning in the positive direction. Subsequently, both electrodes are assembled into an alkaline electrolyser setup, immersing them in the electrolyte. Scanning between 0 V and 1.6 V enabled measuring the cell potential and the resultant generated current. The reference electrode was attached to the counter electrode (cathode), and the working electrode was the anode. This result revealed that the typical anode coating oxidation peaks were present and that the cell potential started to generate current (OER/HER) at approximately 1.48 V. Finally, the electrodes were assembled into the zero-gap cell design, where analytical techniques were used to determine the performance of different aspects of the design. The stability of the cell was tested by demanding a constant current for a maximum of 15 hours at different temperatures. This result revealed poor stability, where over time, the cell potential significantly and steadily increased, and fluctuations of more than 1 V were observed. Over time, salt forms, seen after disassembling the cell and is thought to be the reason for increased resistance. The large fluctuations in potential are thought to be caused by bubble formation, which blocks active catalytic surface area since, at higher temperatures, bubble formation is improved and shows fewer fluctuations. The cell potential was approximately 1.8 V at 80 °C and 300 mA/cm<sup>2</sup>, while that of reported literature was 1.47 V at 80 °C and 300 mA/cm<sup>2</sup> [6]. The faradaic efficiency of the cell was measured and resulted in values between 60-80% efficiency, depending on the applied current. A near 100% FE was not achieved; one reason for this is the fact that there are parasitic reactions caused by the current collectors, which are made from stainless steel and are not stable in alkaline media under certain potentials. Finally, the gas crossover measurements of this setup showed concerning results of H<sub>2</sub> crossover in O<sub>2</sub> above the legal limit of 2 mol%. The results showed that the amount of H<sub>2</sub> crossover can be manipulated by changing the pressure in the anode compartment (or by changing the production to pressure ratio). In standard applications, however, the setup is run at ambient pressure, which means that the crossover is imminent and needs to be mitigated before scaling up this process.

## 5 Outlook

It has become clear that the zero-gap cell does not perform as well as reported in Hodges et al. [6]. The individual electrodes seem to be working properly and are stable, as well as being assembled into an alkaline electrolysis setup. When assembling them into the zero-gap design, however, the lowest cell potential acquired was not coming close to the reported values, the gas crossover was above legal limits, and the FE was not close to 100%. The following recommendations are therefore in place:

- Changing the stainless steel current collectors to a material (either by coating or completely changing the material) to something more stable at high pH. The addition of this would theoretically lead to higher FE values. Assuming a hermetically sealed design would potentially give values close to 100% FE. Whether this holds true or not is yet to be reproduced from literature [6].
- The overall performance of the cell (stability and overpotential), at changing temperatures is poor compared to literature [6]. Arguably, optimisations need to be done, but the cause(s) of this poor performance is unclear and needs further investigation.
- The formation of salt, happening at the electrodes, gas chambers, and current collectors, would pose issues regarding gas removal, blocking of active surface area, and overall increased resistance. By lowering the electrolyte concentration, this could theoretically be mitigated, but it needs experimental evidence to show this does not have other effects on the performance of the cell.
- It is clear that gas crossover with the use of the PES membrane under ambient conditions is above legal limits. The proof of that has been displayed in this project; however, the mitigation of gas crossover with this capillary-fed setup is yet to be researched. For this reason, it is advised to look for methods that reduce the gas crossover on both sides of the cell.

## 6 Acknowledgement

I would like to express my heartfelt gratitude to the following individuals and groups who have been instrumental during my project:

First and foremost, I extend my sincerest thanks to my daily supervisor, Santosh Pal, whose guidance and lab support have been an important part in my project. I truly learned a lot from you in many aspects of the research field.

Secondly, I am deeply appreciative of my project supervisor, Fokko Mulder, for giving me this project. I would also like to thank you for your expert guidance and insightful meetings, which have been crucial to the success and development of my project.

In general, I also wish to acknowledge the MECS group for providing a collaborative and inspiring research environment that has enriched my academic experience, where the coffee breaks, drinks, and other social events were always pleasant and fun to be a part of. I am thankful to the students, PhD and PostDoc researchers within the MECS group, whose shared knowledge and insightful discussions and feedback have significantly contributed to my growth as a researcher.

I would also like to give thanks to the dedicated technicians Herman Schreuders and Joost Middelkoop who have provided essential technical support and expertise, facilitating the smooth execution of my experiments.

Lastly, I would like to thank my friends and family for their unlimited support, their understanding, and encouragement, for without their presence, this academic journey wouldn't have been as well-rounded.

## References

- [1] United Nations. *Carbon neutrality 2050*. URL: <https://www.un.org/sg/en/content/sg/articles/2020-12-11/carbon-neutrality-2050-the-world%E2%80%99s-most-urgent-mission>. (accessed: February 1, 2024).
- [2] Rajendra K Pachauri and Andy Reisinger. “Climate change 2007: Synthesis report. Contribution of working groups I, II and III to the fourth assessment report of the Intergovernmental Panel on Climate Change”. In: *Climate Change 2007. Working Groups I, II and III to the Fourth Assessment* (2007).
- [3] Siemens Energy. *The industrial world is still dependent on fossil fuels, here is how we decarbonize it anyway*. URL: <https://www.siemens-energy.com/global/en/news/magazine/2022/decarbonizing-hard-to-abate-industries.html>. (accessed: September 14, 2023).
- [4] IEA (2019). *The Future of Hydrogen*. URL: <https://www.iea.org/reports/the-future-of-hydrogen>. (accessed: September 14, 2023).
- [5] Benjamin Hmiel et al. “Preindustrial 14CH4 indicates greater anthropogenic fossil CH4 emissions”. In: *Nature* 578.7795 (2020), pp. 409–412.
- [6] Aaron Hodges et al. “A high-performance capillary-fed electrolysis cell promises more cost-competitive renewable hydrogen”. In: *Nature communications* 13.1 (2022), p. 1304.
- [7] Diogo MF Santos, César AC Sequeira, and José L Figueiredo. “Hydrogen production by alkaline water electrolysis”. In: *Química Nova* 36 (2013), pp. 1176–1193.
- [8] Mingyong Wang et al. “The intensification technologies to water electrolysis for hydrogen production—A review”. In: *Renewable and sustainable energy reviews* 29 (2014), pp. 573–588.
- [9] Gerda Gahleitner. “Hydrogen from renewable electricity: An international review of power-to-gas pilot plants for stationary applications”. In: *international Journal of hydrogen energy* 38.5 (2013), pp. 2039–2061.
- [10] C Carpetis. “Estimation of storage costs for large hydrogen storage facilities”. In: *International Journal of Hydrogen Energy* 7.2 (1982), pp. 191–203.
- [11] Jan Michalski et al. “Hydrogen generation by electrolysis and storage in salt caverns: Potentials, economics and systems aspects with regard to the German energy transition”. In: *International Journal of Hydrogen Energy* 42.19 (2017), pp. 13427–13443.
- [12] A Goncharov, A Guglya, and E Melnikova. “On the feasibility of developing hydrogen storages capable of adsorption hydrogen both in its molecular and atomic states”. In: *International journal of hydrogen energy* 37.23 (2012), pp. 18061–18073.
- [13] Jörn Brauns and Thomas Turek. “Alkaline water electrolysis powered by renewable energy: A review”. In: *Processes* 8.2 (2020), p. 248.
- [14] IREA IRENA. “Green hydrogen cost reduction: scaling up electrolyzers to meet the 1.5 C climate goal”. In: *Abu Dhabi: International Renewable Energy Agency* (2020).
- [15] Enapter. *What is the energy content of H<sub>2</sub>*. URL: [https://www.enapter.com/kb\\_post/what-is-the-energy-content-of-hydrogen](https://www.enapter.com/kb_post/what-is-the-energy-content-of-hydrogen). (accessed: February 1, 2024).
- [16] Ember. *Yearly electricity Data*. URL: <https://ember-climate.org/data-catalogue/yearly-electricity-data/>. (accessed: February 1, 2024).
- [17] Powermag. *Who has the worlds most efficient coal power plant fleet*. URL: <https://www.powermag.com/who-has-the-worlds-most-efficient-coal-power-plant-fleet/>. (accessed: February 1, 2024).
- [18] Hyper Textbook. *Energy density of coal*. URL: <https://hypertextbook.com/facts/2003/JuliyaFisher.shtml>. (accessed: February 1, 2024).
- [19] European Nuclear Society. *Coal Equivalent*. URL: <https://www.euronuclear.org/glossary/coal-equivalent/>. (accessed: February 1, 2024).
- [20] Yuhao Chu et al. “A new method for improving the ion conductivity of anion exchange membranes by using TiO<sub>2</sub> nanoparticles coated with ionic liquid”. In: *RSC advances* 6.99 (2016), pp. 96768–96777.
- [21] Wei You et al. “Highly conductive and chemically stable alkaline anion exchange membranes via ROMP of trans-cyclooctene derivatives”. In: *Proceedings of the National Academy of Sciences* 116.20 (2019), pp. 9729–9734.
- [22] Sun Young Kang et al. “High-performance and durable water electrolysis using a highly conductive and stable anion-exchange membrane”. In: *International Journal of Hydrogen Energy* 47.15 (2022), pp. 9115–9126.

- [23] Ali Keçebaş, Muhammet Kayfeci, and Mutlucan Bayat. “Electrochemical hydrogen generation”. In: *Solar Hydrogen Production*. Elsevier, 2019, pp. 299–317.
- [24] Vincenzo Liso and Samuel Simon Araya. “Chapter 6 - Thermodynamics and operating conditions for proton exchange membrane fuel cells”. In: *PEM Fuel Cells*. Ed. by Gurbinder Kaur. Elsevier, 2022, pp. 123–136.
- [25] Min Li, Hemiao Yu, and Hongpu Du. In: *Open Physics* 18.1 (2020), pp. 906–915. DOI: doi:10.1515/phys-2020-0203. URL: <https://doi.org/10.1515/phys-2020-0203>.
- [26] Haojun Xie et al. “Coupling of two-phase flow in fractured-vuggy reservoir with filling medium”. In: *Open Physics* 15.1 (2017), pp. 12–17.
- [27] Yueying Wang et al. “Simulation of counter-current imbibition in water-wet fractured reservoirs based on discrete-fracture model”. In: *Open Physics* 15.1 (2017), pp. 536–543.
- [28] CJ Kuijpers et al. “Quantitative measurements of capillary absorption in thin porous media by the Automatic Scanning Absorptometer”. In: *Chemical Engineering Science* 178 (2018), pp. 70–81.
- [29] Frank Allebrod et al. “Electrical conductivity measurements of aqueous and immobilized potassium hydroxide”. In: *International Journal of Hydrogen Energy* 37.21 (2012), pp. 16505–16514.
- [30] Mark Sassenburg et al. “Zero-gap electrochemical CO<sub>2</sub> reduction cells: challenges and operational strategies for prevention of salt precipitation”. In: *ACS Energy Letters* 8.1 (2022), pp. 321–331.
- [31] Volkmar Schröder and Kai Holtappels. “Explosion characteristics of hydrogen-air and hydrogen-oxygen mixtures at elevated pressures”. In: (2005).
- [32] Philipp Haug, Matthias Koj, and Thomas Turek. “Influence of process conditions on gas purity in alkaline water electrolysis”. In: *International Journal of Hydrogen Energy* 42.15 (2017), pp. 9406–9418.
- [33] JT Kraakman. “Gas Crossover in Alkaline Water Electrolysis”. In: (2023).
- [34] PTHM Verhallen et al. “The diffusion coefficients of helium, hydrogen, oxygen and nitrogen in water determined from the permeability of a stagnant liquid layer in the quasi-s”. In: *Chemical Engineering Science* 39.11 (1984), pp. 1535–1541.
- [35] RC Roberts. “Molecular diffusion of gases”. In: *American Institute of Physics Handbook* 235 (1963).
- [36] Zengcai Liu et al. “The effect of membrane on an alkaline water electrolyzer”. In: *International Journal of Hydrogen Energy* 42.50 (2017), pp. 29661–29665.
- [37] Jörn Brauns et al. “Evaluation of diaphragms and membranes as separators for alkaline water electrolysis”. In: *Journal of The Electrochemical Society* 168.1 (2021), p. 014510.
- [38] Kenta Kawashima et al. “Accurate Potentials of Hg/HgO Electrodes: Practical Parameters for Reporting Alkaline Water Electrolysis Overpotentials”. In: *ACS Catalysis* 13.3 (2023), pp. 1893–1898.
- [39] A Iranzo and FM Mulder. “Nickel-iron layered double hydroxides for an improved Ni/Fe hybrid battery-electrolyser”. In: *Materials Advances* 2.15 (2021), pp. 5076–5088.
- [40] SB Lyon. “Corrosion of noble metals”. In: *Shreir’s Corrosion* 3 (2010), pp. 2205–2223.
- [41] CM Zalitis et al. “Properties of the hydrogen oxidation reaction on Pt/C catalysts at optimised high mass transport conditions and its relevance to the anode reaction in PEFCs and cathode reactions in electrolyzers”. In: *Electrochimica Acta* 176 (2015), pp. 763–776.
- [42] W Visscher and E Barendrecht. “Investigation of thin-film  $\alpha$ - and  $\beta$ -Ni(OH)<sub>2</sub> electrodes in alkaline solutions”. In: *Journal of electroanalytical chemistry and interfacial electrochemistry* 154.1-2 (1983), pp. 69–80.
- [43] Ding Yunchang, Yuan Jiongliang, and Chang Zhaorong. “Cyclic voltammetry response of coprecipitated Ni(OH)<sub>2</sub> electrode in 5 M KOH solution”. In: *Journal of power sources* 69.1-2 (1997), pp. 47–54.
- [44] AMP Sakita et al. “Novel NiFe/NiFe-LDH composites as competitive catalysts for clean energy purposes”. In: *Applied Surface Science* 447 (2018), pp. 107–116.
- [45] Prabjit Singh et al. “A case study of nickel dendritic growth on printed-circuit boards”. In: *2020 Pan Pacific Microelectronics Symposium (Pan Pacific)*. IEEE, 2020, pp. 1–8.
- [46] Pengcheng Zhao et al. “Alkaline zero gap bipolar water electrolyzer for hydrogen production with independent fluid path”. In: *Energy Reports* 9 (2023), pp. 352–360.
- [47] Mitja Mori et al. “Integral characteristics of hydrogen production in alkaline electrolyzers”. In: *Strojniški vestnik-Journal of Mechanical Engineering* 59.10 (2013), pp. 585–594.

- [48] Marcelo Carmo and Detlef Stolten. “Energy storage using hydrogen produced from excess renewable electricity: Power to hydrogen”. In: *Science and Engineering of Hydrogen-Based Energy Technologies*. Elsevier, 2019, pp. 165–199.
- [49] Weizhe Zhang et al. “Water electrolysis toward elevated temperature: advances, challenges and frontiers”. In: *Chemical Reviews* (2023).
- [50] Pekka Pohjanne et al. “Effect of Electrochemical Potential on Stress Corrosion Cracking Susceptibility of EN 1.4301 (AISI 304) Austenitic Stainless Steels in Simulated Hot Black Liquor”. In: *Corrosion* 71.7 (2015), pp. 887–894.
- [51] Metallos. *Pourbaix diagram of Fe*. URL: <https://commons.wikimedia.org/wiki/File:Fe-pourbaix-diagram.svg>. (accessed: January 20, 2024).
- [52] Sahil Garg et al. “How alkali cations affect salt precipitation and CO<sub>2</sub> electrolysis performance in membrane electrode assembly electrolyzers”. In: *Energy & Environmental Science* 16.4 (2023), pp. 1631–1643.
- [53] JW Haverkort and H Rajaei. “Voltage losses in zero-gap alkaline water electrolysis”. In: *Journal of Power Sources* 497 (2021), p. 229864.
- [54] Qihua Liang, Geert Brocks, and Anja Bieberle-Hütter. “Oxygen evolution reaction (OER) mechanism under alkaline and acidic conditions”. In: *Journal of Physics: Energy* 3.2 (2021), p. 026001.
- [55] Nasir Mahmood et al. “Electrocatalysts for hydrogen evolution in alkaline electrolytes: mechanisms, challenges, and prospective solutions”. In: *Advanced science* 5.2 (2018), p. 1700464.

## Part II

# Appendix

## Table of Contents

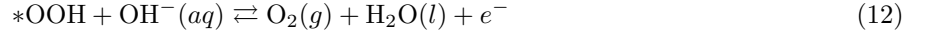
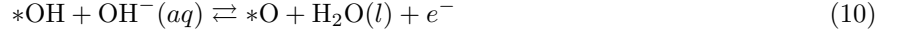
---

|          |   |           |
|----------|---|-----------|
| <b>A</b> | <b>Half reactions</b>                           | <b>39</b> |
| <b>B</b> | <b>Anode experiments</b>                        | <b>40</b> |
| B.1      | Stability Stainless Steel . . . . .             | 40        |
| <b>C</b> | <b>X-ray powder diffraction</b>                 | <b>42</b> |
| C.1      | XRD results . . . . .                           | 42        |
| <b>D</b> | <b>Anode SEM Images</b>                         | <b>43</b> |
| D.1      | Ni-Coatings (No iron) . . . . .                 | 43        |
| D.2      | PTFE implemented in the Ni/Fe coating . . . . . | 44        |
| <b>E</b> | <b>Membrane SEM Images</b>                      | <b>46</b> |
| E.1      | Dry and wet . . . . .                           | 46        |
| E.2      | Lower currents . . . . .                        | 47        |
| E.3      | Higher currents . . . . .                       | 48        |
| E.4      | Cleaned membrane: higher currents . . . . .     | 49        |
| <b>F</b> | <b>Visual information</b>                       | <b>50</b> |
| F.1      | Anode coatings . . . . .                        | 50        |
| F.2      | Coating area . . . . .                          | 51        |
| <b>G</b> | <b>EDX area measurement</b>                     | <b>52</b> |
| <b>H</b> | <b>Faradaic efficiency</b>                      | <b>54</b> |
| H.1      | GC calculation . . . . .                        | 54        |
| H.2      | Faradaic efficiencies . . . . .                 | 54        |
| <b>I</b> | <b>Salt formation</b>                           | <b>56</b> |
| <b>J</b> | <b>Gas Crossover</b>                            | <b>57</b> |

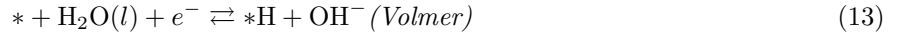
---

## A Half reactions

The total reaction is a simplification of the half reactions; in turn, the half reactions are also simplified. In reality,  $\text{OH}^-$  and  $\text{H}_2\text{O}$  have to bind to the surface of the catalysts, forming intermediates before producing the desired gases. The reaction mechanism for OER in an alkaline medium is encapsulated in (Eq. 9-12)[54].



The reaction mechanism for HER in an alkaline medium is expressed in (Eq. 13-15)[55].



## B Anode experiments

Throughout the anode preparation, multiple techniques were implemented for training and testing purposes. Different mixture compositions, coating methods or drying and/or aging methods were tested. In this section, the used techniques are explained. The electrodes were placed in an electrocoating solution that comprised of various mixture compositions:

- 0.2 M  $\text{Ni}(\text{NO}_3)_2 \cdot 6\text{H}_2\text{O}$  for only  $\text{Ni}(\text{OH})_2$  plating.
- 0.2 M  $\text{NiCl}_2 \cdot 6\text{H}_2\text{O}$  for only  $\text{Ni}(\text{OH})_2$  plating.
- 1:1 mixture of  $\text{NiCl}_2 \cdot 6\text{H}_2\text{O}$  (0.2 M) and  $\text{FeCl}_3$  (0.2 M), where  $\text{FeCl}_3$  was added after bubbling the solution with Ar for 20 minutes.
- 1 M KCl supporting electrolyte, along with a 3:1 mixture of  $\text{NiCl}_2 \cdot 6\text{H}_2\text{O}$  (0.075 M) and  $\text{FeCl}_3$  (0.025 M), where after bubbling the solution with Ar for 20 minutes,  $\text{FeCl}_3$  was added.
- 1:1 mixture of  $\text{Ni}(\text{NO}_3)_2 \cdot 6\text{H}_2\text{O}$  (0.15 M) and  $\text{FeSO}_4$  (0.15 M), where  $\text{FeSO}_4$  was added after bubbling the solution with Ar for 20 minutes.
- 70/30% mixture of  $\text{Ni}(\text{NO}_3)_2 \cdot 6\text{H}_2\text{O}$  (0.21 M) and  $\text{FeSO}_4$  (0.09 M), where  $\text{FeSO}_4$  was added after bubbling the solution with Ar for 20 minutes.

The immersed Ni mesh was coated with  $\text{NiFeOOH}$  by:

- Cycling between -1.3 V and -0.5 V (vs Ag/AgCl) at 10 mV/s until a charge of 2-3 C has been deposited for  $\text{NiCl}_2 \cdot 6\text{H}_2\text{O}$  solutions, and cycling between -0.9 V and -0.2 V (vs Ag/AgCl) for  $\text{Ni}(\text{NO}_3)_2 \cdot 6\text{H}_2\text{O}$  solutions.
- Applying constant current, where the maximum applied current did not exceed a corresponding applied potential of -0.9 V for  $\text{Ni}(\text{NO}_3)_2 \cdot 6\text{H}_2\text{O}$  solutions, and -1.3 V for  $\text{NiCl}_2 \cdot 6\text{H}_2\text{O}$ .
- applying pulse potentials of -1 V for 1 second, with a 1 second rest for  $\text{Ni}(\text{NO}_3)_2 \cdot 6\text{H}_2\text{O}$  and  $\text{Fe}(\text{SO}_4)$  solutions.
- Corrosion assisted synthesis, stirring the substrate in a 0.5 M  $\text{NiCl}_2 \cdot 6\text{H}_2\text{O}$ ,  $\text{FeCl}_3$  (70/30%) solution for 5 minutes.

After coating, the Ni mesh was rinsed with deionised water and went through drying or aging in one of the following manners:

- Put in a vacuum oven and dried at 50°C for 1 hour.
- Dried at room temperature for 1 hour.
- Aged in KOH for 1 hour for complete activation of the surface area.

### B.1 Stability Stainless Steel

The surface area of an even finer mesh made from stainless steel is larger than the Ni mesh reported in Hodges et al. [6]. This results in a less thick coating by applying the same method reported in the Result section, and with this, the performance is very poor.

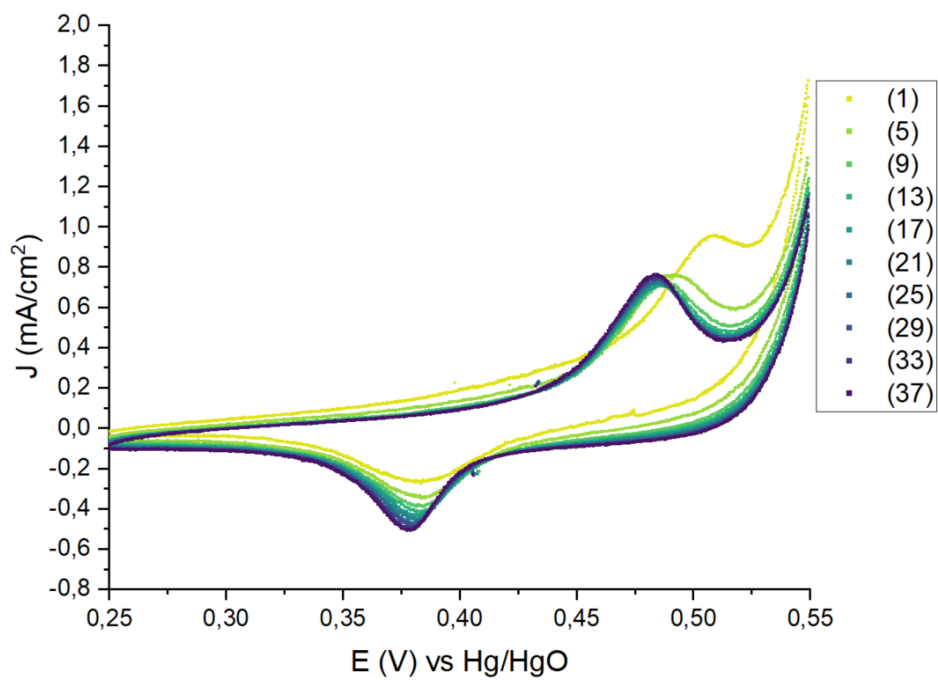


Figure B.1: 80/20 coating  $\text{Ni}(\text{NO}_3)_3 \cdot 6 \text{H}_2\text{O}$  (0.24 M) and  $\text{Fe}(\text{SO}_4)_7 \cdot 7 \text{H}_2\text{O}$  (0.06 M) together with PTFE (10 g/L) on a stainless steel mesh, cycling between 0.25 V-0.55 V (vs Hg/HgO), scanrate = 10 mV/s, cycles 1, 5, 9, 13, 17, 21, 25, 29, 33 and 37 are shown.

## C X-ray powder diffraction

X-ray powder diffraction (XRD) is used as phase identification of a crystalline material and provides information on lattice structures and parameters. Bragg's Law, as shown in (Eq. 16), is used to calculate the distance between planes passing through atoms identically. For cubic lattice structures, the lattice parameters ( $a=b=c$ ) are calculated using (Eq. 17).

$$n\lambda = 2d \sin \theta \quad (16)$$

$$\frac{1}{d^2} = \frac{(h^2 + k^2 + l^2)}{a^2} \quad (17)$$

### C.1 XRD results

By beaming electrons on a copper substrate,  $\alpha$ -K and  $\beta$ -K x-rays are released and beamed onto the sample, where material specific  $\theta$  angles are compared with reference databases. With this, the lattice parameters can be calculated as explained in section 2. Using this analytical method, the peaks for Ni are identified, as seen in figure C.1. Any additional peaks are absent in these measurements due to the higher abundance of nickel in comparison to substances like  $\text{Ni}(\text{OH})_2$ . When measuring  $\theta$  values below the onset of nickel's first appearance, it does not establish the discernible presence of  $\text{Ni}(\text{OH})_2$  or other materials due to the lack of signal. It is thought that this challenge mainly arises from the difficulty of maintaining the mesh in a flat configuration. Furthermore, the coating is relatively thin ( $1.2 \mu\text{m}$ ) compared to the substrate thickness ( $40 \mu\text{m}$ ), so more signal can come from the Ni substrate. Moreover, the diamond-shaped holes in the mesh contribute to a substantial surface area, reducing the surface area of the coating that the XRD measurement measures.

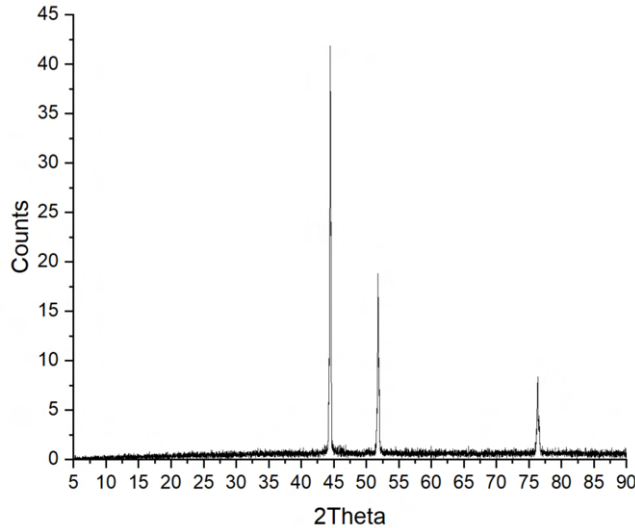


Figure C.1: Graph of the XRD measurement showing the peaks for nickel, overshadowing any presence of other substances.

## D Anode SEM Images

Throughout the thesis, multiple samples were imaged using the JMS-IT700. Below, the samples taken can be seen.

### D.1 Ni-Coatings (No iron)

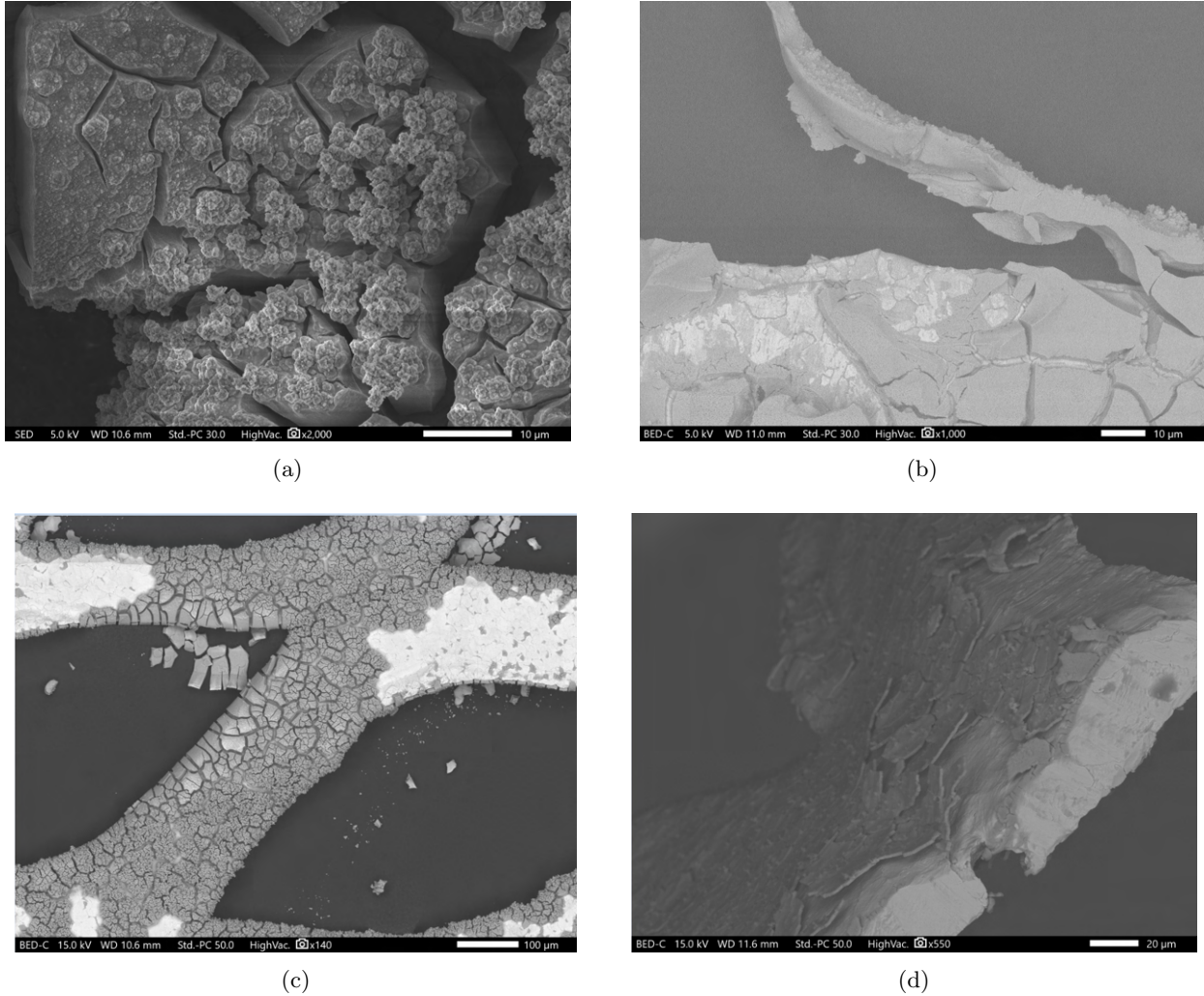


Figure D.1: (a) Image showing the surface structure of the Ni-coating (no Fe). The method used for applying this coating is constant current as discussed in Appendix B. (b) Image showing the thickness of the coating; the same sample is used as in the previous subfigure. Coating has a thickness of approximately 10–15 microns. (c) overhead view illustrating that the coating is covering the whole surface due to handling or bending the material. (d) Sideview image of a sample using the pulse applied potential method, showing thickness of approximately 1 micron.

In the images displayed above, the thickness of the coating differs because of the different duration and method of applying the coating to the substrate. Where the constant current method typically applied approximately 10–15 C, the pulse applied potential method applied roughly only 2 C. As seen in the Result section, the flakes on these coatings are also spike-like, so implementing or excluding iron does not influence the structure and shape of the flakes.

## D.2 PTFE implemented in the Ni/Fe coating

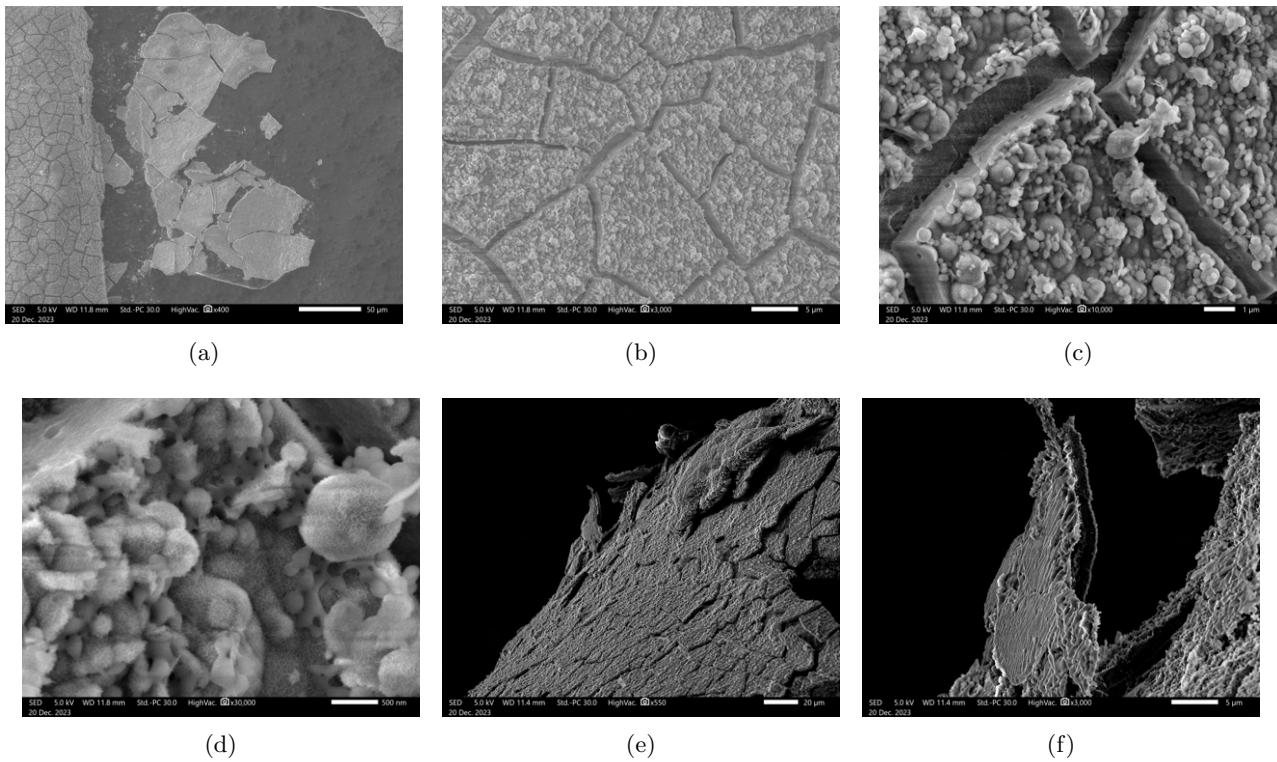
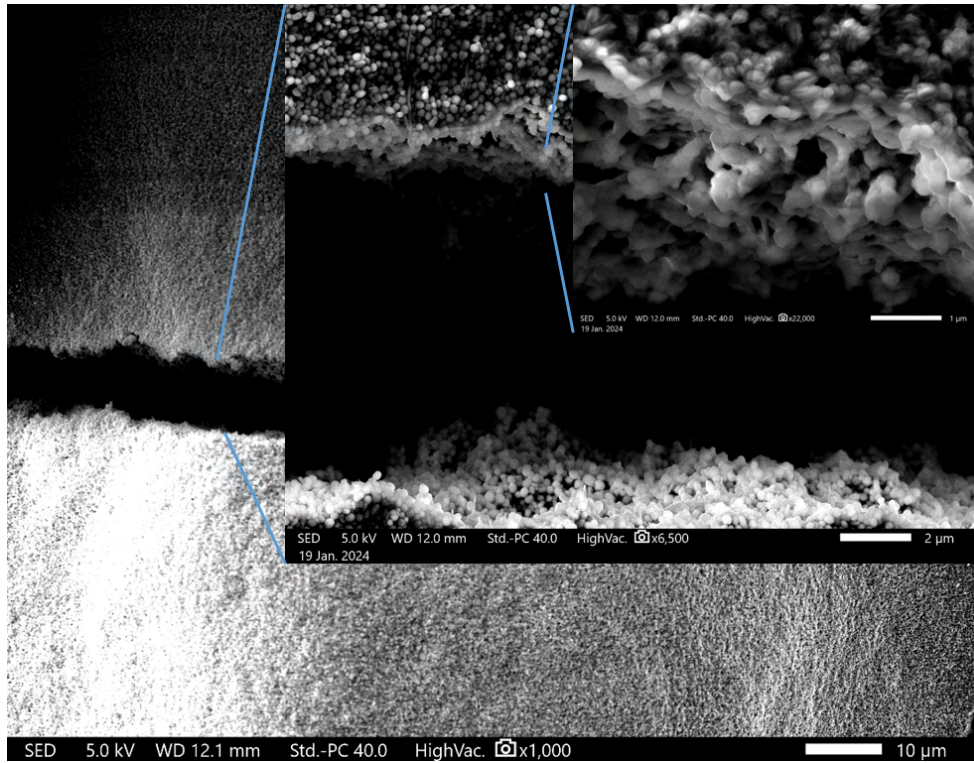
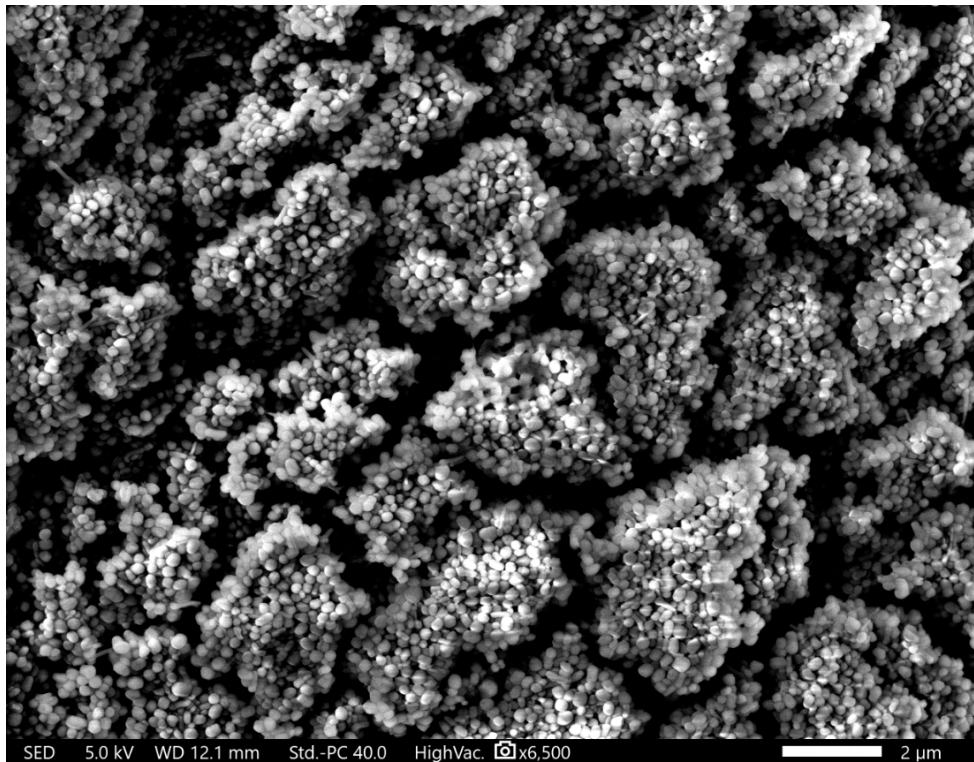


Figure D.2: (a) Image showing the backside of a piece of coating. (b) 3000x zoomed-in image of the surface of the coating, showing boundaries and some detail about the surface roughness. (c) 10000x zoomed-in image of the surface of the coating showing boundaries and the surface roughness in greater detail. (d) 30000x zoomed-in image of the surface of the coating, showing great detail about the surface roughness and structure. (e) Image taken of a place where the substrate is bended so the coating can be peeled off. (f) A more zoomed-in image of the same area as previous subfigure, showing the thickness of the coating is relatively equal and close to 1 micron.

Compared to the previous subsection in this appendix, the flakes have a bit of a different shape when implementing PTFE in the coating. The flakes are a bit more soft-like instead of spike-like, as without the implementation of PTFE. The PTFE itself is also put in the SEM. The images can be seen in Figure D.3a and D.3b where it becomes clear that PTFE follows a blob-like structure.



(a)



(b)

Figure D.3: (a) Three-phase image of the PTFE, one after the other, more zoomed-in. (b) A different chosen area where blob-like structures are seen.

## E Membrane SEM Images

During the testing phases of the cell, the PES membrane was cut into pieces and refreshed after a cell performance test. The membranes were treated during testing differently, resulting in a visible difference after testing. The difference is explained in further detail below, along with the illustrations of the SEM images.

### E.1 Dry and wet

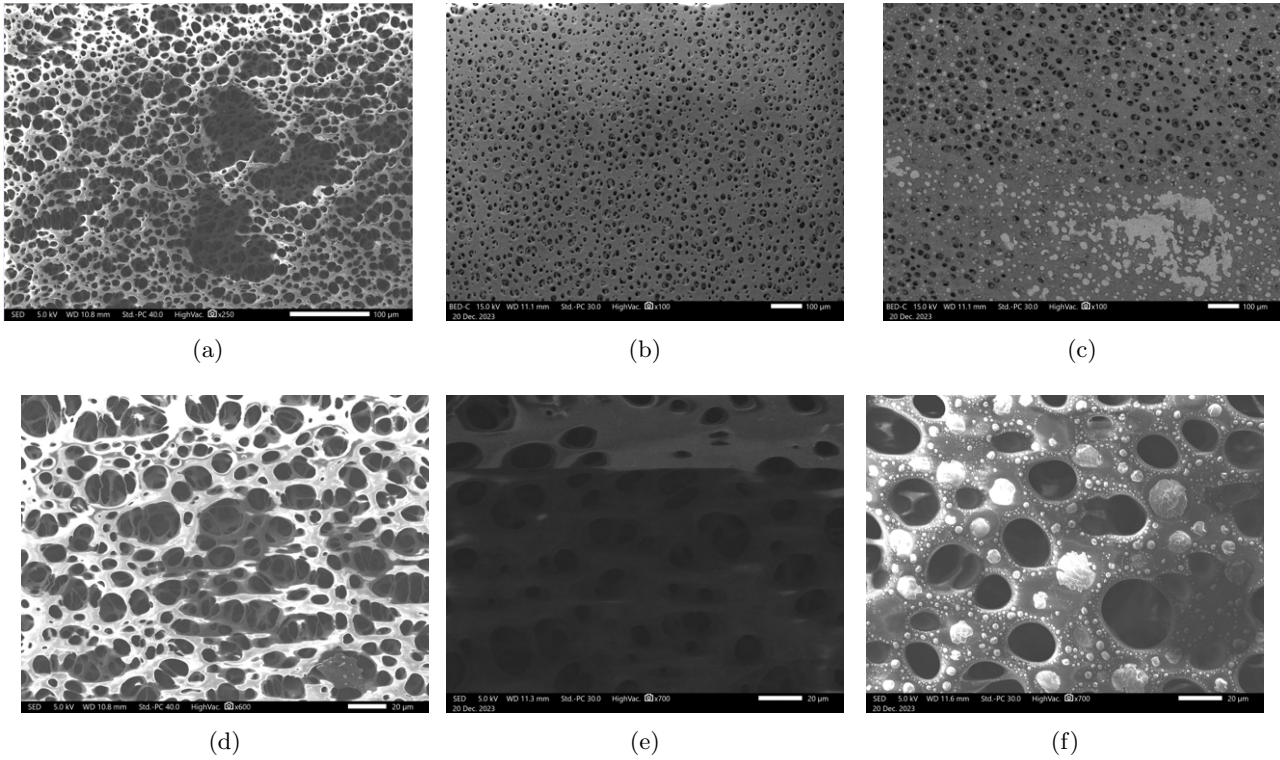
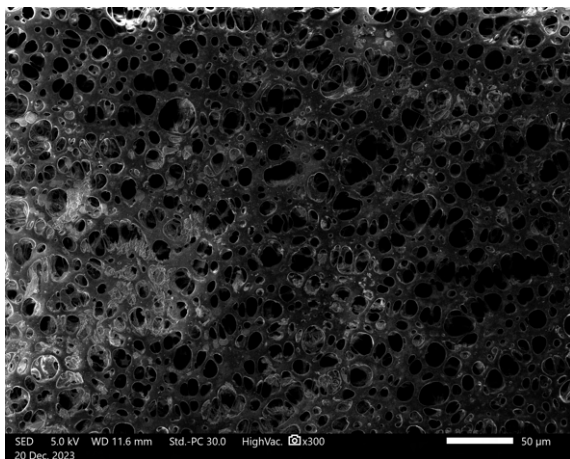


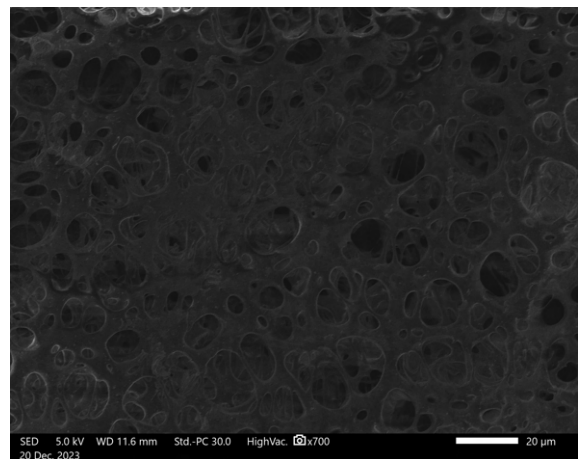
Figure E.1: (a) Coupled with (d): Completely dry membrane, not used for cell testing. (b) Coupled with (e): Membrane wetted with dionised water, not used for cell testing. (c) Coupled with (f): Membrane sample put in KOH and dried in vacuum, not used for cell testing. Salt crystals formed on the surface of the membrane.

Dry and wetted with dionised water do not show any difference in the PES separator. The color contrast is simply because of settings, not because of a physical difference between the two samples. A very clear difference can be seen in the KOH wetted sample, however. After drying, salt crystals form on the surface of the PES separator.

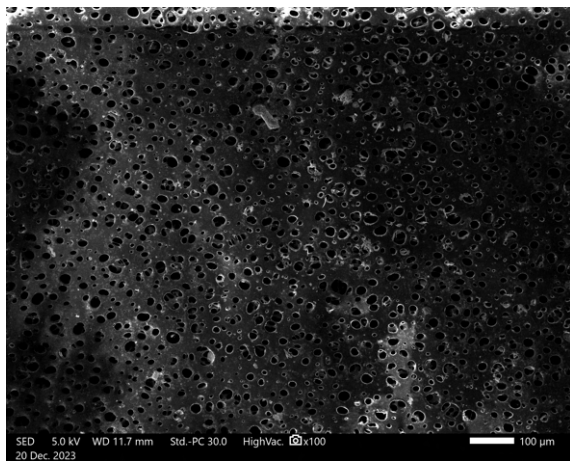
## E.2 Lower currents



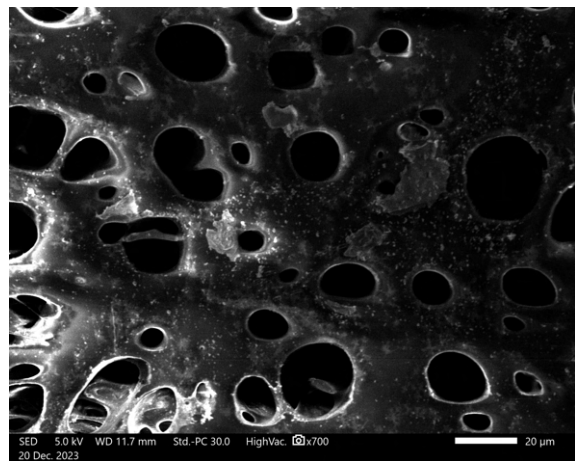
(a)



(b)



(c)

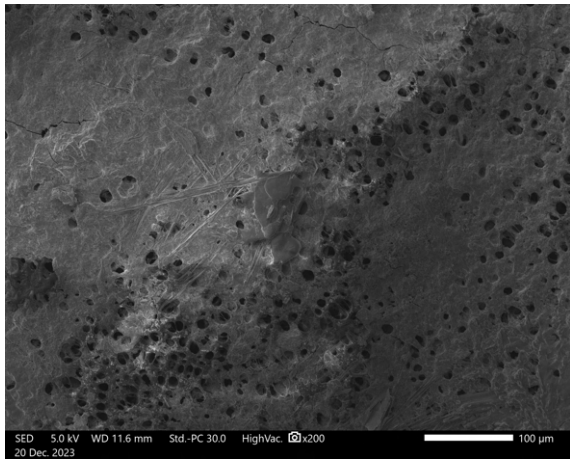


(d)

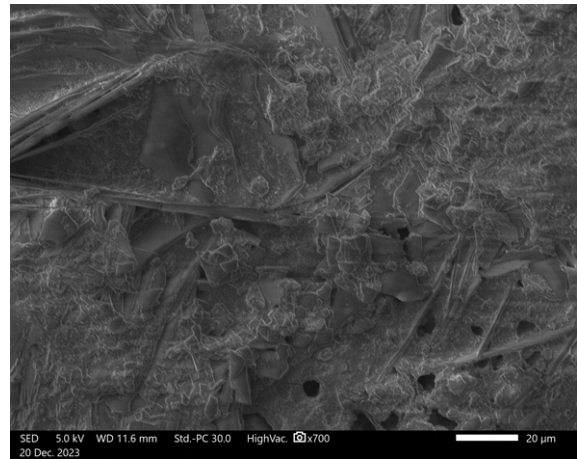
Figure E.2: (a) Coupled with (b): The side of the membrane touching the anode during testing, using a current of 100 mA. (c) Coupled with (d): The side of the membrane touching the cathode during testing, using a current of 100 mA.

No significant difference can be seen in the SEM imaging by applying 100 mA on the electrodes. There are, however, points that indicate a difference with the blank sample (dry or wetted with dionised water), which is salt formation on the membranes.

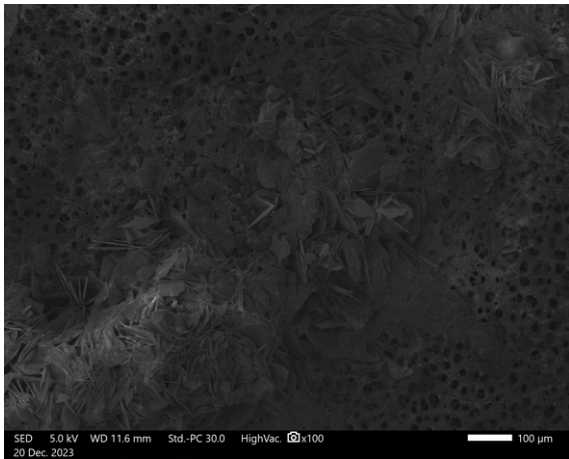
### E.3 Higher currents



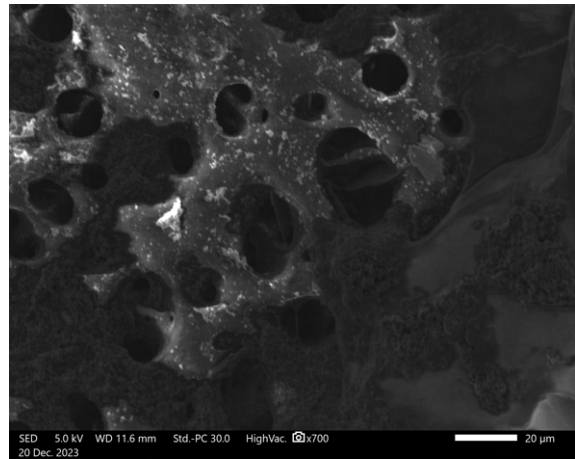
(a)



(b)



(c)



(d)

Figure E.3: (a) Coupled with (b): The side of the membrane touching the anode during testing, using a current of 300 mA. (c) Coupled with (d): The side of the membrane touching the cathode during testing, using a current of 300 mA.

Compared to the lower applied currents, a lot more salt formation can be seen in these images. A lot of pores are being blocked by the salt.

#### E.4 Cleaned membrane: higher currents

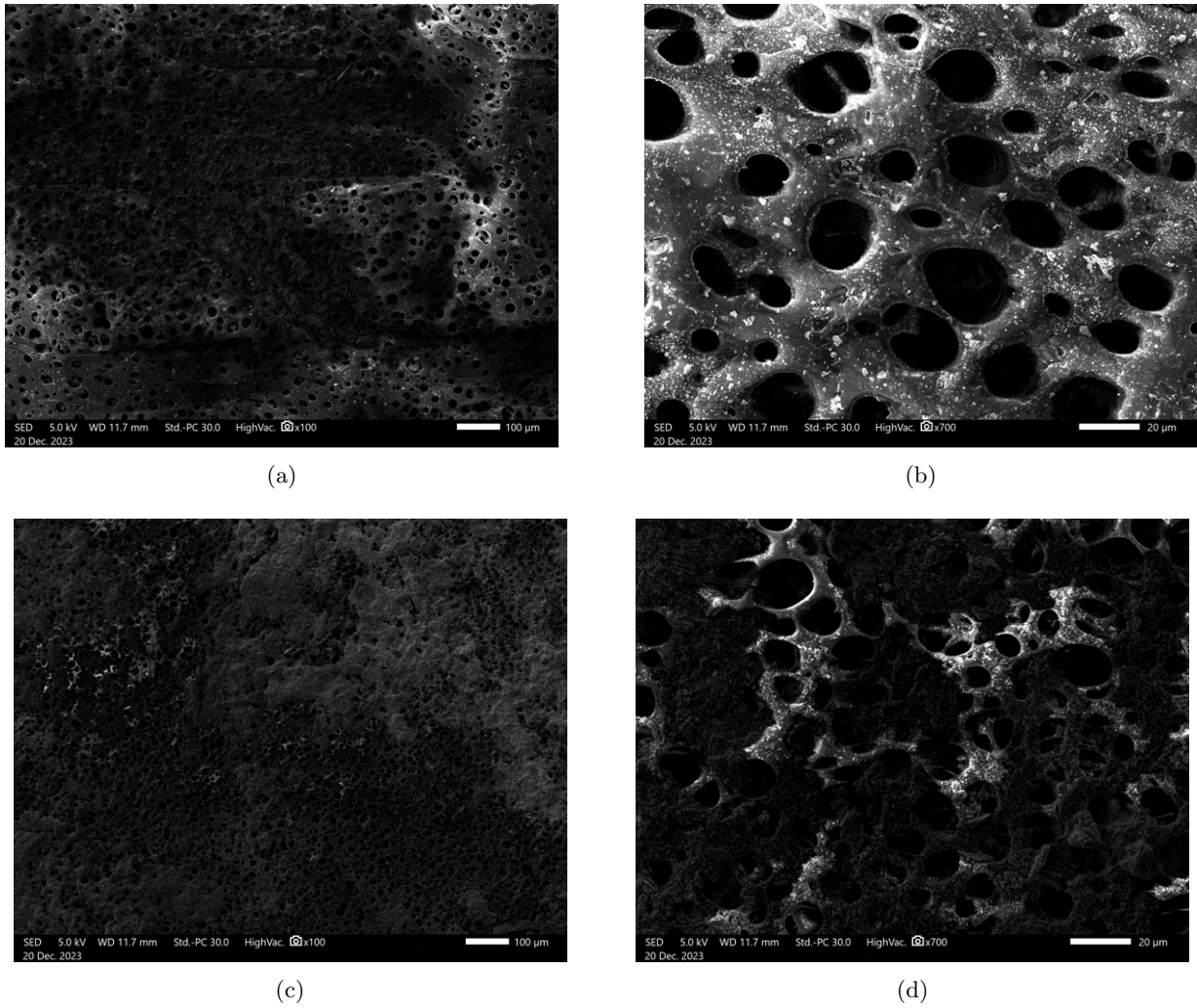


Figure E.4: (a) Coupled with (b): The side of the membrane touching the anode during testing, using a current of 300 mA, cleaned with deionised water. (c) Coupled with (d): The side of the membrane touching the cathode during testing, using a current of 300 mA, cleaned with deionised water.

From these images, it can be concluded that a lot of the salt formation can be removed by rinsing the membrane with water. Some of the blocked pores seem difficult to unblock, however. This might be caused by a local high current damaging the surface of the membrane.

## F Visual information

Throughout measurements, multiple photos are taken for visual representation.

### F.1 Anode coatings

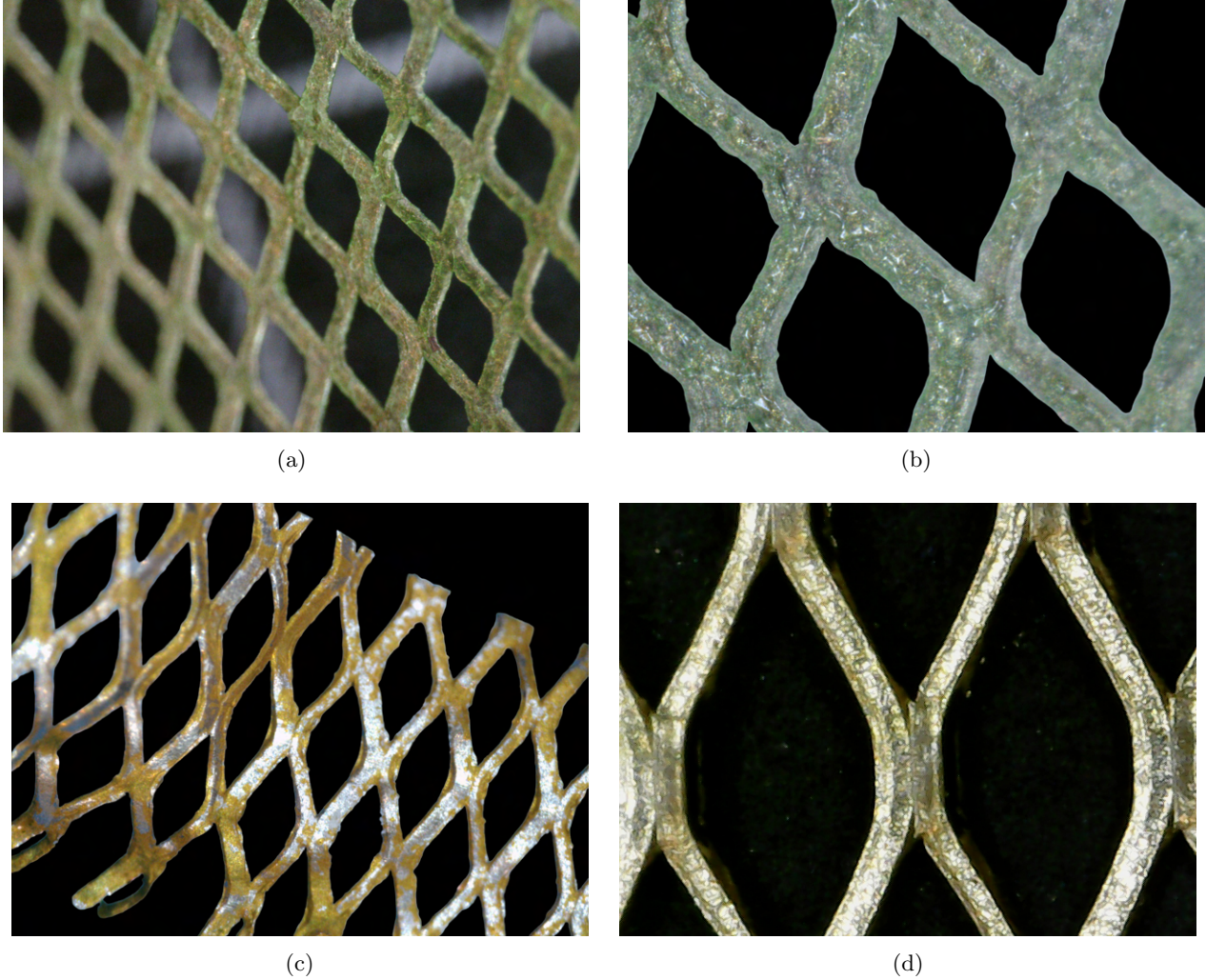


Figure F.1: (a) Coupled with (b):  $\text{Ni(OH)}_2$  coating on the nickel mesh. The coating shows a green color. (c) Coupled with (d):  $\text{NiFe(OH)}_2$  coating on the nickel mesh. The coating shows a golden color.

The images above illustrate the difference in color with two different coatings. Both cases show some spots with bare nickel, concluding that the coating peels off easily.

## F.2 Coating area

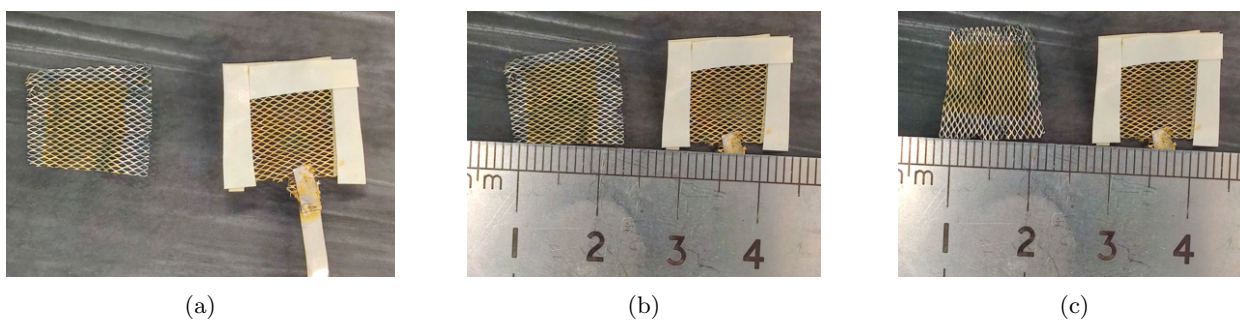


Figure F.2: (a) Image of the coated material before welding. The left side is the electrode after removing the electrocoated tape. The right side is the electrode before removing the tape and the extended part that connects with the parstat. (b) same electrodes, together with a ruler to show that the electrocoated part is 1 cm. (c) Indicates that the other side of the electrode is also 1 cm.

The images above conclude that the area which is coated is  $1 \text{ cm}^2$ . The gray part of the electrode is bare nickel mesh, which is welded on the stainless steel perforated plates for good contact.

## G EDX area measurement

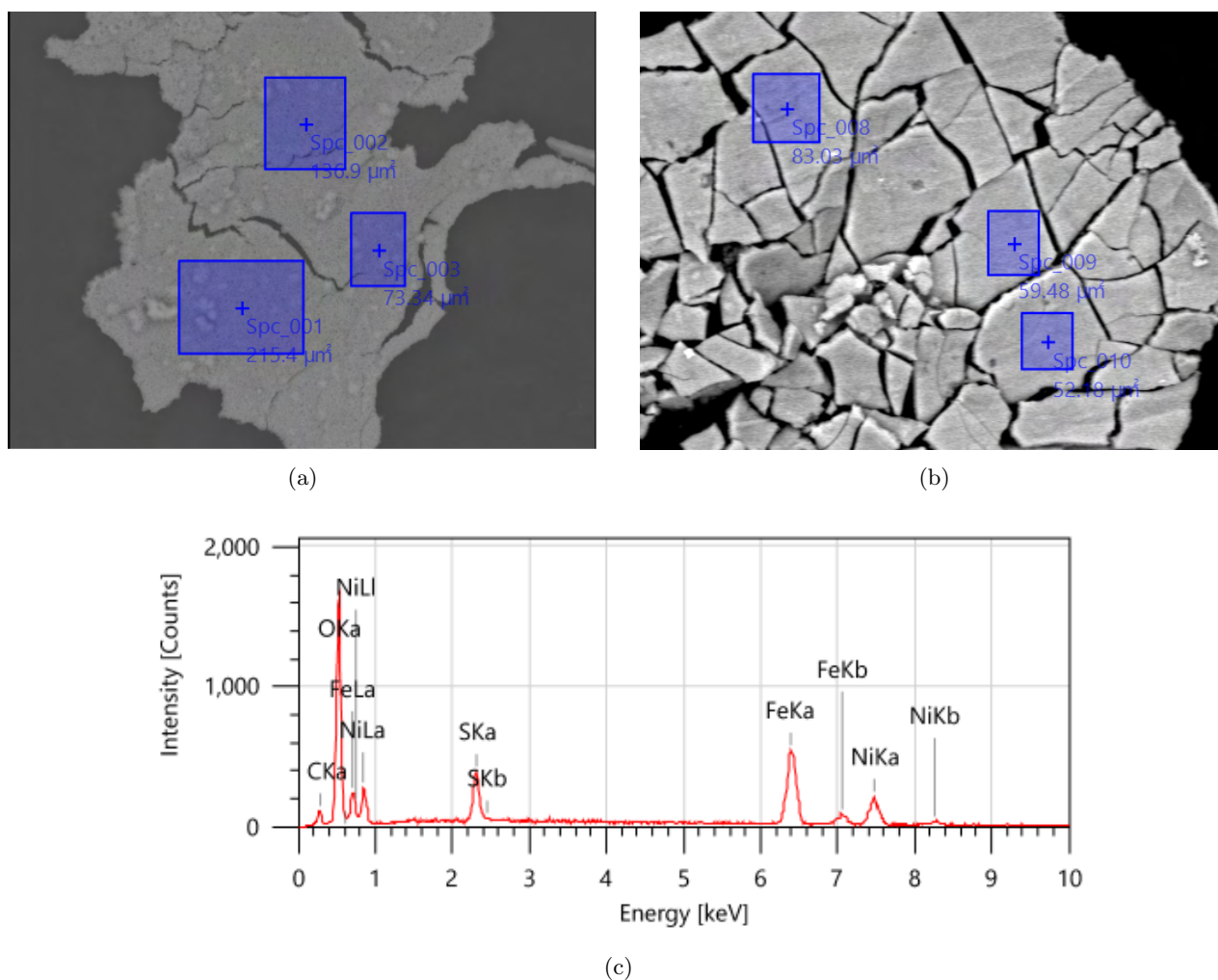


Figure G.1: (a)-(b) Images of the areas where the EDX measurements are done. The surface is scraped to ensure the coating is not in contact with the substrate. Sample is prepared via pulse applied potential for 300 pulses, using 50/50  $\text{Ni}(\text{NO}_3)_2 \cdot 6\text{H}_2\text{O}$  (0.15 M),  $\text{FeSO}_4 \cdot 7\text{H}_2\text{O}$  (0.15 M). (c) An example of the peaks of the different elements measured on one of the areas measured.

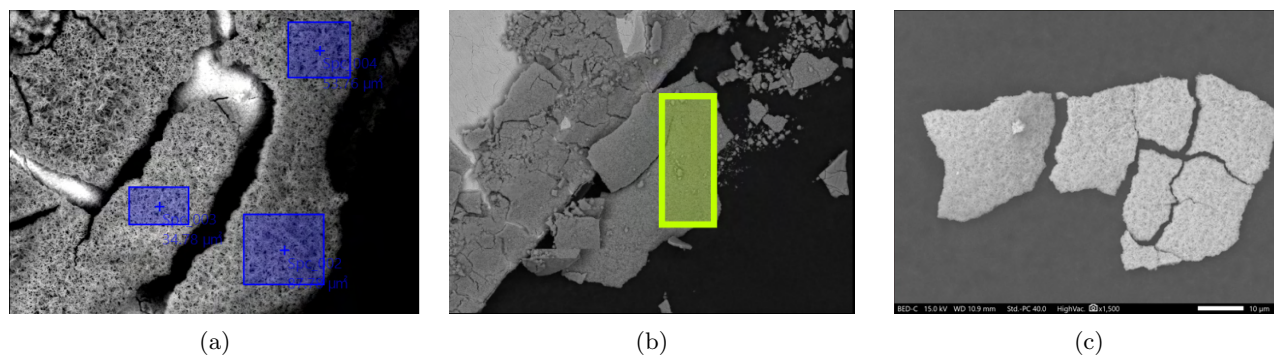


Figure G.2: (a)-(c) Images of the areas where the EDX measurements are done. The surface is scraped to ensure the coating is not in contact with the substrate. The sample is prepared via pulse applied potential for 300 pulses using 80/20  $\text{Ni}(\text{NO}_3)_2 \cdot 6\text{H}_2\text{O}$  (0.24 M) and  $\text{FeSO}_4 \cdot 7\text{H}_2\text{O}$  (0.06 M).

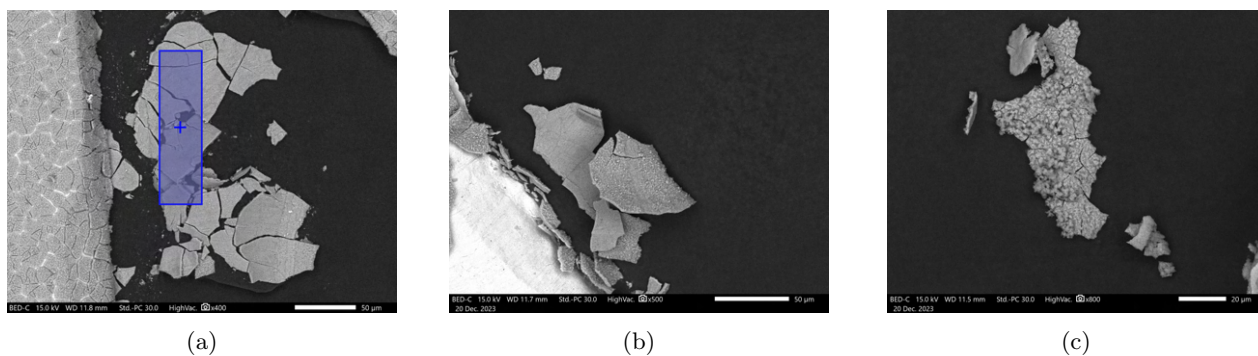


Figure G.3: (a)-(c) Images of the areas where the EDX measurements are done. The surface is scraped to ensure the coating is not in contact with the substrate. The sample is prepared via pulse applied potential for 300 pulses using 80/20  $\text{Ni}(\text{NO}_3)_2 \cdot 6 \text{H}_2\text{O}$  (0.24 M),  $\text{FeSO}_4 \cdot 7 \text{H}_2\text{O}$  (0.06 M) and PTFE (10g/L).

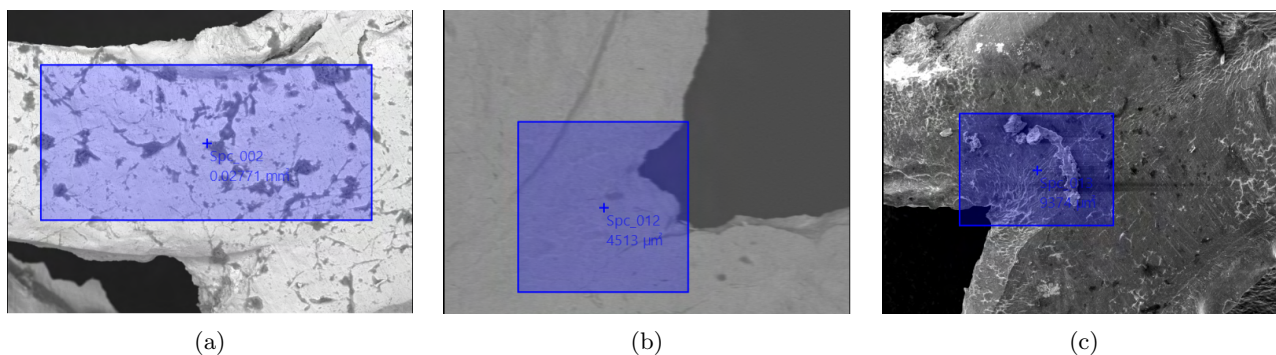


Figure G.4: (a)-(c) Images of the areas where the EDX measurements are done. The sample used was used for the cell setup for a certain amount of time, and after cleaning, it was used for SEM imaging. The sample is prepared via pulse applied potential for 300 pulses using 80/20  $\text{Ni}(\text{NO}_3)_2 \cdot 6 \text{H}_2\text{O}$  (0.24 M) and  $\text{FeSO}_4 \cdot 7 \text{H}_2\text{O}$  (0.06 M).

Whenever an EDX measurement is done, it is ensured that there is no nickel substrate background that will influence the results. The surface is therefore scraped with tweezers to peel off some coating. The results of the EDX measurements can be seen in the Results section. Interestingly, there is almost no coating left on the anode after being used in the cell setup for extended periods of time.

## H Faradaic efficiency

### H.1 GC calculation

Considering the FE calculated via data from the GC, there are multiple equations used to calculate this (Eq. 18-20).  $MFM_{Correction}$  is the corrected mass flow meter value, as it is calibrated towards  $CO_2$ . The concentration of the gasses ( $H_2$ ,  $O_2$  and  $N_2$ ) ( $m_{X2}$ ) divided by 1 million ( $m_0$ ) all have their own specific conversion value (K value) needed to acquire the corrected value. The flow of gas is considered for  $m^3/s$ , as the R value chosen is 8.314. Since the MFM value read from the data is in mL/min, it needs to be divided by a factor of 60 and  $10^6$  in order to get to the desired units,  $m^3/s$ . The value of 0.876 is empirical and comes from a correction factor due to an error within one of the GC setups. Lastly, the FE is calculated using the acquired data of the ppm values of the gas ( $H_2$  or  $O_2$ ), divided by 1 million. Secondly, the acquired V/s value and standard parameters P, R, and T (T being 273 K as this is the calibrated temperature) are filled in.  $n_e$  is the number of electrons per unit of gas molecule, and  $n_{e0}$  is the mole of electrons per second, acquired from the applied current. With this, the FE is calculated in units of percentages.

$$MFM_{Correction} = \frac{\frac{1}{\frac{m_{H2}}{m_0} + \frac{m_{O2}}{m_0} + \frac{m_{N2}}{m_0}}}{K_{CO2}} [-] \quad (18)$$

$$V/s = \frac{MFM_{Correction} \cdot MFM}{60} \cdot 10^{-6} (\cdot 0.876) [m^3/s] \quad (19)$$

$$FE = \frac{m_{X2}}{m_0} \cdot \frac{P \cdot V/s}{R \cdot T} \cdot \frac{n_e}{n_{e0}} \cdot 100 [\%] \quad (20)$$

### H.2 Faradaic efficiencies

Figure H.1 indicates what the FE is when both compartments are measured. During this GC measurement, a total of 30 injections are conducted. After every 10 injections, the pressure between the two cell compartments is altered to either induce underpressure or overpressure (or equal pressure) on one side (and vice versa on the other compartment). When changing the pressure, the first four injections are excluded due to heavy fluctuations, resulting in a total of 18 injections considered for this graph. The FE varies between  $H_2$  and  $O_2$ , attributed to the use of two different GC setups. During an injection, there is a slight variation in gas flow and pressure. Both machines are operating at the same time, but the injections are not exactly at the same time. The flow, which is used to calculate the FE, fluctuates approximately 13% at the point of injection (e.g. going from 10.0 mL/min to 11.3 mL/min at the moment an injection starts). This argument could explain the difference in FE, as the trend of both gasses is relatively the same throughout the experiment. Similarly, it is quite safe to estimate the FE in this case to be around 60%, a value in the same range as the previous method.

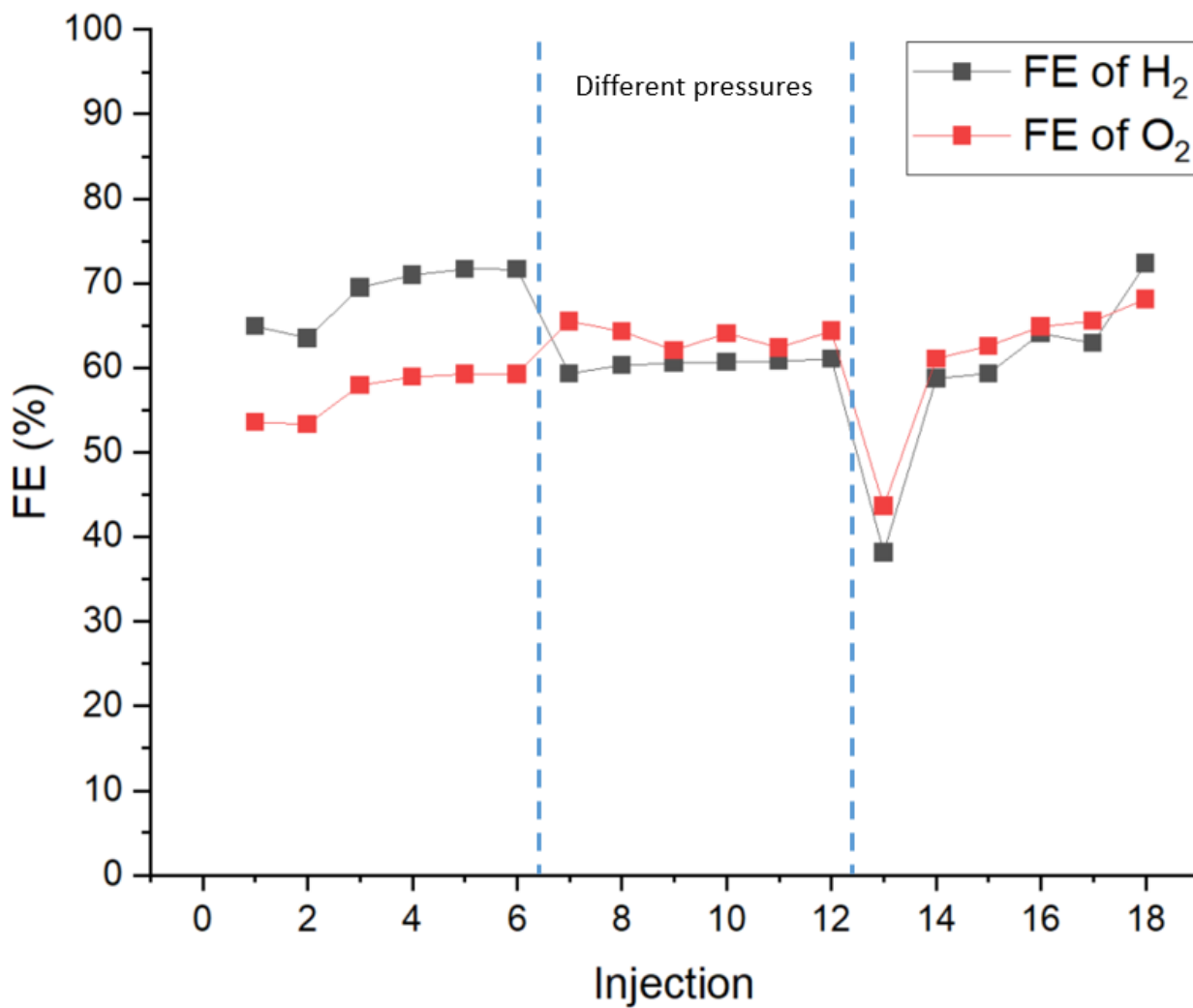


Figure H.1: (a) FE of 5 different current densities. Only the O<sub>2</sub> side is measured, and no backpressure was applied on the H<sub>2</sub> side. The carrier gas flow was set to 8 mL/min. (b) Graph of the FE values acquired from the GC. The graph is split into three segments, where the first segment considers an overpressure on the oxygen side, the second considers an overpressure on the hydrogen side, and the last segment considers equal pressure. The measurement was performed at a constant current density of 200 mA/cm<sup>2</sup>.

## I Salt formation

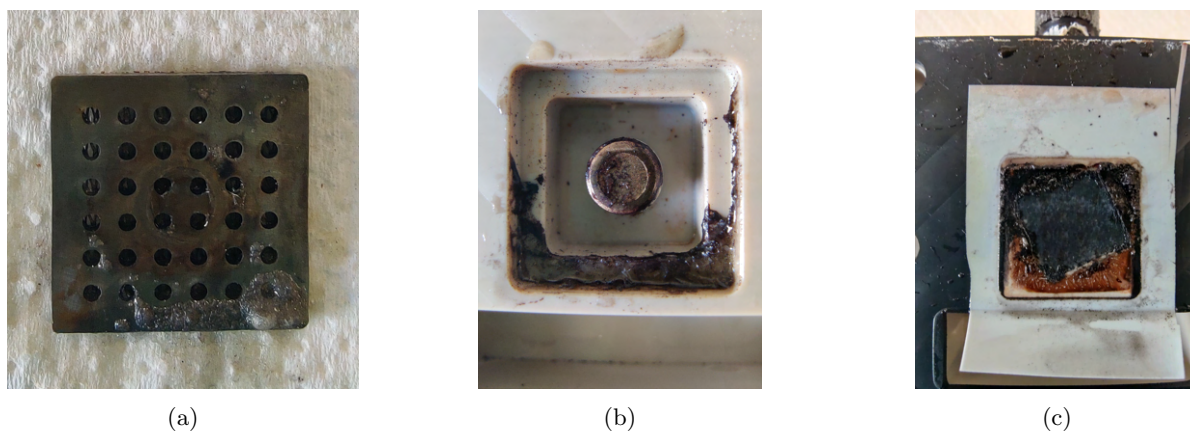


Figure I.1: (a) Backside of the anode after measuring at 80 °C for 15 hours. (b) Cathode gas chamber after measuring at 80 °C for 15 hours. (c) Cathode side of the membrane after measuring at 80 °C for 15 hours.

From Figures I.1a - I.1c, it is concluded that salt formation affects multiple parts of the setup. The effect of this result is not entirely understood, and for that reason, it is important to further investigate.

## J Gas Crossover

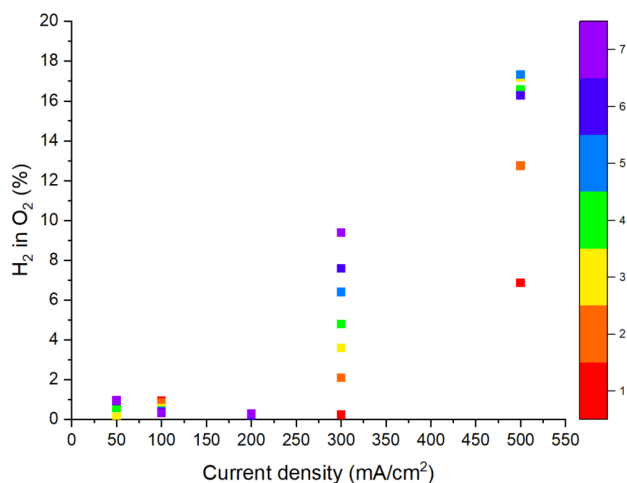


Figure J.1: Gas crossover measurement all injections. The color spectra indicate the injection number at that specific current density.

Based on the laws of thermodynamics, gasses flow from high-pressure regions towards low-pressure regions. For this reason, it is therefore interesting to use two GC setups to measure crossover on both sides to get an idea of what happens on both sides of the cell when there is a pressure difference between the two. Instead of applying backpressure; underpressure or overpressure is introduced to one of the compartments, resulting in distinct high- and low-pressure compartments. Crossover is measured in both compartments, and the outcomes are depicted in Figures J.2a and J.2b. The figure captions include important notes that help understand the acquired results. When higher pressure is applied, a significant portion of the produced gas is directed towards the opposite side, leading to a 2:1 gas crossover to the underpressurized part, mirroring the gas production ratio (2 H<sub>2</sub> to 1 O<sub>2</sub>). While the reliability of O<sub>2</sub> crossover in H<sub>2</sub> is compromised due to fluctuations in the measured O<sub>2</sub> values, the overall trend in the results indicates the feasibility of influencing gas crossover through the application of (back)pressure. With somewhat equal pressure on both sides, the resulting gas crossover of H<sub>2</sub> is then about 9%, above legal limits.

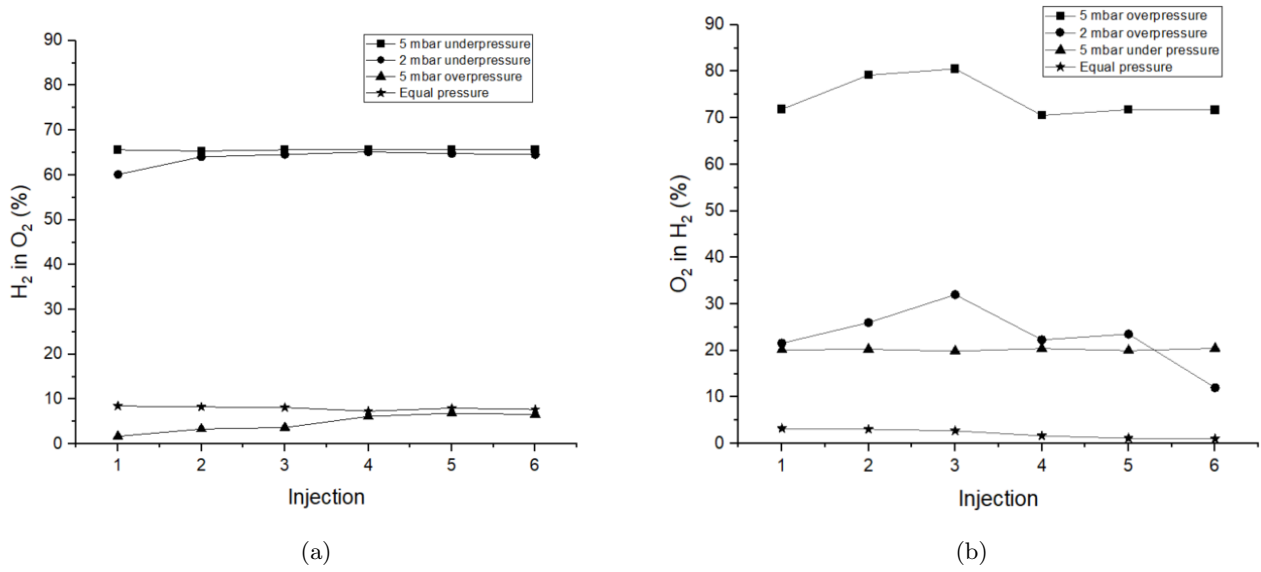


Figure J.2: (a) H<sub>2</sub> gas crossover in O<sub>2</sub> at a constant current of 200 mA/cm<sup>2</sup>. Four separate measurements are done to see what the gas crossover does. (b) OH<sub>2</sub> gas crossover in H<sub>2</sub> at a constant current of 200 mA/cm<sup>2</sup>. Four separate measurements are done to see what the gas crossover does. Note: (1) The GC setups used for this experiment uses calibration gasses to get PPM values from the area of the peak, for oxygen however, there is only one calibration gas while typically a minimum of two is required for accurate results. (2) The use of hydrogen gas in the GC setup used for O<sub>2</sub> crossover uses a different calibration gas than the GC setup used for H<sub>2</sub> crossover. The difference between the two setups is the standard value it will output whenever it detects almost no gas, this has been accounted for in these graphs.

